DOCTORAL THESIS

How Molybdenum Species Cleave the Phosphœster Bond

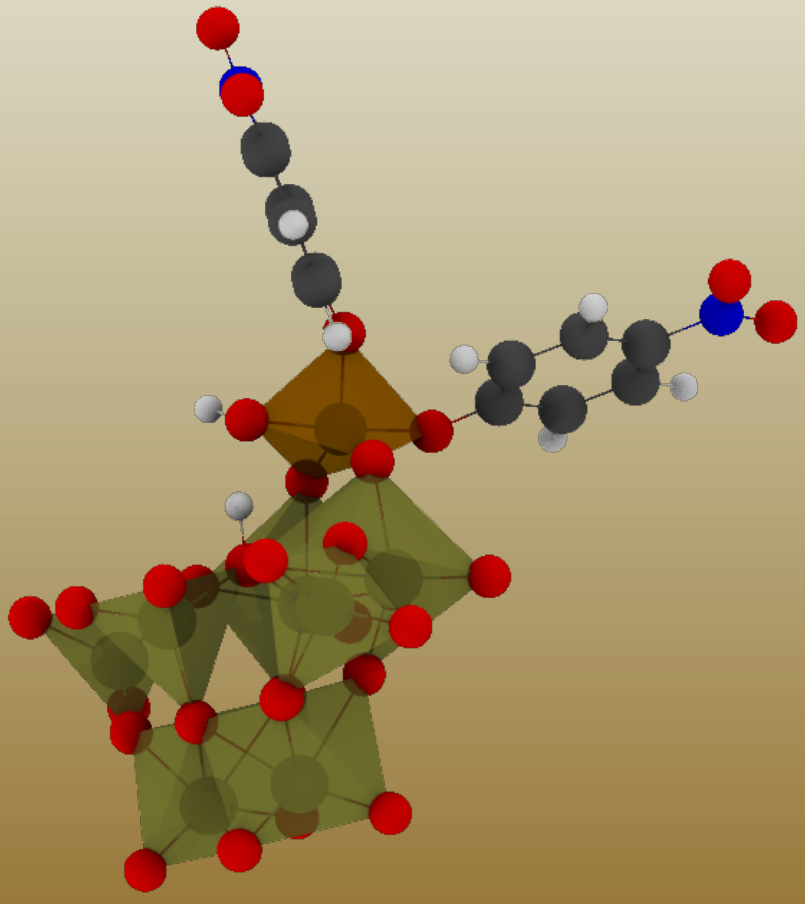

JOSE LANUZA

Universidad del País Vasco
Euskal Herriko Unibertsitatea

2023

How Molybdenum Species Cleave the Phosphoester Bond

by

Jose Lanuza

A thesis submitted in partial fulfilment
of the requirements for the Doctor of Philosophy degree
in Theoretical Chemistry & Computational Modelling
of the University of the Basque Country

May 2023

Thesis Committee: Xabier López, Thesis Supervisor
Adrià Gil, Thesis Co–supervisor
Jordi Carbó Martín
Laia Vilà Nadal
Eider San Sebastián Larzábal

ACKNOWLEDGMENTS

It felt like an eternity, but it has been "only" four years. Four years of a roller coaster journey. A lot of people came and went, and some even stayed until the end of the lane. I will try to thank each one of them, but forgive me if I forgot someone. I am thankful to everyone. Really, thanks.

First, I want to highlight the great help of my even greater advisors. Xabi, apart from your always helpful advises, I want to thank you the positiveness and support you give me. You are a fantastic advisor and a better person. Adrià, I greatly appreciate the hard work and effort you have made. I know there have been times in which we were stuck, and you always broke you back to unstuck it. I really appreciate it.

Of course, I am grateful to the Donostia International Physics Center for the opportunity of doing my PhD here, at the Euskal Herriko Unibertsitatea. They gave me the means to achieve the personal goal of contributing to the scientific world becoming a researcher. And that is something.

En este tiempo he conocido a muchas personas. Cada una con sus propias aspiraciones, alegrías y frustraciones, caminos parecidos pero diferentes. Hemos compartido parte de nuestros viajes, haciéndolos más fáciles y cómodos de caminar. Tenía la suerte de conocer ya a Mikel e Iker. Mikel, tú me enseñaste

cómo funcionaba este pequeño cacho de mundo en el que se habla euskera. Gracias a ti empecé a conocer gente en la uni y fuera de ella, y poco a poco me fui haciendo mi hueco. Iker, gracias por estar ahí para lo que fuera. Ya fuese una duda tonta, ir a tomar una birra o a perdernos por Lisboa. No me olvido del resto de la facultad, esos descansos en la cafetería con vosotros me daban aire, siempre y cuando no me engulliese el desorden de mi vida. Durante este tiempo he podido descubrir a muy buenas personas entre mis compañeros, entre los que puedo mencionar a Elisa, Raúl, Irene, Maru, Mireia y el resto de "The very best". Me lo pasé en grande con vosotros antes de que todo se volviera un caos que devora personas. Menos mal que tuve suerte y a los que les tocó aguantarme de cerca en "Hartree Home" fueron buena gente, como Roberto o lagun Marcelo.

Una tesis no se hace sola, y quiero agradecer de verdad a aquellos que me han ido ayudando a que todo fuese sobre ruedas. Aparte de Xabi y Adrià, tengo que agradecer a Vèro todo lo que hizo por aquél artículo, a Ángel sus topografías y la ayuda a aclimatarme en mi tiempo en Lisboa, al igual que a Nuno por acogerme en dos periodos distintos allí en Portugal.

Y bueno, nunca hubiera llegado hasta el final sin el apoyo que he tenido de mi gente. Algunos ya estaban ahí cuando empezó este viaje, y estarán tiempo después de que acabe. Víctor, nuestros mundos han cambiado barbaridad desde que dejé el piso de Delicias, y ya no te cuento desde que nos pegabamos findes enteros juntos. Mientras yo me sacaba el doctorado, tú te has mudado y casado con Ana. Quién nos ha visto y quién nos ve. Aún así, a pesar de la distancia y todo, has estado en parte aquí conmigo, haciendo menos difícil el

camino. Por supuesto, Álex. No me olvido de ti, y sé que tú de mí tampoco. Ya podrán pasar meses, que si te veo es como siempre. Cada momento contigo ha sido un impulso. He echado de menos tenerte más cerca para hacer cualquier plan loco e improvisado. Siempre habrá tiempo.

Podría hacer una detallada lista con toda la gente a la que he tenido la suerte de conocer en mayor o menor medida: Iria, Paula, Nerea y Fermín, Alba, Alvarito y Janire, Ixai y la gente de Urnieta... pero siempre me quedaría corto tanto de gente como de palabras. Así que sólo diré una: Gracias. A todos y a cada uno de vosotros.

A mi familia. Sé que estáis más orgullosos de mí de lo que merezco. Siempre habéis confiado en mí, y nunca me ha faltado vuestra ayuda cuando la he necesitado. Soy lo que soy y estoy donde estoy gracias a vosotros, y no existen palabras para agradecer tanto.

Y por último, y extrañamente, a mí. Porque ha habido tiempos en los que rendirse sonaba bien. No me dejé convencer y seguí sin importar cómo. A veces es más duro luchar contra uno mismo que contra el mundo.

CONTENTS

LIST OF FIGURES

LIST OF TABLES

The most violent element in society is ignorance.

– Emma Goldman

Nothing in life is to be feared, it is only to be understood. Now is the time to understand more, so that we may fear less.

– Marie Curie

The world was to me a secret which I desired to divine. Curiosity, earnest research to learn the hidden laws of nature, gladness akin to rapture, as they were unfolded to me, are among the earliest sensations I can remember.

– Mary Wollstonecraft Shelley, *Frankenstein, "The Modern Prometheus"*

PREFACE

I have a confession to make. I suffer from a disease called "curiosity". I have it since I was a child and this condition have driven me to a handful of chaotic scenarios. Once—when I was that little that I couldn't even spoke very well—I managed to open a working washing machine, causing a distressful disaster in the whole kitchen. My mother was fuming, trying to fix the awful mess I had created. Meanwhile, I was just standing there, fascinated, because I just wanted to see what happens inside.

Besides child mischiefs—including some wounds and painful hurts—curiosity also led me, slowly but unstoppable, to science. I fell in love with chemistry the day it showed me an unknown world of little things that made my entire living universe. It was like watching inside of the washing machine without getting wet. I wanted to know more, so I decided to rummage in this world of the little things to understand the bigger things. As time passed and my knowledge grew, I focused my learning ambitions away from living things to the physical laws that made them and, ultimately, to the strange quantum world of the theoretical chemistry.

So, curiosity brought me here. And here I am, unraveling a little part of the unknown world of the little things. Making computer simulations of complex

systems. Watching phosphates and molybdenum species spinning around in the washing machine. And no one gets wet. I hope this thesis satisfies some curiosities. If not, there are plenty of washing machines in the world for all of us.

PUBLICATION LIST

- Martins, F. F.; Sánchez-González, Á.; Lanuza, J.; Miras, H. N.; Lopez, X.; Bandeira, N. A.; Gil, A. Probing the Catalytically Active Species in POM-Catalysed DNA-Model Hydrolysis. *Chem. Eur. J.* **2021**, *27*, 8977–8984. DOI: 10.1002/chem.202004989

- Lanuza, J.; Sánchez–González, Á.; Bandeira, N. A. G.; Lopez, X.; Gil, A. Mechanistic Insights into Promoted Hydrolysis of Phosphoester Bonds by $MoO_2Cl_2(DMF)_2$. *Inorg. Chem.* **2021**, *60*, 11177–11191. DOI: 10.1021/acs.inorgchem.1c01088

- Sánchez-González, Á.; Bandeira, N. A. G.; Ortiz de Luzuriaga, I.; Martins, F. F.; Elleuchi, S.; Jarraya, K.; Lanuza, J.; Lopez, X.; Calhorda, M. J.; Gil, A. New Insights on the Interaction of Phenanthroline Based Ligands and Metal Complexes and Polyoxometalates with Duplex DNA and G-Quadruplexes. *Molecules.* **2021**, *26*, 4737. DOI: 10.3390/molecules26164737

- Lanuza, J.; Sánchez–González, Á.; Lopez, X.; Gil, A. Unravelling the Catalytic Effect of Heptamolybdate in Phosphate Diester Hydrolysis. (Submitted)

Outside of this Thesis

- Lanuza, J; Postils, V; Lopez, X. Can aluminum, a non-redox metal, alter the thermodynamics of key biological redox processes? The DPPH-QH_2 radical scavenging reaction as a test case. *Free Radic. Biol. Med.* **2022**, *179*, 200. DOI: 10.1016/j.freeradbiomed.2021.12.308

Chapter 1

INTRODUCTION

Scope of this Thesis

Since some centuries ago, we have known that metal species are essential for living systems and can significantly affect their biochemistry. Because of that, many different metal complexes have been used for therapeutic applications. For example, bismuth has been considered due to its anti-inflammatory properties,[1] gold because of its anti-arthritis activity,[2] iron as an anti-malaria drug,[3] silver as anti-microbial,[4] and platinum as an anti-cancer agent.[5]

Some decades ago, it was reported that polyoxomolybdates have anti-tumour activity, even more significantly than commercial drugs.[6–8] Since then, the mechanism by which these species are effective against cancer has been an elusive topic. Their activity has been mainly attributed to their interaction with some vital biological molecules, which share a key feature: the phosphoester bond. Experimental studies have found that some molybdenum species acts as promoters or catalysts to cleavege different phosphoester-containing model molecules.[9–15]

Nevertheless, the complex chemistry of molybdates, which can form a great variety of species with different nuclearity in a very short time, hinders the data collection and interpretation of these experimental studies. Because of that,

the aid of computational methodologies is crucial to elucidate the intricate mechanisms that explain their phosphoesterase activity. This thesis intends to give a closer look into these mechanisms by using theoretical approaches to different reaction models used in experimental works.

Therefore, in the present thesis we explore the mechanistic details of different phosphate ester hydrolysis reactions using various substrates (phosphate monoesters in chapters 3 and 4, phosphate diesters in chapter 5) as well as different molybdenum-containing species as promoters (molybdenum complexes in chapter 3, polyoxometalate structures in chapters 4 and 5). Additionally, more biologically realistic approaches are discussed in chapter 6, just before a brief chapter summarising the essential points extracted from this thesis.

1.1 The Rich Spectrum of Molybdenum Species

Any chemistry student with a periodical table can find molybdenum in the 6th group, between chromium and wolfram. As a middle transition metal, it can form species with great versatility, varying its oxidation state (from -II to VI) and coordination number (from 4 to 8).[16] Nevertheless, Mo rarely reaches a coordination number higher than 6 and the most common oxidation states are IV, V and VI. Besides that—like other transition metals—it can form a range of compounds with different nuclearity. These chemical properties make it a very useful "heavy" metal for many applications.[17] Moreover, the low toxicity of molybdenum—it is an essential trace metal related to some enzymes—made it a powerful candidate to replace some other toxic metals for biological uses.[18–21]

Molybdenum complexes

Molybdenum is known to form stable complexes with many organic and inorganic ligands.[22, 23] Compounds with oxygen, nitrogen or sulfur as donors are specially known for its stability. Besides that, molybdenum carbonyl and molybdenum halide complexes are also a very well known group of compounds that have interesting applications in different fields such as synthesis and catalysis. Recently, molybdocene dihalides, molybdenum dihalides dioxides and molybdenum oxo-peroxo complexes have been proved active in the catalysis of different reactions.[24–35] Specifically, its application in hydrolysis of phosphoester bonds in model substrates has been noteworthy.[13–15, 36, 37]

In biological systems, molybdenum-containing enzymes are divided into the nitrogenases—in which molybdenum is part of a $[MoFe_7S_9]$ cluster— the xanthine oxidases, the sulfite oxidases and the DMSO reductases. These last three enzymes have a similar LMoOS(OH) square-pyramidal structure with an apical Mo=O bond, a plane with sulfur atoms and a labile Mo−OH which serves as an anchoring point to the substrates.[38]

Polyoxometalates

As with other transition metals, molybdenum oxides are known to form polyoxometalates. These POMs are discrete negative clusters of oxygen and metal atoms. They constitute a large category of inorganic species, with an outstanding diversity in many aspects which made them very useful in numerous fields. The formation of these structures is a result of the nucleation of metal oxides in acidic solutions. The self-assembly processes of these polyoxometalates

are fast and difficult to study, leading to different types of polyoxometalates depending on the conditions and the species present in solution.

Polyoxometalates are divided into two families: isopolyoxometalates (iso-POMs) and heteropolyoxometalates (hetero-POMs). The formers consist of the same type of transition metal cations and oxide anions, whereas the latters include one or more heteroatoms. These heteroatoms could be inside the polyoxometalate structure or on the surface. Hetero-POMs are more diverse due to the many heteroatoms that can be included in the system, enhancing and tuning their properties to specific purposes.

POM structures can be seen as corner-sharing, edge-sharing, and face-sharing polyhedra clusters. Some key structural motifs are repeated through different polyoxometalate species, allowing the categorisation of every polyoxometalate species.

Lindqvist structure

Also called hexametalate because of the number of metal ions in the structure (M_6O_{19}), the Lindqvist structure is made by edge-sharing octahedral units. The repulsion between metal ions create slight displacements in these metal centres, causing them to be off-centre of the octahedral units. In Figure 1.1 we can see a depiction of this structure.

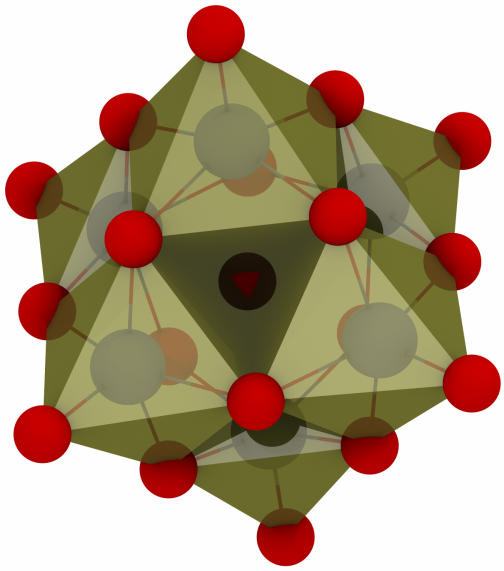

Figure 1.1: Hexametalate ($[M_6O_{19}]^{2-}$) structure. Metal cations ($M_6{}^{+}$) are represented with grey balls inside the polyhedra, oxygen anions ($O_2{}^{-}$) with red balls on the surface.

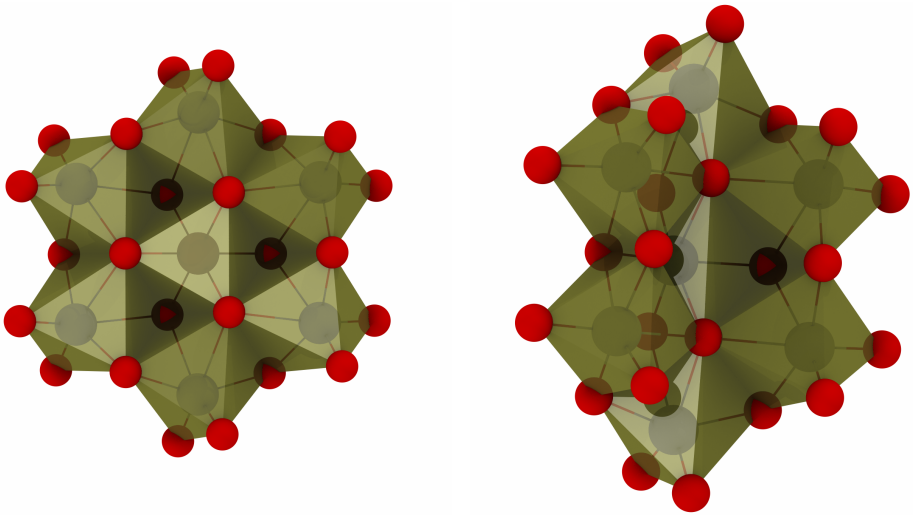

(a) (b)

Figure 1.2: Heptametalate ($[M_7O_{24}]^{2-}$) structures: a) Anderson. b) Bent structure. Metal cations ($M_6{}^{+}$) are represented with grey balls inside the polyhedra, oxygen anions ($O_2{}^{-}$) with red balls on the surface.

Anderson structure

The Anderson structure is formed by seven edge-sharing octahedra. In this heptametalate structure, the central atom can be substituted by a heteroatom capable of a octahedral arrangement. In Figure 1.2 we can see a depiction of this structure and a distorted structure frequent in isopolyoxometalate cases.

One application in progress of heptametalate structure is the use of $[Mo_7O_{24}]^{6-}$ as an anti-cancer drug. Diverse studies with this anion have been made, starting with promising results against Meth A sarcoma, MM-46 adenocarcinoma, and MX-1 carcinoma in mice. Experiments followed this up against AsPC-1 human pancreatic cancer cells, which also pointed that the heptamolybdate is binding to DNA rather to enzyme proteins. A similar apoptosis mechanism was achieved when heptamolybdate was used to suppress the growth of the gastric MKN45 cancer.[39, 40]

Keggin structure

As we increase the number of metal ions, the structures get more complex. The Keggin structure is made by twelve octahedra surrounding a tetahedron. Those octahedra are divided into four groups of three edge-sharing polyhedra connected to other groups and the central tetrahedron through corners. This central tetahedron is prone to be occupied by an heteroatom. This structure is known as α-Keggin and through rotations of one, two, three or four of the groups we can get the β, γ, δ and ϵ isomers. We can see in Figure 1.3 those different isomers which alter the high symmetry of the α-Keggin.

This Keggin polyoxometalates have been widely used as an analytical tool to determinate different heteroatoms using its reduction to blue heteropolyoxometalates. Keggin structures have also been used to catalyse different organic reactions as they are very good electron and proton transfer agents—which helps with redox and hydrogenation reactions.[41] Different Keggin structures with wolfram, molybdenum and vanadium have also been used to treat carcinoma.[42, 43]

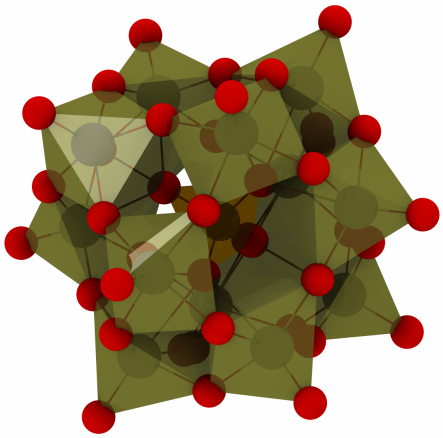

(a)

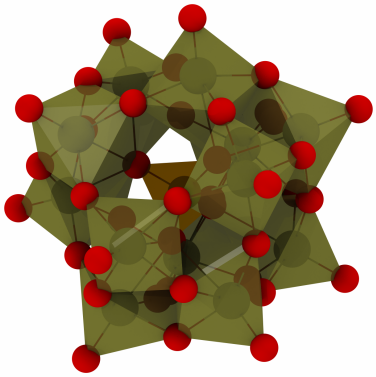

(b)

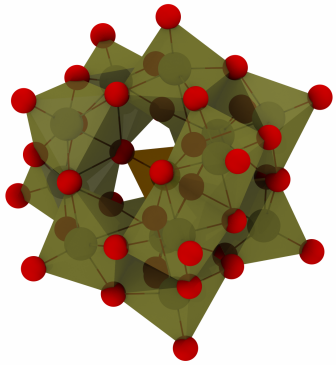

(c)

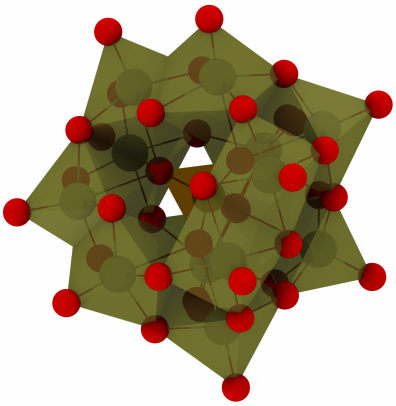

(d)

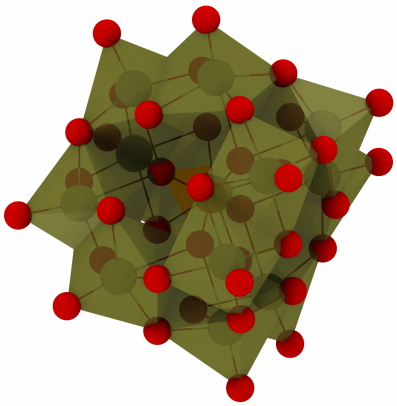

(e)

Figure 1.3: Keggin ($XM_{12}O_{40}$) structures: a) α. b) β. c) γ. d) δ. e) ϵ. Metal cations ($M_6{}^+$) are represented with grey balls inside tan polyhedra, heteroatoms (X^{n+}) with orange balls inside ochre polyhedra, oxygen anions ($O_2{}^-$) with red balls on the surface.

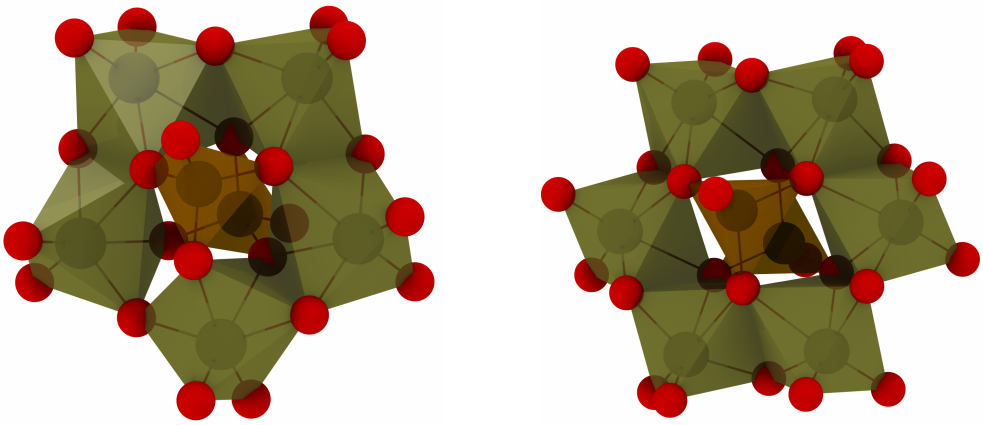

(a) (b)

Figure 1.4: Ring structures: a) $X_2M_5O_{23}$. b) $X_2M_6O_{26}$. Metal cations ($M_6{}^+$) are represented with grey balls inside tan polyhedra, heteroatoms (X^{n+}) with orange balls inside ochre polyhedra, oxygen anions ($O_2{}^-$) with red balls on the surface.

Ring structures

If we cap a polyoxometalate structure with two tetahedra, we obtain ring structures in which five—Strandberg structure—or six octahedra surround the tetrahedral units. This structures are common when heterospecies prone to tetahedral arrangements are present, like phosphate. The five-membered ring structure is less symmetrical than the six-membered one, as it contains one octahedron that has to be linked through the corners, whereas in the six-membered structure all octahedra are edge-sharing. Both ring structures are depicted in Figure 1.4.

Silverton structure

This structure requires the central atom to be a bigger heteroatom. In that case, having a higher coordination enables a particular compound. An icosahedron is placed at the centre of the molecule, surrounded by six pairs of face-sharing octahedra joint by corners. These face-sharing octahedra are relatively uncommon occurrence due to the strong electrostatic forces that repel the metal cations. In Figure 1.5 we can see a representation of this unique structure.

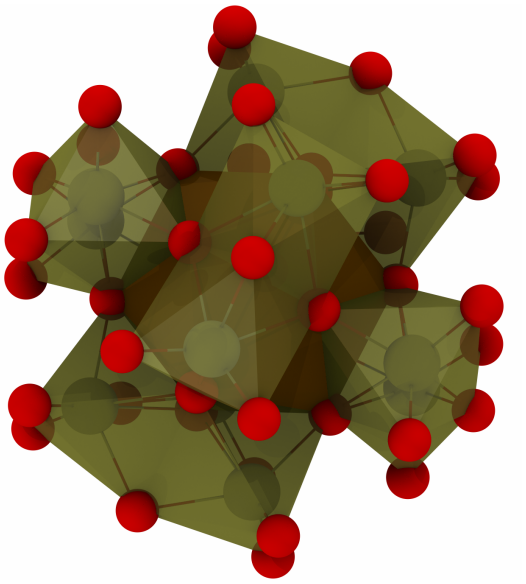

Figure 1.5: Dodecametalate ($XM_{12}O_{42}$) structure with icosahedral centre. Metal cations ($M_6{}^+$) are represented with grey balls inside tan polyhedra, heteroatoms (X^{n+}) with orange balls inside ochre polyhedra, oxygen anions ($O_2{}^-$) with red balls on the surface.

1.2 Understanding the Phosphoester Bond

So what is a phosphoester bond? As its name suggests, a phosphoester is very similar to an ester bond. Both cases are linked to another group through an oxygen atom ($-O-$). The difference is that in the phosphoester bond we have a phosphoryl ($-PO_3-$) group instead of the typical carbonyl group ($-CO-$) bonded to that oxygen atom. Very simple. Well, kind of. As we can see in Figure 1.6, three of the four oxygen atoms of the phosphate group can form a phosphoester bond and many different phosphomonoesters, phosphodiesters, and phosphotriesters are known to be stable. These phosphate esters have remarkable stability due to the delocalisation of the oxygen lone pairs, resulting in hyperconjugation and partial double bond character in the $P-OR$ bonds. So, the phosphoester bond is a very stable and versatile bond. And that make it very useful.

Phosphate Esters in Nature

The importance of phosphate esters for biological systems is outstanding and well known. Even if you are not familiar with biochemistry it is almost certain that you have heard about DNA, RNA, and probably ATP. The ability of phosphate to form various stable bonds with different groups simultaneously is used in nature to join structural units to a phosphodiester backbone. This is the case with DNA and RNA present in every living cell. Moreover, the formation and cleavage of this bond is used routinely as energy exchange, which is why ATP is commonly called "the currency of cells". Apart from storing genetic data and energy, phosphate esters are also used for many applications,

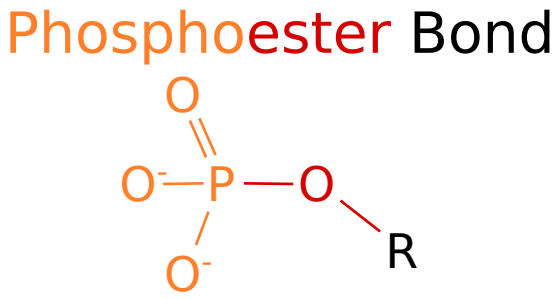

Figure 1.6: A phosphoester bond in a monosphosphate ester. Disphosphate and triphosphate esters would make use of one and two, respectively, of the three remaining oxygen atoms of the phosphate, leaving a P=O bond.

from lipid bilayers to signaling.

The phosphoester bond has to be very stable in order to have these important roles in biology. If our genetic material or our energetic exchange degraded easily, life as we know would not exist. So, slow kinetics and long half-life are characteristic of the phosphodiester bond, in part due to the electrostatic repulsion between the negatively charged phosphate and strong nucleophiles—usually negatively charged. In living systems, the modification of this biomolecules is regulated by very specialised enzymes. These are numerous and vary on the mechanism, the conditions in which they are active, and the range of substrates that are effective against.

Phosphoester Bond Hydrolysis

Phosphorylation and phosphate hydrolysis are opposite reactions. The former is the substitution of a terminal hydrogen by a phosphoryl group to give phosphate diesters or triesters. In contrast, the latter releases an oxygen-based ligand whilst an hydroxide or a water molecule performs a nucleophilic attack.

As these reactions are reversible, the same enzyme is frequently related to both processes. Two main bonds that can be formed/cleaved depending if the acting electrophile is the phosphorous atom or the C1 atom of the radical: the P−O and the C−O bonds. The results are the same, but the mechanisms are very different.

Several factors affect the preferred mechanism for the phosphate ester hydrolysis. Aspects like the esterification level or the protonation state can significantly change the specific pathway. For example, the protonation of alkyl esters leads to a shift from the normally preferred P−O cleavage to a more unusual C−O cleavage. The resulting neutral species is then hydrolysed through the latter bond if its cleavage it is not impeded by other stabilisation effects.

Another aspect that makes the problem more complex is that the reaction can go through an associative or a dissociative mechanism depending on the nucleophile and the leaving group's strengths. In the associative mechanism, the nucleophilic attack occurs before the leaving group departure. If the phosphorane-like structure formed is stable enough, the reaction proceeds through two transition states: one to reach the transient intermediate, and another to break this intermediate and get the products. In dissociative pathways the leaving group cleaves its bond before the nucleophile attack, possibly forming an unstable metaphosphate structure. As in the associative case, this pathway can occur stepwise or in a single concerted step.

Besides these associative/dissociative and stepwise/concerted distinctions there are other details that can twist the picture. As we see in Figure 1.7, nucleophiles that have a proton bound to the attacking atom can transfer it to

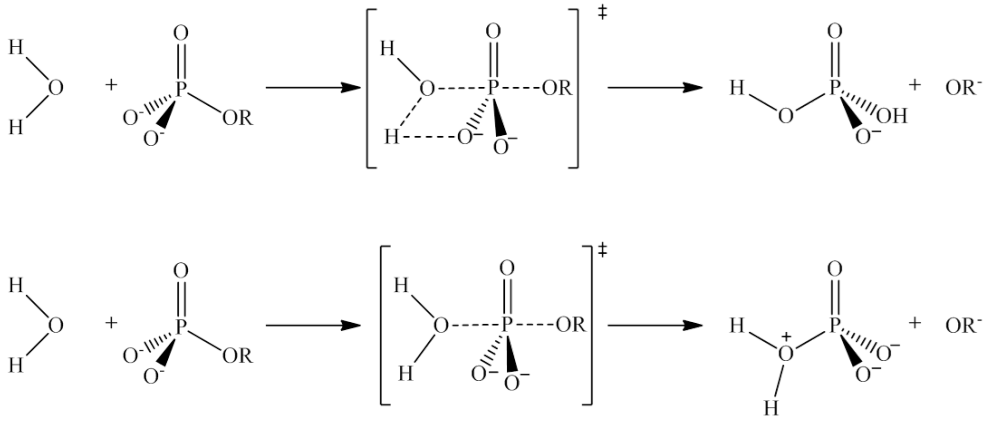

Figure 1.7: Potential mechanisms for the phosphate hydrolysis. Different conditions can lead to the substrate-assisted mechanism (up) or to the solvent-assisted mechanism (down). The possibility of metaphosphate and phosphorane intermediates in the mechanisms is not depicted for the sake of simplification.

the phosphate in a process that is called substrate-assisted mechanism. This proton transfer can happen simultaneously with the nucleophilic attack or with differents degrees of asynchronism, increasing the number of possibilities. The negative charge on the nucleophile increases its strength, leading to a more associative character. When the solvent retains the proton through hydrogen bonds whilst the nucleophile attack and the leaving group departure happen, a more dissociative mechanism is achieved, called solvent-assisted.

Usually these mechanisms occur in in-line disposition, that is, nucleophile and leaving group form and angle close to 180^{o} during the reaction. This is because equatorial positions in this pentacoordinate structures are shorter than the axial ones. Suppose the nucleophilic attack is bound to happen at a different angle to the leaving group. In that case, a pseudorotation must occur before changing the leaving group's position from equatorial to axial position

to proceed to the rupture.

Phosphate Monoester Hydrolysis

Both substrate-assisted and solvent-assisted mechanisms are plausible for phosphate monoester dianions. The preference for one or the other lies in the leaving group strength. With good leaving groups, the cleavage of the phosphoester bond happens before any proton transfer from the nucleophile. With progressively poorer leaving groups the energy gap between this mechanism and a more associative substrate-assisted pathway is shortened and both mechanisms compete. It is stated that for simple alcohol groups like methanol the substrate-assisted mechanism will prevail over the solvent-assisted one.[44] Nevertheless, the availability of competing pathways allows to achieve catalysis by stabilising either mechanism.

For monoester monoanions both mechanisms have been theorised with no clear experimental data that would differentiate one pathway from the other. Nevertheless, the proton on the phosphate increases the reactivity as intramolecular proton transfers can facilitate the leaving group release. Neutral phosphate monoesters only occur in very acidic media, being very reactive.

Phosphate Diester Hydrolysis

As we stated above, phosphate diesters are very important for biological systems. Nevertheless, experimental works on the non-catalysed hydrolysis for these compounds are scarce as their reactions are too slow. Phosphate diester hydrolysis occur through more associative mechanisms, usually involv-

ing phosphorane-like structures. Moreover, phosphodiesterases usually have some phosphomonoesterase activity, indicating that they accelerate the reaction by stabilising the substrate-assisted pathway. On the contrary, phosphomonoesterases that favour the loose substrate-assisted pathway probably will not have activity against phosphodiester especies. As in the monoester case, the extra proton on the neutral phosphate facilitates the leaving group departure. This can favour concerted mechanisms in which the nucleophile attack and the leaving group release occur simultaneously.

Phosphate Triester Hydrolysis

Phosphate triesters are more reactive than either phosphate monoester or diesters. As in previous cases, the specifics of the mechanism depend greatly on the nucleophile, the leaving group, the acidity of the medium and even the present heteroatoms. Nevertheless, phosphate triester are prone to hydrolyse through associative phosphorane intermediates or through concerted mechanisms with tighter transition states.

Chapter 2

THEORETICAL FOUNDATIONS

We, scientists, love to know things. The problem is that there are things that are hard to get information from. In our pursuit, we design intricate methods, using complicated machines to get that experimental evidence that would be impossible otherwise. Sometimes, it is not enough. Technology is not always as fast as we desire, and there are things that are impossible to measure. Not to mention that is not feasible to determine every property of every inch of the universe. So, to know a good deal of these things, we must make predictions. And to be accurate with them, we have to be sure that our methods are correct.

To predict something, we must—at least partially—understand it. For that purpose, we observe nature, see its patterns, and propose hypothesis that become elaborated scientific theories or laws, given enough time and evidence. Using those well-proven scientific laws we can then tell how the universe behaves in some specific conditions, even if we cannot directly check it. That is what science is about.

Theoretical chemistry works that way. In the scale of atoms, protons and electrons, there are a lot of things we cannot measure directly. We often got experimental data via macroscopic properties related to the microscopic ones through some formula. Sometimes that is not enough, and this approach does

not answer some questions. Theoretical chemistry addresses these questions and predict chemical and physical properties through models and simulations. Some of them need to use complex theories like quantum mechanics to work. Solving the derived equations is not easy. They require computing many operations using some approximations to give a good result in a reasonable time. Consequently, the level of approximation needed depends on the complexity of the problem.

In this chapter I will briefly explain what quantum chemistry is and give a clear view of the methods used in this thesis and their approximations.

2.1 The Blooming of Quantum Chemistry

We all know—more or less—what is chemistry, but many people struggle to understand what "quantum" is about. It is easier than it looks. It means that properties can be quantified in small packets. They are so small that we cannot see them at a bigger scale, like sand grains in a desert. In 1900, Planck said that the electromagnetic energy can only be emitted in numbers of this small packet of energy or "quantum". The development of this theory had a significant impact in the scientific world, succeeding to explain many features of our universe. In the subatomic world, quantum mechanics revealed the individual behaviour of subatomic particles, as many models failed to explain how protons, neutrons and electrons form an atom. This "new" theory—only more than a century old—continued its development and evolution, and slowly started to be applied in chemistry.

The basics of quantum mechanics are related to the Schrödinger equation

and its solutions, and I will try to make them understandable in the following lines. First, a function contains all the data that can be extracted for a given system. This is called the wavefunction and its represented as Ψ. Every process of extracting information—called measurement—is translated as applying an operator on this wavefunction. The operator that obtains the energy of the system is called the Hamiltonian, $\hat{\mathrm{H}}$, and its application on a stationary wavefunction gives a value times the wavefuntion, as Ψ is a eigenfunction of this operator. This gives the famous time-independent Schrödinger equation:[45]

$$\hat{H}\Psi = E\Psi \tag{2.1}$$

So, it seems easy. But it is a trap. Neither the Hamiltonian nor the wavefunction has simple mathematical expressions. For example, the hamiltonian can be expressed as the sum of different terms:

$$\hat{H} = \hat{T}_e + \hat{T}_N + \hat{V}_{ee} + \hat{V}_{NN} + \hat{V}_{eN} \tag{2.2}$$

Those terms are related to the kinetic (T) and potential (V) energy of the electrons (e) and nuclei (N) of the system, which can be expanded using atomic units as follows:

$$\hat{T}_e = -\sum_{i}^{n_e} \frac{\nabla_i^2}{2} \tag{2.3}$$

$$\hat{T}_N = -\sum_{A}^{n_N} \frac{\nabla_A^2}{2M_A} \tag{2.4}$$

$$\hat{V}_{ee} = \sum_{i>j}^{n_e} \frac{1}{r_{ij}} \tag{2.5}$$

$$\hat{V}_{NN} = \sum_{A>B}^{n_N} \frac{Z_A Z_B}{r_{AB}} \tag{2.6}$$

$$\hat{V}_{eN} = -\sum_{i}^{n_e} \sum_{A}^{n_N} \frac{Z_j}{r_{iA}} \tag{2.7}$$

As you see, this is starting to get complicated, as we have to take into account not only the kinetic energy of each particle but also the potential energy resulting from the interaction between them. So, we have to use approximations to make it feasible. For example, using the Born-Oppenheimer approximation, we can neglect the kinetic energy of the nuclei (T_N) and take its potential energy (V_{NN}) as a fixed value. Considering its movement too slow compared to electrons to take it into account at this scale.[46]

$$\hat{H}_e = \hat{T}_e + \hat{V}_{ee} + \hat{V}_{eN} \tag{2.8}$$

This electronic Hamiltonian yields an energy dependent on the nuclei's fixed positions. The study of this energy plus the coulombic repulsion (V_{NN}) at various nuclei positions, gives what we call potential energy surface (PES), which provides information about the most stable chemical structures—minima—the preferred paths connecting them through transition states, and their energetics.

We have an idea about the Hamiltonian, but we have not approached the electronic wavefuntion (Ψ_e) yet. Several methods have been developed to describe it. One of them is called the self-consistent field method (SCF). This approach uses the mean-field approach to simplify the interactions between

electrons. This results in isolated electrons in an average field created by the rest of the electrons, enabling the treatment of the electronic wavefunction as a product of monoelectronic orbitals ϕ_i.[47]

$$\Psi_e = |\phi_1 \cdots \phi_{n_e}\rangle \tag{2.9}$$

These orbitals are wavefunctions that describe the location and behaviour of one electron of the system. Squaring one orbital gives the probability of finding that electron in a region.

This approximation was later improved to satisfy the Pauli exclusion principle—which states that two identical fermions cannot have the same quantum state—by including antisymmetry in this expression. This was achieved using the Slater determinant, giving birth to the Hartree-Fock method.[48–50] However, the mean field of electrons had to be calculated by an iterative process, which prevented the application of this method until several years later.[51]

Other theories focused more on explaining the chemical bond by studying its electron distribution. One of them was called valence bond theory, in which electrons were treated as localised in bonds between atoms using non-orthogonal orbitals.[52] Later, this theory was improved by adding concepts of resonance and hybridisation.[53, 54] A different theory—called molecular orbital theory—used linear combinations of atomic orbitals to get orthogonal orbitals covering the entire molecule.[55–58]

The development of computers increased the applicability of these meth-

ods, consolidating them in the scientific world. It also enabled the development of better approaches, improving the drawbacks of the previous ones. For example, as a consequence of the self-consistent field, the Hartree-Fock method, lacked of specific electronic interactions, also called electronic correlation. The Møller-Plesset theory used perturbation theory to include correlation as a perturbation of the Hartree-Fock method, increasing the accuracy at the expense of computational cost.[59, 60] Another methodology that solved the correlation problem was the inclusion of different electronic configurations by using more than one Slater determinant. Both configuration interaction (CI)[61, 62] and coupled cluster (CC)[63, 64] methods used this approach. They differentiate in how they mix excited states. Whereas CI include them through a weighted summation, CC uses a product of exponential functions. This results in different weaknesses, since CI has no size extensivity and CC is generally non-variational.

Last but not least, another completely divergent approach to the problem is to avoid the use of the wavefunction to calculate the properties of the system.[65, 66] The density functional theory uses electron density to replace it.[67] Since the electron density is much simpler than the wavefunction, the computational efficiency is more significant. Nevertheless, the lack of a mathematical expression that relates unequivocally properties as the energy with the electron density makes the method challenging. Different functionals have been proposed to get meaningful results.[68]

2.2 The World as a Combination of Basis Sets

Representing an orbital into an operable mathematical object is not straightforward. Frequently, orbitals are approximated as a product of the radial and angular parts.

$$\phi = R_n Y_{l,m} \tag{2.10}$$

Then, the radial part is expressed as a normalised function that depends on the quantum number n, the charge ζ, and the electron-nucleus distance r. The Slater-type functions use the following expresion:[69]

$$R_n^{STO} = N r^{n-1} e^{-\zeta r} \tag{2.11}$$

This equation has a complicated integration due to the the use of $r = \sqrt{x^2 + y^2 + z^2}$. Because of that, Gaussian functions are popularly used to solve this problem, as they use the square of the distance, simplifying the calculations:

$$R_{n,l}^{GTO} = N r^{2n-2-l} e^{-\zeta r^2} \tag{2.12}$$

Nevertheless, Gaussian functions also have their problems. They have issues to represent the cusp and they decay too fast at longer distances. To overcome this, a combination of Gaussian functions is used to refine the behaviour at such conditions.

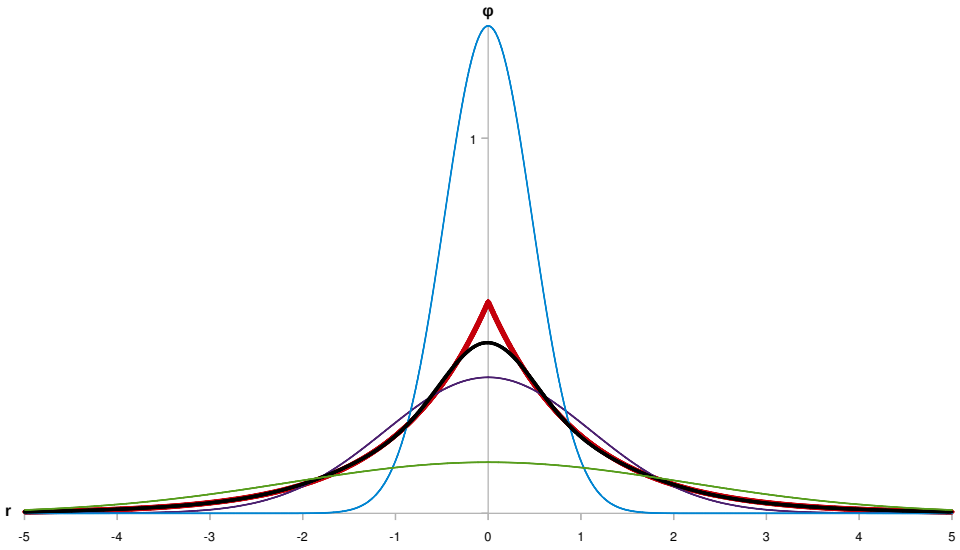

Figure 2.1: A combination (black) of three gaussian functions (blue, green and aubergine) using least-squares fitting to represent a Slater type function (red).

These combination of functions are called basis sets, and many different types have been developed to work with different systems and methods.[70] We can see in Figure 2.1 a combination of three Gaussian functions to emulate a Slater type function.

2.3 Mapping the Reaction: Potential Energy Surface

As previously stated, the Born-Oppenheimer approximation allowed us to calculate an electronic energy for fixed nuclei positions, neglecting the nuclei kinetic energy and taking their electrostatic repulsion as a constant.[46]

Nevertheless, if we want our results to be chemically relevant we have to be sure that the disposition of the atoms is accurate for the system we are studying. If not, the energetic information will be flawed and useless. We

have to analyse how the potential energy varies when we change the nuclei coordinates to optimise these structures.

Every non-linear system has 3N−6 internal coordinates that could affect its potential energy. In most cases, it is impossible to represent how these coordinates affect the potential energy in a simple graph. The standard solution is to choose one or two relevant variables—a coordinate or a combination of them—to make potential energy curves or surfaces. For example, if we were studying the formation or cleavage of a bond, a potential energy curve using the interatomic distance between the involved atoms could be depicted.[71, 72]

Although we cannot represent a potential energy surface containing every internal coordinate, we can estimate the first and second derivatives of the energy with respect to the nuclei coordiantes to characterise the relative minima—zero gradient points that represent stable structures—and the saddle points that link them through the reaction coordinate—that is, the minimum energy path in which the highest energy point is the transition state.[73, 74]

Therefore, the use of geometry optimisation algorithms in this potential energy surface allows us to describe the reaction mechanisms of chemical systems precisely: their reactant, intermediate, and product states, and the transition states along the intrinsic reaction coordinate that connects these stationary points.

Sometimes, finding the minimum energy path between two stationary states is far from simple, mainly if the transition state is located in a complex energy surface involving flat regions, or if it involves too many atomic rearrangements. In such cases, more complex algorithms can be used to overcome

these problems. For example, the Nudged Elastic Band method interpolates the minimum energy path between two structures. It optimises each interpolated point, including a spring force that ensure that each point is connected to the same path and that all points are equally spaced.

2.4 Using the Electron Density Instead

The wavefunction has a lot of variables. If monoelectronic orbitals are used to describe the radial part, there are three variables for each of the electrons in the system. That scales immensely as the number of electrons increases. The electron density (ρ) is quite different, as it only depends on the three coordinates of the space. This results in a significant reduction of the computational cost in systems with large number of electrons. To achieve that, new expressions had to be developed to relate the energy and other properties to the electron density. These functions of functions are called functionals, and a bunch of them have been created in order to improve the method and get better results.

The first try to adapt the Schrödinger equation in terms of the electron density used the uniform electron gas model, in which the electrons where distributed consistently. The kinetic energy was expressed as follows:[65, 66]

$$T_{UG} = \frac{3}{10}\sqrt[3]{9\pi^4}\int \sqrt[3]{\rho^5}dr \tag{2.13}$$

And consequently the total energy was written as:

$$E_{UG} = \frac{3}{10}\sqrt[3]{9\pi^4}\int \sqrt[3]{\rho^5}dr - Z\int \frac{\rho}{r}dr + \frac{1}{2}\iint \frac{\rho\rho'}{|r-r'|}drdr' \tag{2.14}$$

This expression can be solved easily, but apart from qualitative information, it is a crude approximation that shows significant drawbacks to be used at a molecular level.

Hohenberg-Kohn Theorems

Density functional theory became useful after the Hohenberg-Kohn theorems demonstrated two things.[67] The first is that an external potential V_{ext}—which is the potential made by the nuclei to the electrons and defines the system—can be related to a specific electron density. And second, we can determine the properties of the system in terms of the electron density. A universal functional exists in principle, and the energy can be expressed as:

$$E = T + V_{ee} + V_{ext} = F_{HK}[\rho] + \int \rho v_e x t dr \tag{2.15}$$

Moreover, this functional follows a variational behaviour: the exact ground energy the lower limit if the ground electron density is used. Using this, we can minimise the energy to find the ground-state electron density, provided the functional is exact.

Kohn-Sham Equations

Although these theorems sound quite powerful, they do not state how to calculate a system's ground-state electron density. The first attempt to do it used a non-interacting reference system, obtaining monoelectronic orbitals and expressions like in the Hartree-Fock method.[68] The hamiltonian was defined as follows:

$$\hat{H}_S = -\frac{1}{2}\sum_{i}^{n_e}\nabla_i^2 + \sum_{i}^{n_e}\hat{V}_{eff} \tag{2.16}$$

Solving these equations, we get the orbitals that will be used to get the initial guess of the electron density. Here, V_{eff} is chosen to be an effective external potential that affects the non-interacting electrons. This potential contains the following terms:

$$\hat{V}_{eff} = \hat{V}_{ext} + \hat{J} + \hat{V}_{XC} \tag{2.17}$$

So, this effective potential includes the external potential made by the nuclei to the electrons, the coulombic repulsion between them, and the exchange-correlation term, which accounts all non-classical corrections to this non-interacting system:

$$\hat{V}_{XC} = \hat{T}_C + \hat{V}_{ncl} = (\hat{T} - \hat{T}_C) + (\hat{V}_{ee} - \hat{J}) \tag{2.18}$$

The explicit form of the exchange-correlation potential is unknown, being the only term of these equations that is not exact. The common practice in density functional theory is to define exchange-correlation energy functionals with respect to the electron density to approximate this value. These equations are then solved iteratively, and the solution's quality depends on the functional's suitability to describe the system.

Using the Uniform Electron Gas Again (LDA)

The first approximation to the exchange-correlation functional used the so-called local density approximation, taking the uniform electron gas as reference. The accuracy of this model depends on how the electron density varies in space, being a bad option for systems with localised regions—which are frequent.[68, 75] The functional can be split into the exchange and correlation terms. The first is known, but the latter have been approximated using analytical approaches. Here we will see two examples, one developed by Vosko, Wilk, and Nusair;[76] and another developed by Perdew and Wang:[77]

$$E_{XC}^{LDA}[\rho] = \int \rho\epsilon_X d\vec{r} + \rho\epsilon_C d\vec{r} \tag{2.19}$$

$$\epsilon_X = -\frac{3}{4}\sqrt[3]{\frac{3\rho}{\pi}} \tag{2.20}$$

$$\begin{aligned}\epsilon_C^{VWN} = A\Bigg\{ & ln\frac{1}{1+b\sqrt[6]{\frac{4\pi\rho}{3}}+c\sqrt[3]{4\pi\rho}} + \frac{2b}{\sqrt{4c-b^2}}tan^{-1}\frac{\sqrt{4c-b^2}}{2\sqrt[6]{\frac{3}{4\pi\rho}}+b} \\ & + \frac{bx_0}{ax_0^2+bx_0+c}\left(ln\frac{\sqrt[3]{\frac{3}{4\pi\rho}}-2x_0\sqrt[6]{\frac{3}{4\pi\rho}}+x_0^2}{\sqrt[3]{\frac{3}{4\pi\rho}}+b\sqrt[6]{\frac{3}{4\pi\rho}}+c}\right. \\ & \left. + \frac{4x_0+2b}{\sqrt{4c-b^2}}tan^{-1}\frac{\sqrt{4c-b^2}}{2\sqrt[6]{\frac{3}{4\pi\rho}}+b}\right)\Bigg\}\end{aligned} \tag{2.21}$$

$$\epsilon_C^{PW} = -2A\left(1+\alpha_1\sqrt[3]{\frac{3}{4\pi\rho}}\right) ln\,[1 + \frac{1}{2A\left(\beta_1\sqrt[6]{\frac{3}{4\pi\rho}} + \beta_2\sqrt[3]{\frac{3}{4\pi\rho}} + \beta_3\sqrt[2]{\frac{3}{4\pi\rho}} + \beta_4\sqrt[3]{\frac{9}{16\pi^2\rho^2}}\right)}] \tag{2.22}$$

As you can see, these analytical equations are heavily parameterised, and the results depend on the data used to calibrate the parameters. Local density approximations work well enough for equilibrium geometries, harmonic frequencies and dipole moments, but fails to give accurate approximations to exchange, correlation energies and many chemical properties.

Tuning the Density (GEA & GGA)

So, the logical next step is to make the electron density to be non-local. For that, we could use a Taylor expansion to the exchange-correlation functional, giving a gradient expansion approximation (GEA):[68]

$$E_{XC}^{GEA} = E_{XC}^{LDA} + E_{XC}^{nl} = \int \rho\epsilon_{XC}dr + \sum_{i=\alpha}^{\beta}\sum_{j=\alpha}^{\beta} C_{XC}^{ij}\frac{\nabla\rho_i\nabla\rho_j}{\sqrt[3]{\rho_i^2\rho_j^2}} \tag{2.23}$$

However, this approximation was even worse than LDA for systems where the electron density does not vary smoothly. This is because this approximation does not reproduce well the exchange hole—a depletion zone in the electron density near the electrons due to Pauli exlusion principle—whilst LDA does it. So, this approximation was improved using restrictions to reproduce these holes better. The result was an "enhancement factor" F_{XC} which modified the LDA term.[78–80]

$$E_{XC}^{GGA} = \int \rho \epsilon_{XC}^{LDA} F_{XC} dr \tag{2.24}$$

Also, this enhancement factor could be split into the correlation and exchange terms, and different equations were proposed, putting them in terms of the reduced density gradient (s) and atomic radii based on the electron density (Wigner-Seitz, r_s).

$$s = \frac{|\nabla \rho|}{\sqrt[3]{24\pi^2 \rho^4}} \tag{2.25}$$

$$r_s = \sqrt[3]{\frac{3}{\pi \rho}} \tag{2.26}$$

This approach—called Generalised Gradient Approximation—worked, solved GEA problems and improved LDA. Precisely, it reduced the overbinding error of LDA when applied to molecules and solids.

Tune it Even More (meta-GGA)

The next step was to include more inhomogeinity parameters into the mix. For example, the non-interacting kinetic energy could be put in a functional. To do so, the meta-generalised gradient approximations have included a kinetic energy density (τ_S)to their expressions.[81, 82]

$$\tau_S = \frac{1}{2} \sum_{i=\alpha}^{\beta} |\nabla \psi_i|^2 \tag{2.27}$$

This expensive method improves some properties, but it fails to reproduce the long range behaviour of the exchange hole.

Putting some Hartree-Fock on it: Hybrid Functionals

DFT did not have an exact expression to calculate the exchange. But we know that Hartree-Fock method does. So why do not combine both? That is the idea that gave birth to the hybrid functionals.[83, 84] With this approach, we obtain a compromise since the exchange energy is improved—which has a greater overall contribution—while the correlation energy worsens, as Hartree-Fock does not describe it.

The exchange-correlation energy is then written as an integral of a parameter-dependent term, reproducing the potential of a system with non-interacting electrons when λ is zero and the potential of a fully interacting system—using some DFT approximation—when λ is one.

$$E_{XC} = \int_0^1 E_{XC}^{\lambda} d\lambda \tag{2.28}$$

In this method, both states are connected by a continuum of partially interacting systems with no exact mathematical expression. So this energy is simply put as a linear combination of the limit states:

$$E_{XC} = c_0 E_{XC}^{\lambda=0} + c_1 E_{XC}^{\lambda=1} \tag{2.29}$$

The first parameterisation used was the half-and-half, but later this coefficients were adjusted using thermochemical data, obtaining values of 0.332 and

0.575 for c_0 and c_1, respectively.[83]

The next step was to use not two but three parameters. We get the following expression by mixing the gradient corrections with the local density approximation and the exact exchange.

$$E_{XC}^{B3} = E_{XC}^{LDA} + a\left(E_{XC}^{\lambda=0} - E_{X}^{LDA}\right) + b\Delta E_{X}^{GGA} + c\Delta E_{C}^{GGA} \tag{2.30}$$

As we see here, parameter a indicates the exchange replaced with exact exchange, and b and c regulate the gradient approximation to exchange and correlation, respectively. These values are 0.20, 0.72, and 0.81, and they were adjusted to reproduce ionisation and atomisation energies.[84] For the GGA part, multiple approximations can be used. The first used was B88 for the exchange and PW91 for the correlation, giving the B3PW91 method.[85, 86] Using the LYP functional as correlation functional and keeping the rest of the method, we get the popular B3LYP method, which is the most used in this thesis.[87]

$$\Delta E_{X}^{B88} = -\frac{\beta \sqrt[3]{576\pi^4\rho^4 s^2}}{1 + \frac{6\beta \sqrt[3]{24\pi^2 s}}{sinh(\sqrt[3]{24\pi^2 s}}}) \tag{2.31}$$

$$\begin{aligned}\Delta E_C^{LYP} = &- \int \frac{4a\rho_\alpha\rho_\beta}{1+d\sqrt[3]{\rho^4}} - \int ab\rho_\alpha\rho_\beta \left[\frac{12\sqrt[3]{36\pi^4(\rho_\alpha^8+\rho_\beta^8)}}{5e^{\frac{c}{\sqrt[3]{\rho}}}\sqrt[3]{\rho^{11}}\left(1+\frac{d}{\sqrt[3]{\rho}}\right)} \right. \\ &+ \frac{(47-7c\sqrt[3]{\rho})|\nabla\rho|^2 - (45-c\sqrt[3]{\rho})(|\nabla\rho_\alpha|^2+|\nabla\rho_\beta|^2}{18e^{\frac{c}{\sqrt[3]{\rho}}}\sqrt[3]{\rho^{11}}\left(1+\frac{d}{\sqrt[3]{\rho}}\right)} - \\ &\left. - \frac{c\sqrt[3]{\rho}-11(\rho_\alpha|\nabla\rho_\alpha|^2+\rho_\beta|\nabla\rho_\beta|^2)}{9e^{\frac{c}{\sqrt[3]{\rho}}}\sqrt[3]{\rho^{14}}\left(1+\frac{d}{\sqrt[3]{\rho}}\right)} \right] \\ &+ \int \frac{ab\left[2\rho^2|\nabla\rho|^2 - (2\rho^2-3\rho_\alpha^2)|\nabla\rho_\beta|^2 - (2\rho^2-3\rho_\beta^2)|\nabla\rho_\alpha|^2\right]}{3e^{\frac{c}{\sqrt[3]{\rho}}}\sqrt[3]{\rho^{11}}\left(1+\frac{d}{\sqrt[3]{\rho}}\right)}\end{aligned} \tag{2.32}$$

Other hybrid methods mixed different exact exchange and DFT functionals. PBE0 mixed one-quarter of HF exchange with three-quarters of PBE exchange, using the PBE correlation energy.[80, 88] Another method is to use the meta-GGA methods with a X percentage of HF, like the Minnesota functionals Myz.[89]

$$E_{XC}^{Myz} = \frac{X}{100}E_X^{HF} + \left(1-\frac{X}{100}\right)E_X^{Myz} + E_C^{Myz} \tag{2.33}$$

These functionals have large expressions due to mixing different approximations (PBE, HCTH, VS) using linear combinations, adding range-separation features and non-separable functional forms, and forming an entire family of functionals with different properties and applications.[90–95]

In general, they work very well when dispersion forces are present on the studied system, which is a drawback for other density functional methods.

Focusing on the Dispersion: Grimme Corrections to DFT

London dispersion forces are very weak attractive interactions that occur when two atoms are close enough—but not bonded. A temporary formation of a dipole—created by the negatively charged electronic density around the positive nucleus—in one atom creates another temporary dipole in the neighbour, attracting them together. Usually, DFT methods describe poorly long range correlation effects as these, and that description can be quite important depending on the studied case. For such functionals, some corrections were developed and improved.[96–98] These corrections make use of damping functions (f_d) as well as some atom-related coefficients ($C_{ij,n}$ and R_{ij}) and adjustable parameters (d, s_n, s_r, α_n and a_n).

$$E_{disp}^{D2} = -\sum_{i>j}^{N_N} \frac{C_{ij,6}}{r_{ij}^6} f_{d,6} \tag{2.34}$$

$$f_{d,6}^{D2} = \frac{s_6}{1 + e^{-d\left(\frac{r_{ij}}{s_r R_{ij}} - 1\right)}} \tag{2.35}$$

$$E_{disp}^{D3} = -\sum_{i>j}^{N_N} \left(\frac{C_{ij,6}}{r_{ij}^6} f_{d,6} + \frac{C_{ij,8}}{r_{ij}^8} f_{d,8} \right) \tag{2.36}$$

$$f_{d,n}^{D3} = \frac{s_n}{1 + 6\left(\frac{r_{ij}}{s_r R_{ij}}\right)^{-\alpha_n}} \tag{2.37}$$

$$f_{d,n}^{BJ} = \frac{s_n r_{ij}^n}{r_{ij}^n + (a_1 R_{ij} + a_2)^n} \tag{2.38}$$

Improving that Correlation: Double Hybrid Functionals

The last step in this Jacob's ladder of DFT (see Figure 2.2) is to improve the correlation energy by including a correction that uses non-occupied orbitals. Common double hybrid functionals used the second order perturbation theory to enhance orbital dependent functionals and then mix it with some hybrid functionals.[99–103] These double hybrid functionals reached a very high accuracy—comparable to high-level wavefunction methods—at a much more reachable computational cost. Another approach in this category is to replace the PT2 correction to correlation with the random phase approximation (RPA).[104–108] The RPA methods are more commonly used in materials science, as their strength is the prediction of chemical and physical properties of large-gap compounds. However. including RPA into double hybrid functionals does not improve double hybrid functionals performance using perturbation theory, and improvement over pure RPA methods is scarce.[109]

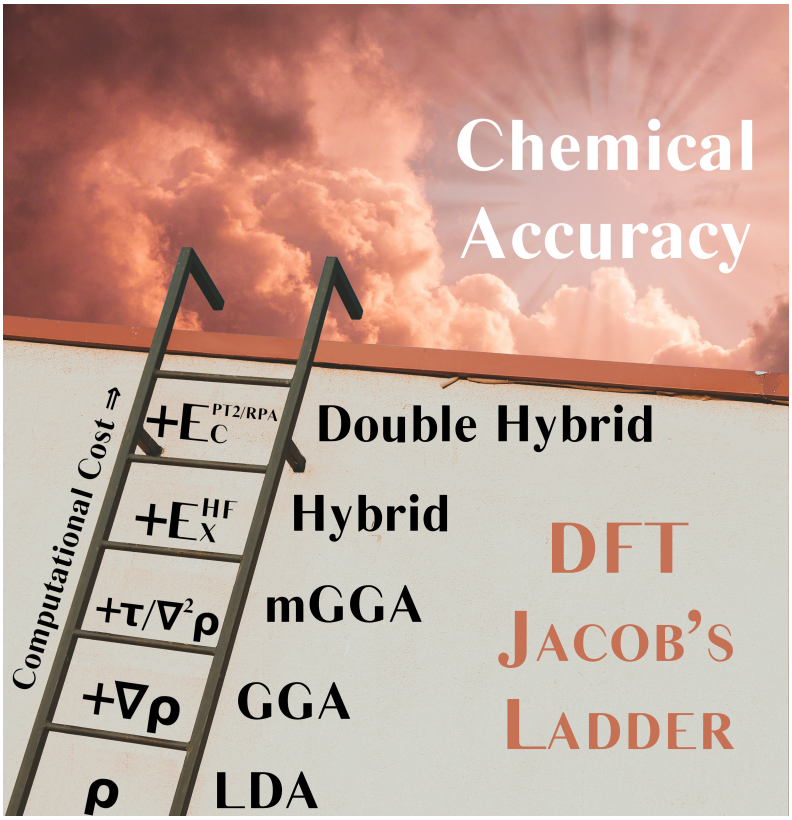

Figure 2.2: Jacob's ladder representation of the evolution of DFT functionals in the pursuit of chemical accuracy.

2.5 How to Split a a Molecule into Atoms

We know that atoms form a molecule. In our classical view, this partition seems intuitive. In quantum chemistry, in which electrons are delocalised around the nuclei, that is not so easy. How to distribute these electrons is a crucial topic that has been thoroughly discussed over the years. Some key properties that describe the electronic status depend on this partition: oxidation states, bond orders, aromaticity, etc. There is no perfect way to define the extension of atoms, and all methods have some arbitrariness with its limitations and weak

points. There are two main approaches: by cutting the real space, or by using the Hilbert space—the mathematical space in which the wavefunction is defined.

Atoms in the Hilbert Space

An atom in the Hilbert space can be seen as formed by monoelectronic orthonormal functions centred on a nucleus. Also, we can decompose any molecular occurrence into a sum of those atomic orbitals. So, using the elements of the first order spinless density matrix—which is related to the occupancy of the single-electron orbitals—we can split the electron density as a linear combination of the atomic orbitals:

$$\rho = \sum_{i,j} \rho_1^{ij} \phi_j^* \phi_i \tag{2.39}$$

Logically, when the electron density is integrated over all space gives the number of electrons, and in this case, we can relate it to the overlap matrix.

$$n_e = \sum_{i,j} \rho_1^{ij} \int \phi_j^* \phi_i dx = \sum_{i,j} \rho_1^{ij} S^{ji} \tag{2.40}$$

Then, we can expand this summation and then group every product into atomic and overlapping terms:

$$n_e = \sum_{N,i\in N} \sum_{M,j\in M} \rho_1^{ij} S^{ji} = \sum_{N,i\in N} \rho_1^{ii} S^{ii} + \sum_{N\neq M, \substack{j\in M \\ i\in N}} \rho_1^{ij} S^{ji} = \sum_N n_N + \sum_{N\neq M} n_{NM} \tag{2.41}$$

With this, we obtain the atomic population n_N and the overlapping population between two atoms n_{NM}. If we wanna split fully the molecule into atoms, the latter terms have to be sliced and dispensed to the involved atoms. Mulliken divided them into halves to get the contribution, which is a gross approximation.[110] With these populations we can infer approximately the atomic properties of the atoms involved in the molecule. Löwdin tried to improve this method with the inclusion of an orthonormalisation process which would reduce drastically the overlapping terms.[111] But both methods were very basis set dependant and did not work well for plane-wave or bond-centred basis sets. Moreover, the inclusion of smoother diffuse functions—improving the description of anions and dipoles—could end up in atomic populations that lacked physical meaning.

Atoms in the Real Space

If we want to split the thee-dimensional space into atoms, we should make each point belong to an atom. From there, it seems easy then to integrate the desired properties over these atomic domains. The problem is that we have to chose the edges of the atomic domains correctly and to do so, we have to do some topological analysis of the electronic structure. By studying the electron density gradient and using the Hessian matrix to characterise the critical points where the gradient is zero, we can then differentiate nuclear, bond, ring and cage points. We can define a bond as the path that connects two nuclear points—maxima in the electron density. Then, a bond critical point is a minimum along that path and a maximum in the rest of directions. We can define an interatomic surface that cross this bond path and have zero

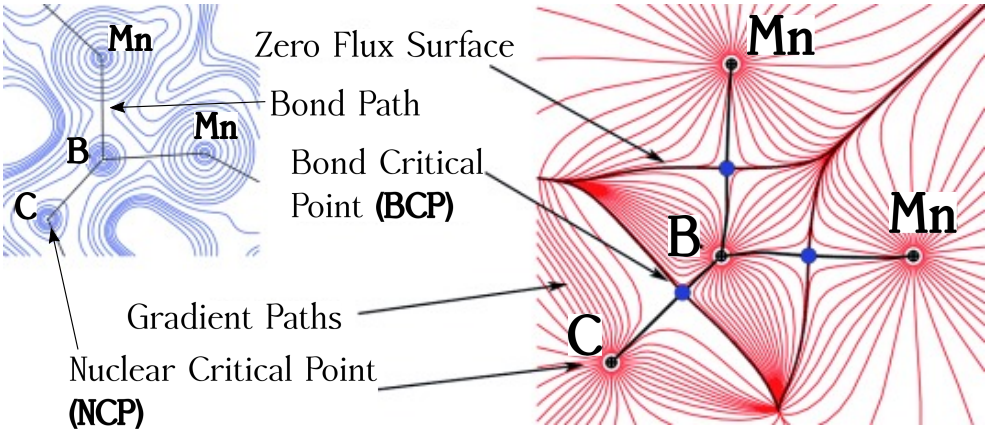

Figure 2.3: Electron density contour map (left) and the corresponding gradient vector field (right). Blue lines represent surfaces with the same electron density. Red lines originates in maxima and end up in the minima, following the gradient and never crossing the atomic boundaries. Example taken from Stalke *et al.* work.[114]

flux—no gradient trespass this surface—and use it to determine the limits of the atoms. This is the methodology used in the QTAIM scheme to define the atom boundaries, leading to complex shapes of the atomic domains which are harder to compute.[112, 113] In Figure 2.3 we can see an example of this analysis. The occurrence of non-nuclear attractors can also be a problem, as sometimes they are interpreted as nuclear critical points and make chemical analysis difficult.

Another way to approximate the atoms is to consider that atoms can overlap, having no exact boundaries.[115] In these regions, each atom presence is evaluated through some coefficients or "weights", enabling the decomposition of physical properties. These weights can be calculated as the ratio between the density of one atom and the summation of atomic densities in a non-interacting system with the same disposition of atoms. This method can be

improved using an iterative process to make these atomic densities to integrate into the correct number of electrons.[116] Another approach to calculate the weights is using algebraic functions that guarantee unique contributions to the nuclear weights.[117, 118] This formulation uses a parameter μ—which quantifies which atom is closer to that location, being zero in the middle—to define a step function that define the Voronoi cells that are used to get the weights. Then we can change the reference midpoint to the atomic radii or to the bond critical point to better partition the molecular space into atoms.[119, 120]

2.6 And the Solvent?

Isolated systems in which atoms and molecules are not affected by any external species are uncommon. Nevertheless, it is impractical to include all surrounding atoms explicitily in our methodologies because of the computational cost. We have two main approaches to overcome this trouble: *i)* to include only some extent of the surroundings (explicit solvent), or *ii)* to approximate it with a continuum model with some physical properties (implicit solvent). To include molecules explicitly is only feasible for a small quantity or in conjunction with low-demanding computational methods like molecular mechanics. Implicit models are more easily computed and can approximate the general properties of the solvent, with the lack of specific interactions as an important drawback of the model. Nevertheless, both methodologies can be combined to include meaningful specific interactions with solvent molecules whilst the rest of the solvent is modeled as a continuum.

In the implicit models,[121, 122] the solvation energy is calculated as the

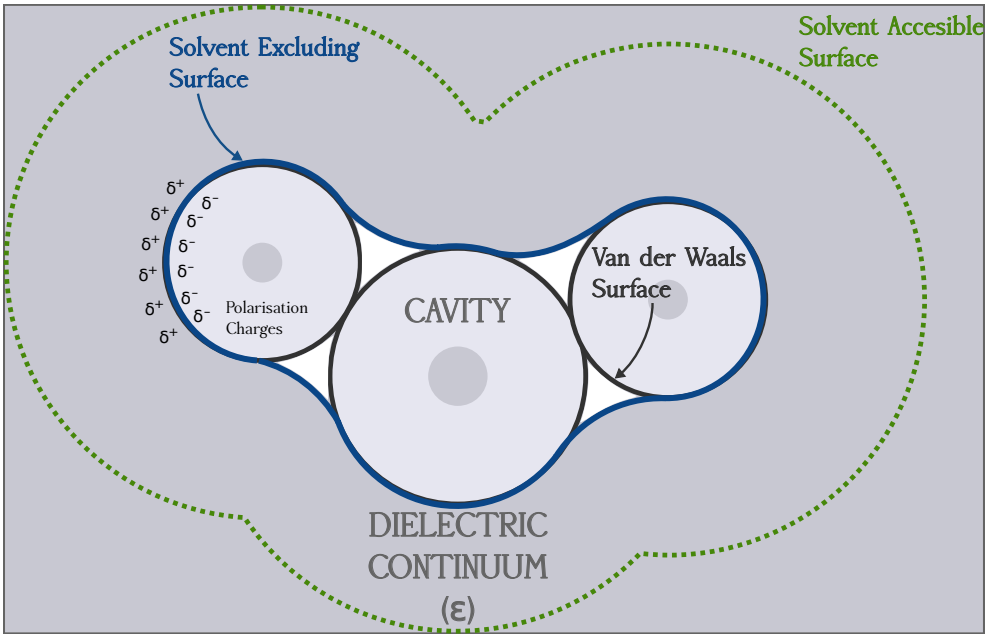

Figure 2.4: Schematic representation of a cavity in implicit solvent models. Black lines represent the van der Waals surfaces, the blue line is the limit that the solvent molecules have when approaching to the solute, and the green dotted line is the surface that is actually accessible by the solvent.

summation of different terms. One term is referred to the energy to create a cavity (see Figure 2.4) in the solvent where the system lies. Another term is related to the Van der Waals interactions between solute and solvent. And the last term is the electrostatic interaction between the continuum solvent and the molecule. Here, we can treat the solvent as different dielectric media: a conductor-like continuum or a polarisable continuum. In the former, the polarisation charges are calculated using a scaled-conductor approximation. Once we know the electric charge of the molecule, then we can calculate the charge on the surface by using a factor f, which depends on the dielectric constant.[123, 124] In the second approach, polarisation charges and potential from solvent

must follow the Poisson's equation—which relates scalar potentials with the functions that generate them—and are calculated numerically.[125–127]

Chapter 3

MECHANISTIC INSIGHTS INTO PROMOTED HYDROLYSIS OF PHOSPHOESTER BONDS BY $MoO_2Cl_2(DMF)_2$

Abstract

The phosphoester bond is a crucial structural block in biological systems, which occurrence is regulated by phosphatases. Molybdenum compounds have been reported to be active in phosphate ester hydrolysis of model phosphates. Specifically, $MoO_2Cl_2(DMF)_2$ was active in the hydrolysis of para-nitrophenyl phosphate (NPP), leading to hetero-polyoxometalate structures. We use density functional theory (DFT) to clarify the mechanism by which these species promote the hydrolysis of the phosphoester bond. The present calculations give insight into several key aspects of this reaction: *i)* the speciation of this complex previous to the interaction with the phosphate (DMF release, Mo−Cl hydrolysis and pH influence on the speciation); *ii)* the competition between phosphate addition and the molybdate nucleation processes; *iii)* and the mechanisms by which some plausible active species promoted this hydrolysis in dif-

ferent conditions. We described thoroughly two different pathways depending on the nucleation possibilities of the molybdenum complex: one mononuclear mechanism which is preferred in conditions in which very low complex concentrations are used; and a dinuclear mechanism, which is preferred with higher concentrations.

3.1 Introduction

The phosphoester bond (Figure 3.1) is ubiquitous in the biological systems. The formation and cleavage of this bond are essential in biological systems as it is used to transfer energy and as a binding mechanism between nucleotides in DNA and RNA. The remarkable stability of these systems lies in the extremely slow but favourable cleavage of the phosphodiester bond that allows an excellent control using enzymes.[128–130]Abnormal changes in these phosphorylation processes can cause several diseases like diabetes or cancer.

The phosphoester bond is also present in a variety of industrial organophosphorous species. Toxic organophosphorous compounds have been widely used as warfare agents and pesticides. They are the most accepted pesticides, allowing a better crop performance. Nevertheless, the exposure to these compounds is dangerous due to their capacity to accumulate in different environments and their harmful effects on mammals, like neurodegenerative diseases. Acute poisoning with these pesticides is responsible for hundreds of thousands deaths per year in developing countries. Warfare agents also produce these effects, but with a more immediate impact (nerve agents). The cleavage of the phosphoester bond in these compounds lead to non-toxic or lower toxic

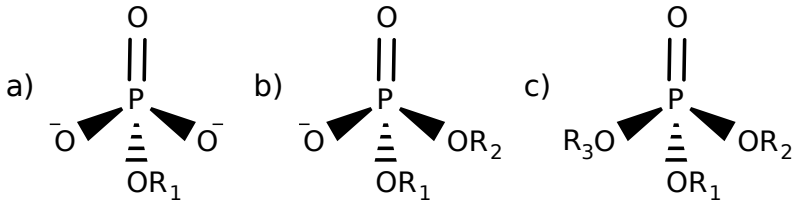

Figure 3.1: a) Phosphate monoester, b) Phosphate diester, c) Phosphate triester.

compounds.[131–136]

Diverse studies have focused on the promotion of the phosphoester hydrolysis to overcome the slow kinetics of the reactions that break apart these poisons. Between these approaches, metal-promoted hydrolysis has arisen with diverse positively charged metal complexes that have been proved to promote the cleavage of the phosphoester bond.[137–148] Among them, molybdenum stands out as it is an essential trace metal with interesting properties. Its high versatility in oxidation states, coordination numbers, stereo-chemistry, ability to form complexes with organic and inorganic ligands, and the formation of polynuclear clusters with bridging atoms makes molybdenum a promising candidate for several catalytic processes.[24, 149–151]

Many molybdenum-containing enzymes participate in essential redox reactions in the global C-, N- and S-cycles. For instance, its action is critical in the fixation of nitrogen (nitrogenases) and oxygen transfer between organic molecules (oxotransferases).[38, 152–154] Because of that, molybdenum oxides are used as soil fertilisers to overcome nitrogen deficiencies that worsen the plant growth.[155, 156] Considering this, it is easy to figure out why molybdenum compounds are good candidates to promote phosphate hydrolysis of organophosphorous pesticides.

In recent years, diverse molybdenum species like molybdocene derivatives,[14, 157–160] dioxomolybdates,[13, 15] and molybdates[161–163] have arisen as promoters of the hydrolysis of the phosphoester bond. Moreover, some species of molybdenum polyoxometalates have been reported to have antitumoural activity linked with its phosphatase activity.[9–12, 164–166].

In the case of the molybdocene derivatives, the proposed active species was $Cp_2Mo(OH)(H_2O)^+$ by hydrolysis of $MoCl_2$ with water. Abrantes and her colleagues showed that $MoO_2Cl_2L_2$ complexes accelerate the hydrolysis of paranitrophenyl phosphate (NPP) in water by a larger amount than the $MoO_2(CH_3)_2L_2$ counterparts (Figure 3.2).[13, 15] These chlorocompounds also lower the pH of the solution, a fact explained by the hydrolysis of the Mo−Cl bonds. The Mo−OH bonds formed are reactive and can in turn condense to form different polynuclear compounds.

The mechanism of the hydrolysis of phosphoester bond has been a hot topic during the last years.[128, 167–171] Depending on the substrate (nature of the leaving group, protonation state, number of phosphates in the molecule, etc.), the characteristics of the catalyst and the properties of the medium, the reaction could occur in very different ways. Studies with phosphoester dianions with good leaving groups in basic media showed a solvent-assisted dissociative transition state, while bad leaving groups preferred a substrate-assisted associative mechanism in which a phosphorane intermediate can be formed upon sufficient stabilisation (Figure 1.7).[172–179]

This mechanism implies a series of proton transfers to activate the nucleophilic attack and the leaving group.[44, 180] In a more acidic media, the monoanionic phosphate transfers the proton of the adjacent oxygens to the leaving group and activates the cleavage of the phosphoester bond.[181–183] The cleavage of a phosphodiester bond molecules is a more difficult task and suggests a more compact transition state.[184] Catalysts and promoters can facilitate one mechanism above the others and only with accurate computational

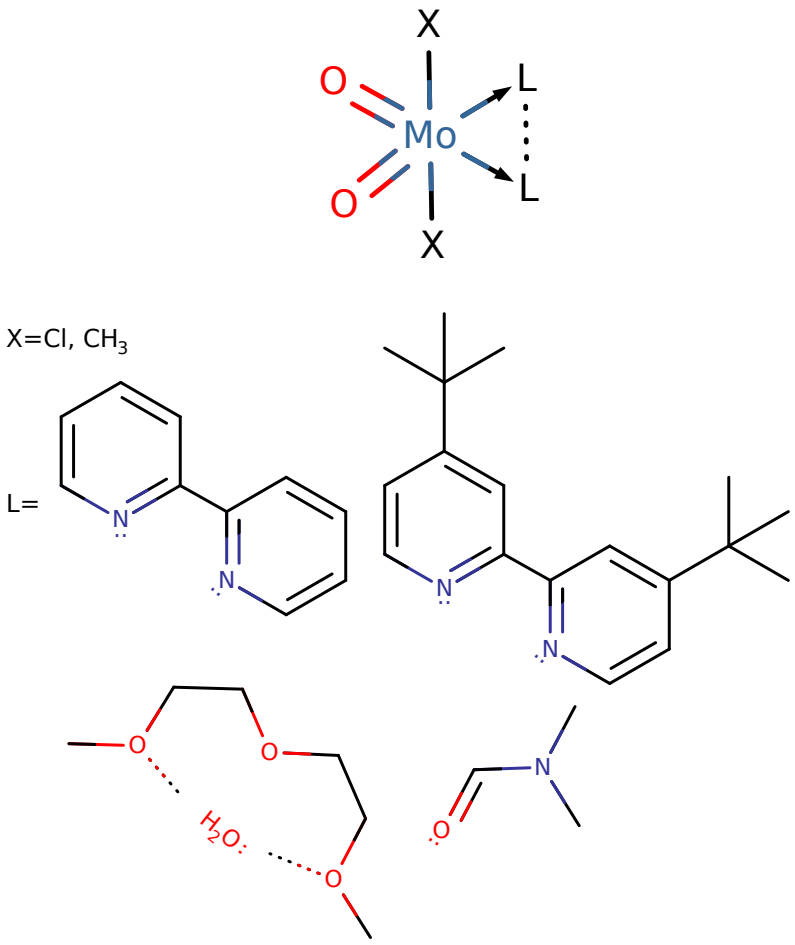

Figure 3.2: Studied complexes by Abrantes and colleagues[13, 15] for the NPP hydrolysis.

methodology we can discern the ongoing mechanism in every case.

Therefore, the aim of this work is to use computational methods to give insight into the mechanism by which this kind of molybdenum complexes hydrolyse phosphate esters, using the NPP mentioned above as a model substrate. We took the species used in the works of Abrantes group as models of these interesting complexes.[13, 15] Explaining why the hydrolysis of this phosphatase substrate was accelerated by compounds with the formula $MoO_2X_2L_2$ will help to rationalise and optimise such catalysts for efficient performance.

3.2 Computational Details

Calculations were carried with the Amsterdam Density Functional program—developed by Baerends, Ziegler, and co-workers—, version 2013.01,[185–187] and the Gaussian 16 Revision C.01 simulation package.[188] In the ADF calculations, we selected the BP86 Density Functional Theory functional, which uses the Vosko-Wilk-Nusair exchange-correlation potential[76] with the Generalised Gradient Approximation exchange correction reported by Becke[85] and the Perdew's correlation correction.[189] In these calculations, we used a triple-ζ plus two polarisation functions basis set and a relativistic frozen core potential—corrections made with scalar-relativistic Zero-Order Regular Approximation.[190, 191] Implicit solvent effects were introduced with continuous model COSMO with standard parameters.[125–127] We also used the Nudged Elastic Band method implemented in ADF to search for transition states where the reaction coordinate was challenging to scan.

Gaussian calculations were made with the B3LYP DFT hybrid func-

tional, which uses the Becke's three parameter exchange-correlation that mixes Hartree-Fock exact exchange with Slater's and Becke's exchange functional;[84] and the local correlation VWN functional with the non-local Lee, Yang and Parr correlation functional.[87] The Los Alamos National Laboratory 2 effective core potential with double zeta (LANL2DZ) and f polarisation functions was used for the molybdenum atoms,[192–196] and the double-zeta split valence basis set including d and p polarisation functions and s and p diffuse functions for non-hydrogen atoms 6-31+G** was used for the rest of the atoms. Transition state geometries were optimised and characterised by frequency calculations. The intrinsic reaction coordinate was followed to obtain the reactants and products geometries, followed by unconstrained optimisations.[197, 198] Energies of mechanistically relevant results were refined using the 6-311++G(3*df*,2*p*) basis set.[199] Polarisable Continuum Model was used to account the implicit solvent.[123, 124] Dispersion effects were included using the third version of Grimme dispersion with the Becke-Johnson damping.[98]. These methodologies with and without single point calculations will be referred as "B3LYP" and "B3LYP+", respectively.

Since the free energies were calculated as ideal gases at the standard state of 1 atm, we included a term in the estimation of the free energy change in solution to consider the volume change attributable to the transformation from 1 atm to 1 M.[200] The correction can be expressed as follows:

$$\Delta G^{0\rightarrow *} = \Delta nRT\ln(22.46) \tag{3.1}$$

This correction is relevant in processes in which the number of species

change ($\Delta n \neq 0$) throughout the reaction. A second term was added to include an entropic factor that accounts for the actual concentration of 55.34M of water in liquid water:[200]

$$\Delta G^{*\rightarrow 1} = mRT\ln(55.34) \tag{3.2}$$

The wave function for the chemical structures was analysed in order to explore the topology of the electron density with the Quantum Theory of Atoms in Molecules (QTAIM).[112] Additionally, non-covalent interactions were analysed using the non-covalent interaction (NCI) index.[201] This method allows us to exhibit the weak interactions representing the reduced gradient of electron density map with the second value of the Hessian matrix. Both analyses have been plotted by using the AIMAll software.[202]

3.3 Results and Discussion

$MoO_2Cl_2(DMF)_2$ Speciation

As Tomé *et al.*[15] pointed out, the initial $MoO_2Cl_2(DMF)_2$ does not keep its structure in solution. They reported the decoordination of DMF by ^{1}H NMR, the acidification of the solution due to the hydrolysis of the Mo−Cl bond, and the formation of isopolyoxometalates and heteropolyoxometalates.

With this information, the first step was to elucidate the species present in the medium when the hydrolysis-promoting agent is dissolved in water and try to reproduce the available experimental evidence. By analysing the relative

stability of the different mononuclear complexes, we can reduce the number of possible species participating in the promoted hydrolysis of NPP.

Molybdenum(VI) species have a coordination number varying from 4 to 6. The most known species, the molybdate ($MoO_4{}^{2-}$), has a tetrahedral structure. Acidification of the media leads to the protonation of the coordinated ligands and increases the electrophilicity of the metal atom, which can now expand its coordination sphere by the inclusion of solvent molecules or other species available in the medium. In these structures, it is already known that the proton transfer between ligands of the same complex or with the participation of solvent molecules is widespread, as well as the condensation of water molecules, leading to a great variety of complexes.[203] Expanding the coordination sphere, proton transfers, and water condensations could lead to polyoxometalate structures if the included ligand is another molybdate species.

Because of that, we took into account the following processes with different coordination numbers:

- Release of DMF:
  $MoO_2Cl_2(DMF)_2 \xrightarrow[-DMF]{H_2O} MoO_2Cl_2(DMF)_{0-1}(H_2O)_n$
- Hydrolysis of the Mo−Cl bond:
  $MoO_2Cl_2(H_2O)_{0-2} \xrightarrow[-Cl^-]{OH^-} MoO_2Cl_{0-1}(OH)_{1-2}(H_2O)_n$
- Protonation of the complex in acidic media:
  $MoO_2(OH)_2(H_2O)_{0-2} \xrightarrow[-H_2O]{H_3O^+} [MoO_2(OH)_{0-1}(H_2O)_n]^{1-2+}$
- Intramolecular proton transfers:
  $MoO_2(OH)_{0-2}(H_2O)_n]^{0-2+} \longrightarrow [MoO_x(OH)_y(H_2O)_z]^{0-2+}$

A general scheme of the accounted reactions is depicted in Figure 3.3. The energetics of these theoretical calculations involving mononuclear species are presented in the Table 3.1, taking the initial $MoO_2Cl_2(DMF)_2$ complex as a reference state. First, we can appreciate that after the release of both DMF ligands, the tetrahedral coordination of MoO_2Cl_2 is more favourable. The following hydrolysis of the Mo−Cl bonds was observed experimentally and our calculations support this finding. In fact, the hydrolysis of the two Mo−Cl bonds was very favourable energetically, getting the $MoO_2(OH)_2$ complex, free DMF in solution, and an acidic media due to the OH^- consumption.

In those acidic conditions, the most stable mononuclear structure is referred to be $[MoO_2(OH)(H_2O)_3]^+$. Our calculations show that the pentacoordinated and tetracoordinated forms are close in energy, which is expected as a consequence of the rich speciation of molybdenum species in acidic media. As expected the tetrahedral coordination is preferred for neutral pH, and the octahedral coordination became more accessible when the pH was lowered and the ligands were protonated. We also observed that intramolecular proton transfers result in species that are very close in energy, as was expected.

Nevertheless, if the concentration of molybdenum complexes is enough, nucleation processes are favoured by the acidic media. Because of that, after identifying the most stable mononuclear species, we have to consider the known nucleation processes that molybdate and its protonated analogues—$HMoO_4^-$ and $MoO_2(OH)_2$—suffer at low pH. In these conditions and after several processes involving coordination of ligands and proton transfers with the solvent, mononuclear structures could form different structures of polyoxometalates

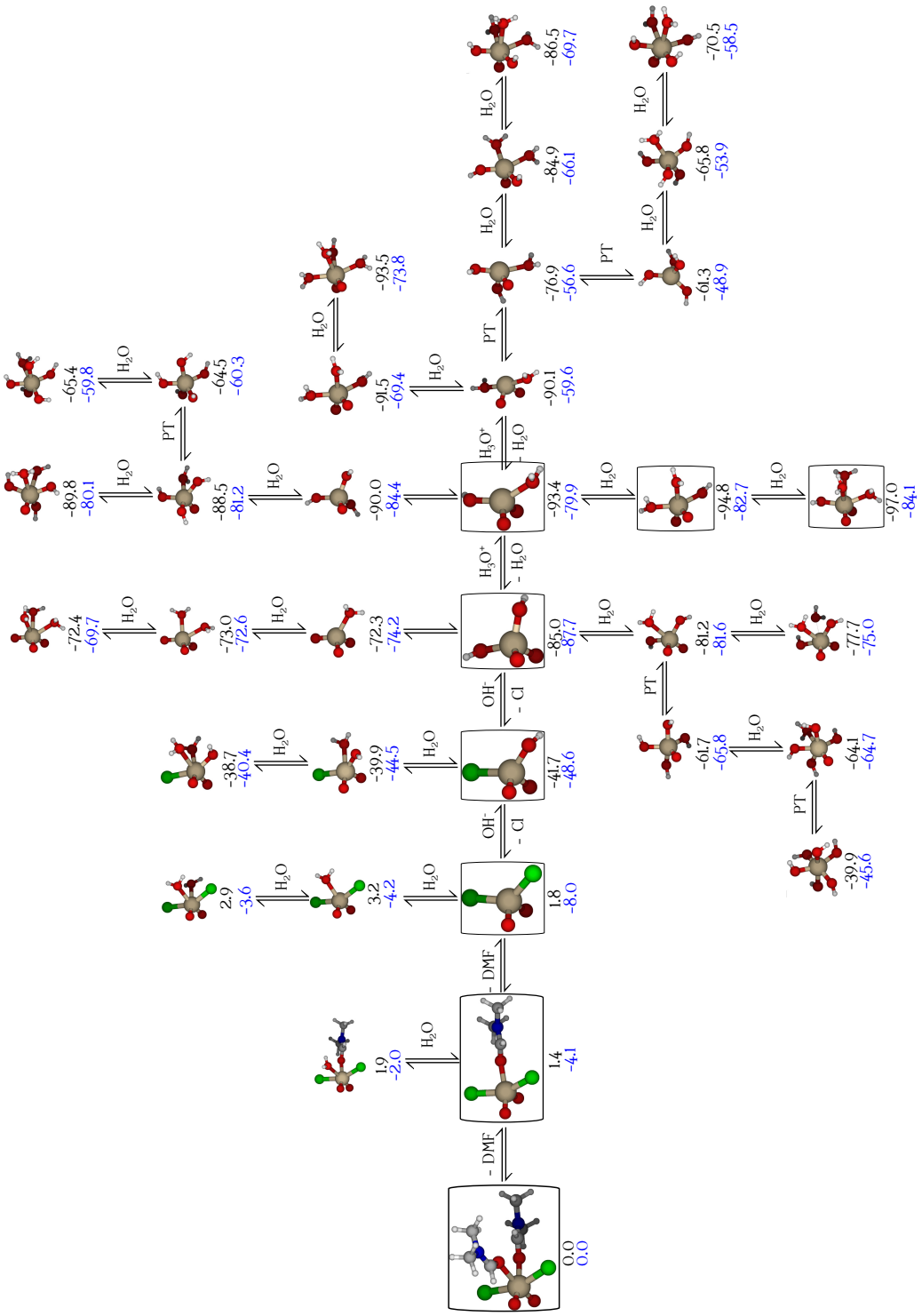

Figure 3.3: General scheme of the mononuclear species that can be formed in solution by ligand release, hydrolysis of Mo-Cl bond, acidification and internal proton transfers (PT). Relative free energies are in kcal/mol. In black, calculated with B3LYP methodology; in blue, calculated at BP86/TZ2P/COSMO; most relevant species are highlighted.

Table 3.1: Relative energies in kcal/mol of different complexes varying the coordination number (CN) of Mo.[1]

	ΔH^2			ΔG^2			ΔH^3			ΔG^3		
Species	CN: 4	CN: 5	CN: 6	CN: 4	CN: 5	CN: 6	CN: 4	CN: 5	CN: 6	CN: 4	CN: 5	CN: 6
$MoO_2(Cl)_2(DMF)_2$	—	—	0.0	—	—	0.0	—	—	0.0	—	—	0.0
$MoO_2(Cl)_2(DMF)(H_2O)_{0-1}$	—	10.1	5.3	—	1.4	1.9	—	6.7	3.7	—	−4.1	−2.0
$MoO_2(Cl)_2(H_2O)_{0-2}$	20.6	16.0	9.79	1.8	3.2	2.9	16.2	12.5	9.9	−8.0	−4.2	−3.6
$MoO_2(Cl)(OH)(H_2O)_{0-2}$	−24.8	−28.5	−34.2	−41.7	−39.9	−38.7	−28.9	−30.2	−32.2	−48.6	−44.5	−40.4
$MoO_2(OH)_2(H_2O)_{0-2}$	−69.1	−71.4	−73.9	−85.0	−81.2	−77.7	−72.2	−72.8	−72.7	−87.7	−81.6	−75.0
$MoO_3(H_2O)_{1-3}$	−56.7	−63.4	−68.7	−72.3	−73.0	−72.4	−58.8	−64.2	−66.2	−74.2	−72.6	−69.7
$MoO(OH)_4(H_2O)_{0-1}$	—	−52.0	−61.8	—	−61.7	−64.1	—	−55.8	−61.8	—	−65.8	−64.7
$Mo(OH)_6$	—	—	−39.0	—	—	−39.9	—	—	−43.5	—	—	−45.6
$[MoO_2(OH)(H_2O)_{1-3}]^+$	−79.2	−87.1	−95.9	−93.4	−94.8	−97.0	−66.5	−75.7	−82.4	−79.9	−82.7	−84.1
$[MoO(OH)_3(H_2O)_{0-2}]^+$	−76.5	−81.1	−88.3	−90.0	−88.5	−89.8	−71.8	−74.3	−78.4	−84.4	−81.2	−80.1
$[Mo(OH)_5(H_2O)_{0-1}]^+$	—	−57.9	−64.5	—	−66.4	−65.4	—	−57.1	−61.4	—	−62.7	−59.8
$[MoO_2(H_2O)_{2-4}]^{2+}$	−77.8	−84.9	−94.1	−90.1	−91.5	−93.5	−50.7	−66.8	−75.5	−59.6	−69.4	−73.8
$[MoO(OH)_2(H_2O)_{1-3}]^{2+}$	−65.3	−79.2	−88.2	−76.9	−84.9	−86.5	−47.0	−62.0	−72.6	−56.6	−66.1	−69.7
$[Mo(OH)_4(H_2O)_{0-2}]^{2+}$	−50.1	−61.3	−72.7	−61.3	−65.8	−70.5	−39.4	−51.4	−60.2	−48.9	−53.9	−58.5

[1]All energies are calculated taking $MoO_2(Cl)_2(DMF)_2$ as reference state. Species are related by release of DMF, hydrolysis of the Mo−Cl bond, protonation of hydroxides and intramolecular proton transfers as stated in the text.
[2] B3LYP-GD3BJ/LANL2DZ(F)/6-31+G**/PCM
[3] BP86/TZ2P/COSMO

within a complex mechanism.[204]

Phosphate vs Molybdate Addition

Once we have narrowed the spectrum of different mononuclear structures that can be present in solution in a significant concentration, we proceed to study a key point of this reaction: the addition of the substrate to the promoter. Before we examine the interaction of the NPP with different species of molybdenum(VI) we had to calculate which species would most likely interact with the phosphate.

Knowing that the oxides of molybdenum(VI) form heteropolyoxometalates when phosphate is present in acidic media and that our ultimate product has a Keggin structure, we compared the mechanism of formation of the Lindqvist $[Mo_6O_{19}]^{2-}$ and Keggin ($[PMo_{12}O_{40}]^{3-}$) molybdenum clusters to see when the interaction of the phosphate with the molybdate species is favoured and the possible competition with the nucleation processes. In the work of Vilà-Nadal *et al.*,[205] they pointed out that the formation of $[Mo_2O_7]^{2-}$ is more favourable than the phosphate addition to the mononuclear species. The later incorporation of the phosphate to the dinuclear species was favoured over the formation of the trinuclear structure. The formation of this dinuclear species incorporating phosphate ultimately led to the formation of the Keggin anion. In the absence of phosphate nucleation processes on the trinuclear structure would lead to the Lindqvist anion. Even though the protonation states are not the same in that study than in our system, the mechanisms of nucleation of molybdates at different protonation states are similar and proton transfers

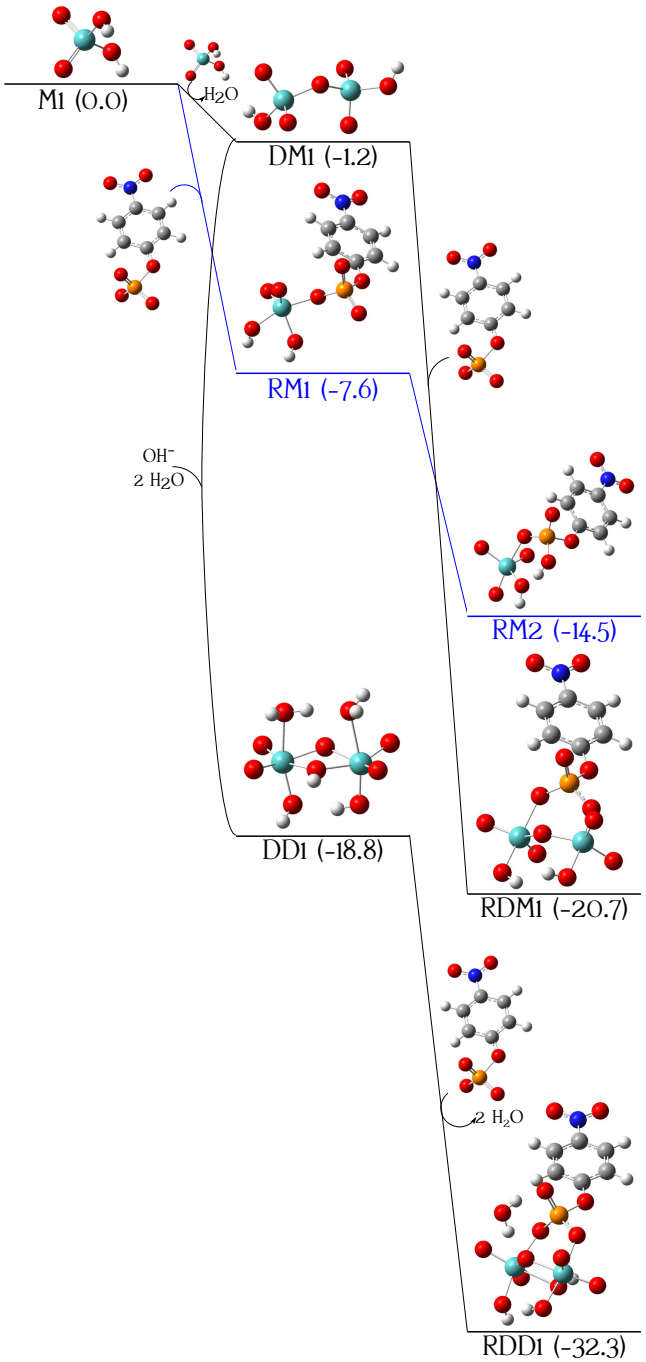

Figure 3.4: Comparison between the incorporation of NPP to the mononuclear species and to the dinuclear species calculated using B3LYP+ methodology. Relative free energies are in kcal/mol.

between the molybdate and the solvent or another ligand of the molybdate structure are very fast and frequent.

Since the $[Mo_2O_6\mu\text{-}O)]^{2-}$ is the result of the condensation of two $[MoO_3(OH)]^-$ into this dinuclear species and a water molecule, we have studied a similar process starting from the neutral species $[MoO_2(OH)_2]$(M1) to give $[Mo_2O_4\mu\text{-}O(OH)_2]$(DM1). This process was compared with the addition of the phosphate substrate as seen in Figure 3.4. As we can see in Table 3.2 the energetics ($\Delta G = -14.5$ kcal/mol) of this phosphate addition—followed by an internal proton transfer—are favourable over the condensation of two M1 molcules to form the dinuclear species DM1 ($\Delta G = -1.2$ kcal/mol). However, the very favourable interaction of DM1 with the phosphate substrate ($\Delta G = -19.5$ kcal/mol) tips the scales in favour of the formation of the dinuclear species.

Besides this dinuclear structure, we also searched for different bridging structures varying the coordination number of Mo as we saw that higher coordination numbers are available within this protonation state. Some double bridged structures like the $[Mo_2O_4\mu\text{-}O(OH)_3\mu\text{-}OH)(OH_2)_2]$(DD1) are more favourable than the $[Mo_2O_4\mu\text{-}O)(OH)_2]$ species. This species can be related to DM1 by the incorporation of a bridging hydroxide and two water molecules, increasing the coordination number of the molybdenum atoms in an exergonic process ($\Delta G = -17.6$ kcal/mol). This double bridged structures are stable when at least one of the bridging oxygen atoms is protonated. This species has two water molecules that can be easily replaced by the oxygen atoms of the NPP ($\Delta G = -13.5$ kcal/mol) to give RDD1. This species is more stable than the direct coordination of the NPP moiety to DM1 to give the monobridged species

RDM1, which is 11.6 kcal/mol over RDD1.

Table 3.2: Relative energies in kcal/mol for the species involved in the phosphate-molybdate addition competition. Single-point energy estimations using 6-311++G(3*df*,2*p*) basis set from geometries optimised at B3LYP-GD3BJ/6-31+G**/PCM level of theory.

Species	ΔH	ΔG
M1	0.0	0.0
RM1	−19.7	−7.6
RM2	−25.9	−14.5
DM1	−7.0	−1.2
RDM1	−38.5	−20.7
DD1	−49.4	−18.8
RDD1	−59.4	−32.3

Taking all these data into account, the main candidate for promoter of this reaction is the [$Mo_2O_4\mu$-O)$(OH)_3\mu$-OH)$(OH_2)_2$]. Nevertheless, we also studied the process with an analogous structure of the species described by Vilà-Nadal *et al.* in which both molybdenum atoms are pentacoordinated, each bonding to an oxygen atom of the phosphate structure (RDM2). This structure can be related with RDD1 by releasing three hydroxides in a very endergonic process (ΔG=94.3 kcal/mol). Also, we studied the hydrolysis with the most stable mononuclear structure to see the energetics of both paths. This competition could explain the slower activity of the promoter with much lower promoter concentration, which disfavours polynuclear species.

Phosphate Ester Hydrolysis

Without Molybdenum Species

As we pointed out in the introduction, the reaction mechanism of the hydrolysis of phosphoester bonds is not straightforward as it seems. We calculated initial

reaction profiles without molybdenum species to have a reference using the same methodology to compare our results, as well as a starting point to search for transition states or intermediates using the molybdenum species.

We explored both pathways well described by Duarte *et al.* in the literature:[44, 180] the substrate-assisted and the solvent-assisted pathways. In our calculations, we found the transition state structures for both mechanisms (Figure 3.5) along with the reactant and product structures, obtained by a relaxed optimisation of the final structures after an intrinsic reaction coordinate calculation. As expected, the transition state for the substrate-assisted pathway involves a proton transfer to the substrate, acting as a Brönsted base. Water molecules impeded this proton transfer in the solvent-assisted transition state, stabilising the proton on the nucleophile. In principle, without molybdenum(VI) the preferred pathway is the most dissociative one—the solvent-assisted pathway—which is in accordance with experimental markers and with some of the latest theoretical calculations.[44, 128, 180]

With Molybdenum Species

Taking both transition state geometries without promoter as a starting point, we searched for transition state structures with mononuclear and dinuclear species. Nevertheless, we obtained intermediate structures in which the phosphorous atom is forming a phosphorane. That can be rationalised by the fact that the interaction of molybdenum, a Lewis acid, with the oxygen atoms of the phosphate increases the electrophilicity of the phosphorous atom, being more prone to a nucleophilic attack. This fact points to a great stabilisation of

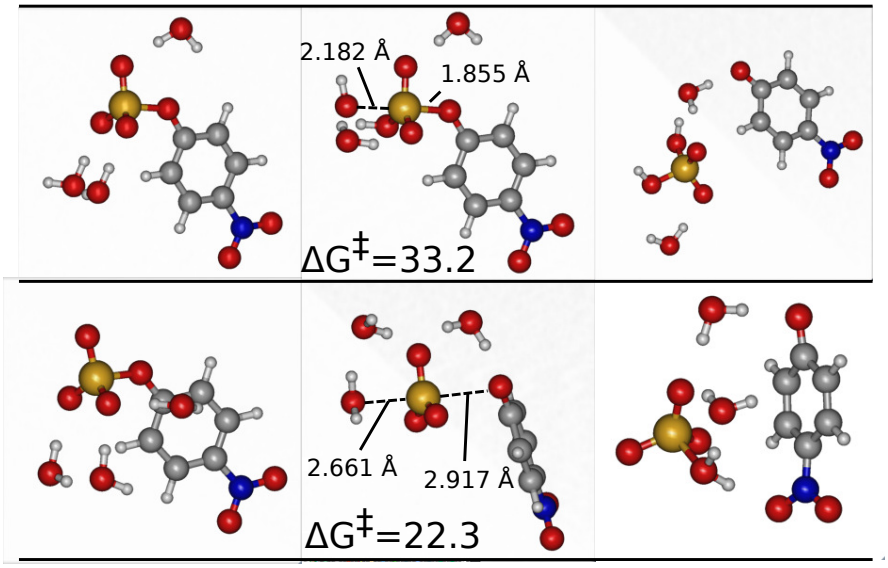

Figure 3.5: Representative stationary points—left, reactants; middle, transition state; right, products—for substrate-assisted—up—and solvent-assisted—down—pathways for the NPP hydrolysis calculated at B3LYP+ methodology. Activation free energies are in kcal/mol.

an associative substrate-assisted pathway and probably discard a dissociative pathway. Here, we mainly present associative pathways involving the mononuclear and dinuclear molybdenum species.

Pathway Involving Mononuclear Species

The exergonic coordination (−7.6 kcal/mol) of the NPP to the metal atom of M1 through an oxygen atom gives a Lewis adduct with a distorted trigonal bipyramidal Molybdenum and a tetrahedral phosphorous (RM1), as seen in Figure 3.4. An intramolecular proton transfer from a hydroxide of the coordination sphere of the metal to the phosphate—leading to RM2—is favoured, releasing 6.9 kcal/mol. Starting from there, we obtained structures in which

molybdenum expanded its coordination number easily using neighbouring oxygen atoms and hindering the nucleophilic attack. For the hydrolysis reaction to occur, this nucleophilic attack has to happen from this RM2 structure, giving an energetically higher intermediate in which the phosphorous atom is coordinatively saturated. The free energy profile for this phosphorane formation and the consequent leaving group departure can be seen in Figure 3.6.

Table 3.3: Relative energies (in kcal/mol), relevant distances (Å) and angles (deg) for the species involved in the mononuclear mechanism. Single-point energy estimations using 6-311++G(3df,2p) basis set from geometries optimised at B3LYP-GD3BJ/6-31+G**/PCM level of theory.

Species	ΔH	ΔG	P⁻O(LG)	P–O(Nu)	O(LG)–P–O(Nu)
RM2	0.0	0.0	1.702	3.094	93.9
TSM1	17.0	19.2	1.746	2.132	164.7
IM1	16.7	18.3	1.835	1.828	166.5
TSM2	16.7	18.0	2.217	1.704	166.9
PM1	−12.0	−13.7	3.625	1.534	34.6

Once we have this structure in which the two negatively charged oxygen atoms of the phosphate are stabilised by positive charges—by the protonation mentioned above of the phosphate as a Brönsted base and the adduct formation with the metal centre as a Lewis acid—the rise in electrophilicity of the phosphorous atom leads to the phosphorane formation through an intramolecular attack. Because of that, a phosphorane intermediate (IM1) is formed with low energy (18.3 kcal/mol over RM2) compared to the non-catalysed mechanism. Despite that fact, the phosphorane seems to be barely below the transition state structures in terms of energy, and its lifetime should be very short. Specifically, the formation of this hypervalent structure and the phosphoester bond breaking have a similar free energy above the reference state

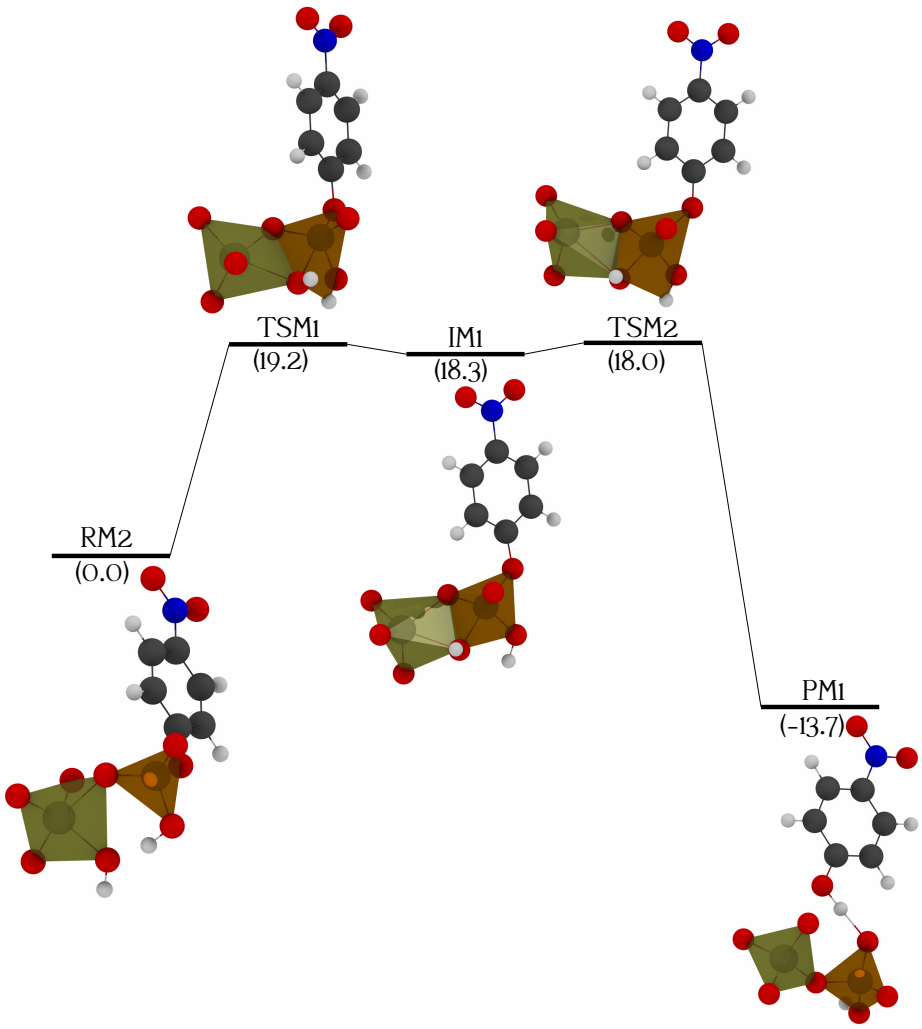

Figure 3.6: Calculated free energy profile for NPP hydrolysis using mononuclear molybdenum species at B3LYP+ methodology. Relative free energies are in kcal/mol.

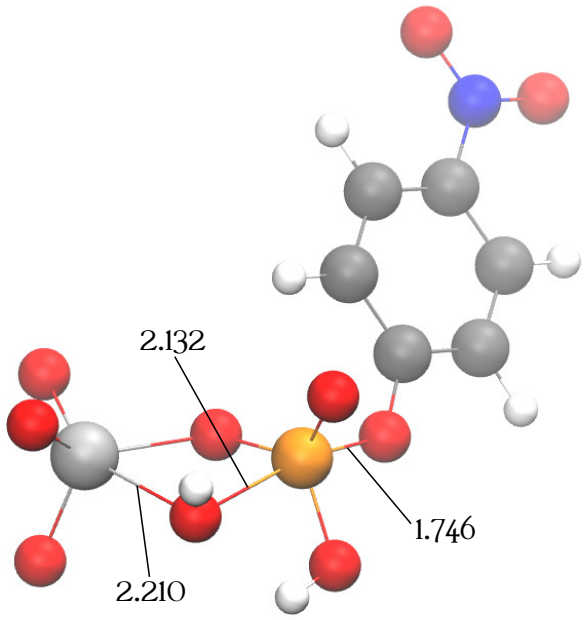

Figure 3.7: Transition state geometry corresponding to the phosphorane structure formation of the mononuclear mechanism. Optimised using B3LYP methodology. Distances in Å.

(19.2 kcal/mol and 18.0 kcal/mol for TSM1 and TSM2, respectively) with the phosphorane intermediate within a narrow range of free energy to these transition states. The breaking of the P−O bond comes along with an asynchronous proton transfer from one of the protonated oxygen atoms of the phosphate and the decoordination of the shared hydroxide from molybdenum, getting $(HPO_4)MoO_3$ in which both centres are tetrahedral.

The associative character of this pathway is highlighted by the existence

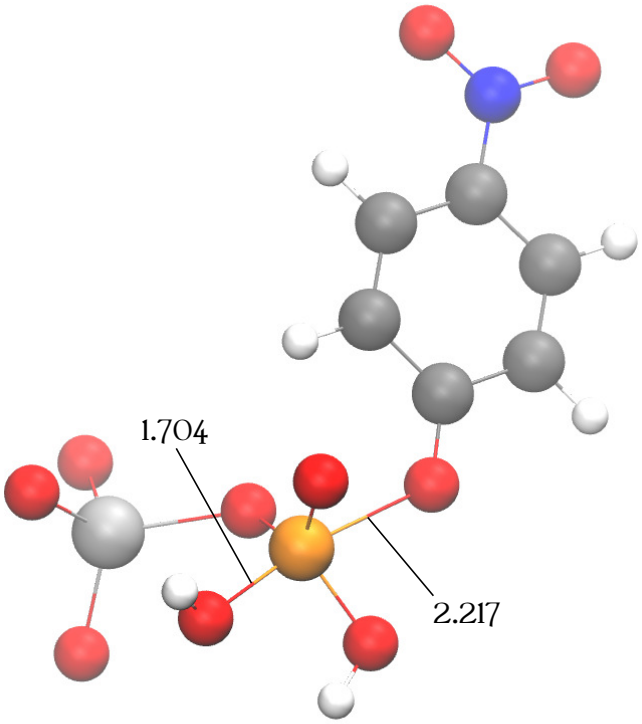

Figure 3.8: Transition state geometry corresponding to the phosphorane structure rupture of the mononuclear mechanism. Calculated using B3LYP methodology. Distances in Å.

of the phosphorane intermediate, in which the distances of the phosphorous atom with the nucleophile and the leaving group are quite similar: 1.828 and 1.835 Å, respectively. Energetic and geometric data are collected in Table 3.3.

This pathway is favourable over the direct NPP hydrolysis as the interaction of the molybdate structures with the substrate is exergonic, and the transition state has a lower barrier—approximately 19 kcal/mol—than the non-catalysed process. With this information, we could explain the promoter's

catalytic activity when the promoter's concentration is very low, disfavouring the formation of dinuclear species.

Pathway Involving Double-Bridged Dinuclear Species

As we stated previously, the formation of the double-bridged dinuclear species RDD1 incorporating the phosphate is favoured by 32.3 kcal/mol. Because of that, this pathway has a lower starting point than the mononuclear pathway, and the entire pathway is favoured over the hydrolysis with mononuclear species.

The saturation of the molybdenum atoms coordination in RDD1 makes a direct interaction between them and the nucleophile impossible. Because of that, an incoming water molecule can be stabilised by hydrogen bonds to the molybdate moiety favouring a correct intermolecular nucleophilic attack. Eventually, this interaction can result in the subtraction of a proton by the substrate, increasing the nucleophilic character of the incoming nucleophile. The proton transfer and the hydroxide attack occur concertedly through an associative TSDD1 transition state located at 22.8 kcal/mol above the reactant state. This process in which the substrate acts as a Brönsted base catalyst is depicted in Figure 3.9.

The associative character of the transition state is confirmed by the distances to the leaving group (1.827 Å) and to the nucleophile (2.335 Å), very close to the reference state without molybdenum (1.855 and 2.182 Å). The process is more asynchronous than the uncatalysed reaction, being the transition state closer to the product state, in which the proton transfer has almost

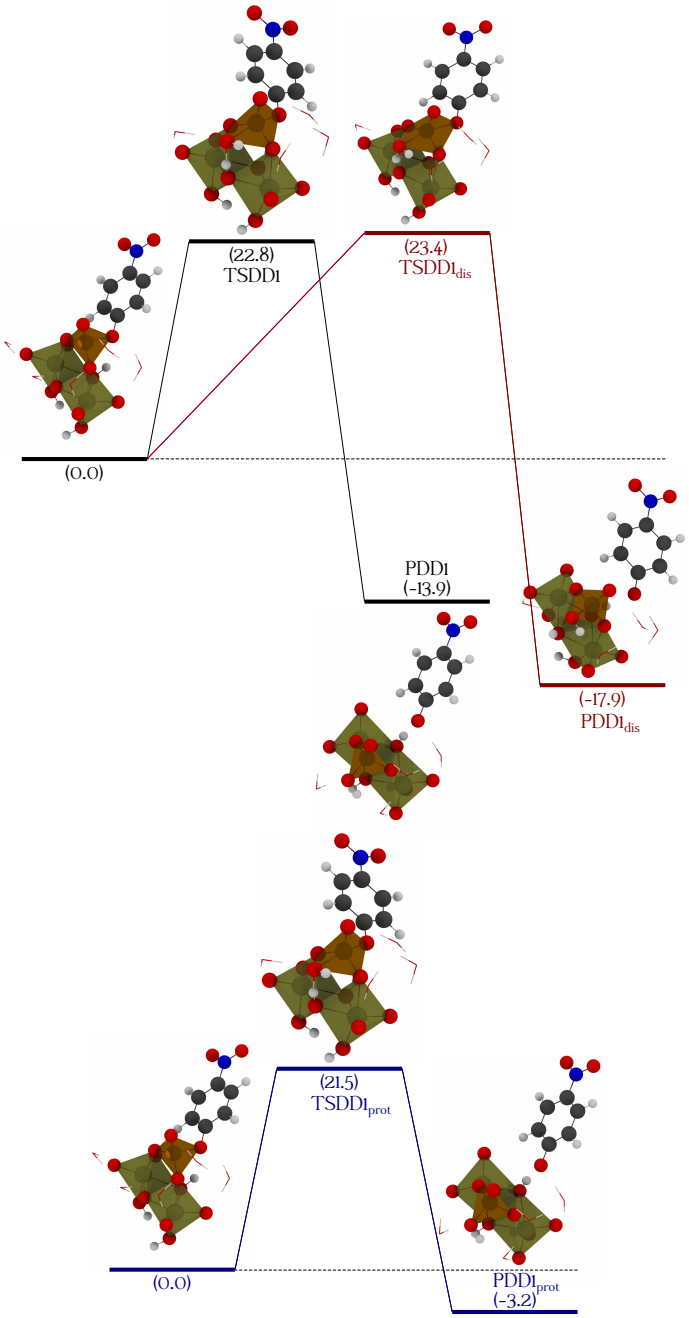

Figure 3.9: Calculated free energy profiles for NPP hydrolysis using higher coordination mode dinuclear molybdenum species using B3LYP+. In black, associate mechanism; in red, dissociative mechanism; in blue, mechanism using a protonated species. Relative free energies are in kcal/mol.

Table 3.4: Relative energies (in kcal/mol), relevant distances (Å) and angles (deg) for the species involved in the dibridge dinuclear mechanisms with five explicit water molecules. Single-point energy estimations using 6-311++G(3df,2p) basis set from geometries optimised at B3LYP-GD3BJ/6-31+G**/PCM level of theory.

Species	ΔH	ΔG	P−O(LG)	P−O(Nu)	O(LG)−P−O(Nu)
RDD1	0.0	0.0	1.723	4.309	148.46
TSDD1	18.2	22.8	1.827	2.335	169.50
PDD1	−18.0	−13.9	3.589	1.641	164.60
$RDD1_{prot}$	0.0	0.0	1.682	3.657	164.20
$TSDD1_{prot}$	20.8	21.5	1.948	1.912	168.40
$PDD1_{prot}$	−2.2	−3.2	3.374	1.645	160.00
$RDD1_{diss}$	0.0	0.0	1.712	3.737	159.37
$TSDD1_{diss}$	22.4	23.4	2.348	2.192	167.00
$PDD1_{diss}$	−18.2	−17.9	3.599	1.643	161.70

entirely happened and the leaving group is close to be released. The whole process is exergonic by 13.9 kcal/mol. Further energetic and geometric details are shown in Table 3.4.

Besides this transition state, we found a dissociative transition state with a higher energetic barrier (23.4 kcal/mol), depicted in Figure 3.9. This transition state is very close in energy to the associative one, but the distances to the leaving group (2.348 Å) and nucleophile (2.192 Å) are somewhat different. In this mechanism, the proton is not substracted by the time the system reaches the transition state, and the leaving group bond is almost broken at that stage without the intervention of the nucleophile.

As we will see in the following chapter, experimental data from a polyoxometalate decomoposition in presence of phosphate pointed to the existence of a dimeric structure that can be related to RDD1 through a protonation of RDD1. Because of that, we calculated the same pathway starting from

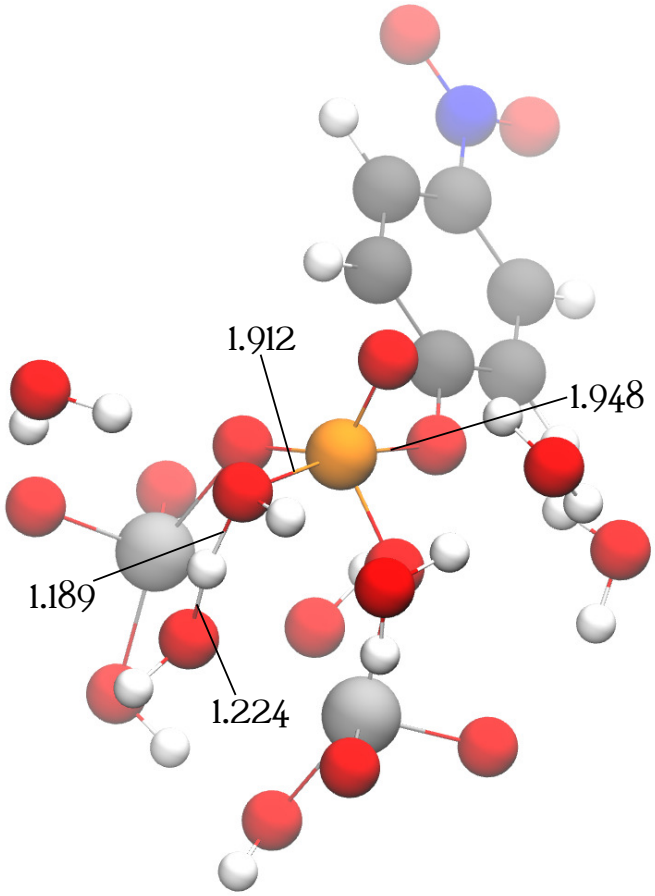

Figure 3.10: Transition state geometry corresponding to the TSDD1$_{prot}$ structure. Optimised using B3LYP methodology. Distances in Å.

RDD1$_{prot}$, in which both bridging oxigens are protonated. This pathway showed a lower energetic barrier, with the transition state 21.5 kcal/mol over the reactant state. This transition state is also depicted in Figure 3.9 and, in more detail, in Figure 3.10.

This synchronous transition state in which the nucleophile and leaving group bonds are formed and broken at the same time is possible due to a lower

basicity of the bridging oxygen when protonated. The associative character of this transition state is evident as it has distances of 1.948 and 1.912 Å to the leaving group and the nucleophile, respectively. These distances differ greatly from TSDD1 as the leaving group is much closer to the phosphorous atom and the nucleophile bond is weaker. In addition, the proton has its bond partially broken (1.189 Å) whilst forming a new bond to the substrate (1.224 Å). As a result, a highly ordered transition state is obtained. In this pathway, the total overcome of the reaction is less exergonic than the previously described mechanisms (ΔG=$-$3.2 kcal/mol).

In studying these mechanisms, we included four extra explicit water molecules, as the specific hydrogen bond interactions can be very relevant in evaluating the energetic barrier. In fact, the energetic barrier of the dissociative transition state decreases by 5.2 kcal/mol upon the addition of four water molecules. On the other hand, we saw some mixed results in the associative pathways. While the TSDD1 transition state stayed almost invariant—decreased from 23.4 kcal/mol to 22.8 kcal/mol—the TSSD1$_{prot}$ transition state decreased 5.8 kcal/mol with the addition of four explicit water molecules. This is in agreement with the character of the transition states, as the dissociative and protonated ones need a higher stabilisation of the nucleophile by water molecules as it is farther from the phosphorous atom than in TSDD1. The data for this mechanism without the extra water molecules are collected in Table 3.5 and its activation energies can be compared in Figure 3.11.

We have made single-point calculations with other suitable functionals to validate our results. We used BP86 functional as it has been used in recent

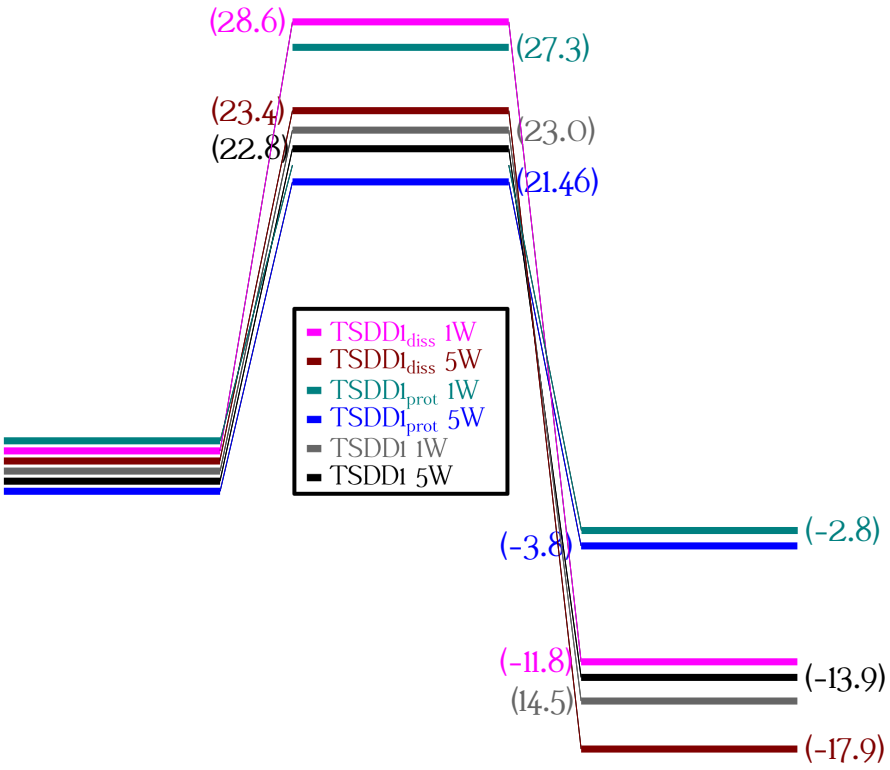

Figure 3.11: Calculated free energy profiles for NPP hydrolysis using higher coordination mode dinuclear molybdenum species with and without extra explicit water molecules. Single-point energy estimations using 6-311++G(3df,2p) basis set from geometries optimised at B3LYP-GD3BJ/6-31+G**/PCM level of theory.

studies involving molybdate and phosphate,[205] and M06-2X as it is a relatively modern functional that has been widely used in organometallic reactions. For these single-point calculations, we used the geometries of the relevant transition states optimised at B3LYP-GD3BJ/LANL2DZ(F)/6-31+G**/PCM level of theory. We compared them with the uncatalysed reaction, as shown in Table 3.6.

A catalytic effect is clearly depicted in the table, with lower-energy associa-

Table 3.5: Relative energies (in kcal/mol), relevant distances (Å) and angles (deg) for the species involved in the dibridge dinuclear mechanisms with one explicit water molecule. Single-point energy estimations using 6-311++G(3df,2p) basis set from geometries optimised at B3LYP-GD3BJ/6-31+G**/PCM level of theory.

Species	ΔH	ΔG	P−O(LG)	P−O(Nu)	O(LG)−P−O(Nu)
RDD1	0.0	0.0	1.698	3.572	155.62
TSDD1	20.5	23.0	1.842	2.253	168.17
PDD1	−13.8	−14.5	4.957	1.659	132.72
$RDD1_{prot}$	0.0	0.0	1.676	3.354	174.43
$TSDD1_{prot}$	23.1	27.3	1.904	1.954	167.32
$PDD1_{prot}$	−2.9	−2.8	5.027	1.662	137.95
$RDD1_{diss}$	0.0	0.0	1.716	4.545	145.72
$TSDD1_{diss}$	26.4	28.6	2.445	2.209	165.20
$PDD1_{diss}$	−13.0	−11.8	4.888	1.661	145.36

Table 3.6: Energetic barrier (ΔG in kcal/mol) for different transition states with different levels of theory. Single-point energy estimations using 6-311++G($3df, 2p$) basis set from geometries optimised using B3LYP methodology. The uncatalysed transition states were used as a comparative reference.

Method	TS_{diss}^{uncat}	TS_{asso}^{uncat}	TSM1	TSDD1	$TSDD1_{prot}$	$TSDD1_{diss}$
B3LYP/GD3BJ	22.3	35.8	19.2	22.8	21.5	23.4
M06-2X	26.5	34.5	19.0	20.2	19.8	28.8
BP86/GD3BJ	18.3	31.9	17.0	18.8	14.1	20.0

tive transition states in presence of mononuclear and dinuclear molybdenum species. When molybdate species are present, the preferred mechanism is changed from dissociative to associative. Whereas the dissociative mechanism is slightly disfavoured when adding the catalyst, the associative mechanism is considerably stabilised by around 15 kcal/mol. The results with different methodologies uphold and support the obtained results with B3LYP and suggest that the choice of method is adequate for this kind of calculations.

With this information we can conclude that the protonated associative

pathway is energetically favoured over the previous mononuclear pathway. Despite having a higher energetic barrier, this mechanism starts from a considerably more favourable species, resulting in transition states that are lower in energy than in the previous mechanism. In good nucleation conditions—low pH and enough complex concentration—, this process will be preferred over the mononuclear pathway.

Pathways Involving Mono Bridged Dinuclear Species

For the next pathway, we considered a pentacoordinated species analogous to a structure described by Vilà-Nadal *et al.*[205] This RDM2 species can be related to RDD1 by the endergonic release of three hydroxides. Starting from this species, we can see that a water addition to one of the unsaturated molybdenum atoms of the dinuclear species followed by a proton transfer leaves the energetics of the system almost invariant (-0.6 kcal/mol). From the structure RDM4, a hydroxide could coordinate with the other unsaturated molybdenum atom to get a structure where both metal centres are pentacoordinated. This process is endergonic, probably due to both stiff and distorted trigonal bipyramidal coordination of the molybdenum atoms, getting an intermediate 13.0 kcal/mol over the reference state.

In RDM5, the hydroxide is very close to the phosphorous atom, ready for an intramolecular attack. A very rigid phosphorane intermediate (IDM1) is obtained after this attack, 7.5 kcal/mol higher in free energy. Moreover, all the structures in which the attacking hydroxide is shared are very high in energy with respect to the ones in which is single-coordinated.

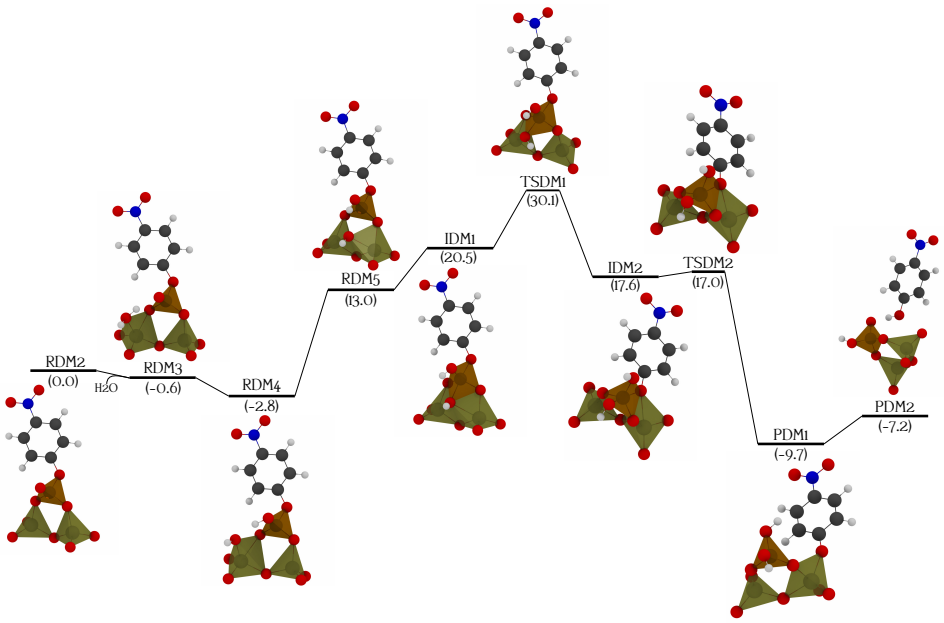

Figure 3.12: Calculated free energy profile for NPP hydrolysis using lower coordination mode dinuclear molybdenum species using B3LYP+ methodology. Relative free energies are in kcal/mol.

A complete reversible process would mean that the molybdenum atoms ease the hydroxy attack as well as the nitrophenolate release. To that, molybdenum atoms should rotate around the shared oxygen atoms to locate near the leaving group. Those rotations are the most demanding processes in this pathway and are not linked with the formation or rupture of the phosphorane structure. Unfortunately, the transition state structures for these torsion processes were difficult to find due to the complexity of the involved movements. We used the Nudged Elastic Band method to overcome these difficulties and estimate the energetics related to this process, resulting in a barrier of approximately 9.6 kcal/mol over the previous intermediate.

This mechanism has to overcome more than 30 kcal/mol of energetic cost

Table 3.7: Relative energies (in kcal/mol), relevant distances (Å) and angles (deg) for the species involved in the monobridge dinuclear mechanism. Single-point energy estimations using 6-311++G(3*df*,2*p*) basis set from geometries optimised at B3LYP-GD3BJ/6-31+G**/PCM level of theory.

Species	ΔH	ΔG	P−O(LG)	P−O(Nu)	O(LG)−P−O(Nu)
RDM2	0.0	0.0	1.625	—	—
RDM3	−10.9	−0.6	1.621	3.123	137.52
RDM4	−12.2	−2.8	1.603	3.183	142.58
RDM5	3.6	13.0	1.596	2.617	176.20
IDM1	10.9	20.5	1.661	1.894	175.43
TSDM1*	31.2	30.1	1.787	1.652	176.76
IDM2	7.1	17.6	1.661	1.894	175.43
TSDM2	5.1	17.0	2.067	1.632	173.20
PDM1	−19.1	−9.7	3.585	1.591	143.10
PDM2	−13.7	−7.2	3.620	1.596	153.62

* Calculated at BP86/TZ2P/COSMO level of theory by using the Nudged Elastic Band method for searching transition states.

from the lowest energetic species, a considerable quantity for the process. If we continue the rotation of the molybdenum atoms, we obtain a similar structure in which one molybdenum atom is coordinated to the leaving group instead of the nucleophile. This intermediate already shows an elongation of the P−OR bond of the leaving group to 1.829 Å, being lower in energy by almost 5 kcal/mol. Geometric and energetic data are displayed in Table 3.7. In these phosphorane species, both nucleophile and leaving group remained at a distance closer than 2 Å, being the angle between them around 173−176 degrees.

Since the the nitrophenolate is a much better leaving group than the hydroxide, the release of this bond can be achieved from that structure with a transition state that is less than 1 kcal/mol higher in energy than the previ-

ous intermediate and lower in energy than the intermediates of the rotation processes of the molybdenum atoms. This gives a very exergonic structure in which the phosphorane structure is broken and the stiffness is relaxed. The release of the leaving group from the coordination sphere of the molybdenum comes along with a proton transfer from the phosphate in an endergonic process (2.5 kcal/mol). After this process, the dinuclear molybdenum species incorporating the phosphate could continue its nucleation process to get the Keggin anion structure.

Nevertheless, this pathway is not preferred over the dinuclear dibridge pathways, in which the direct interaction between molybdenum and the nucleophile or the leaving group is hindered. This interaction seems to be very strong due to the high Lewis acidity of the molybdenum; once an adduct is formed, greater energies are needed to break it, slowing the reaction. If these interactions are impeded due to the saturation of the coordination sphere of the molybdenum, smoother energetic profiles and smaller barriers are obtained.

QTAIM and NCI Topologies

To get insight into the catalytic process of these molybdate species, we have explored the electron density topology for the transition states of the catalysed and uncatalysed reactions.

The properties of the bond critical points (BCPs) of the bonds involved in the transition state (red boxes) are shown in Figure 3.13. The electron density value at the bond critical point (ρ_r) describes the bond strength, representing the electron population between two nuclei.

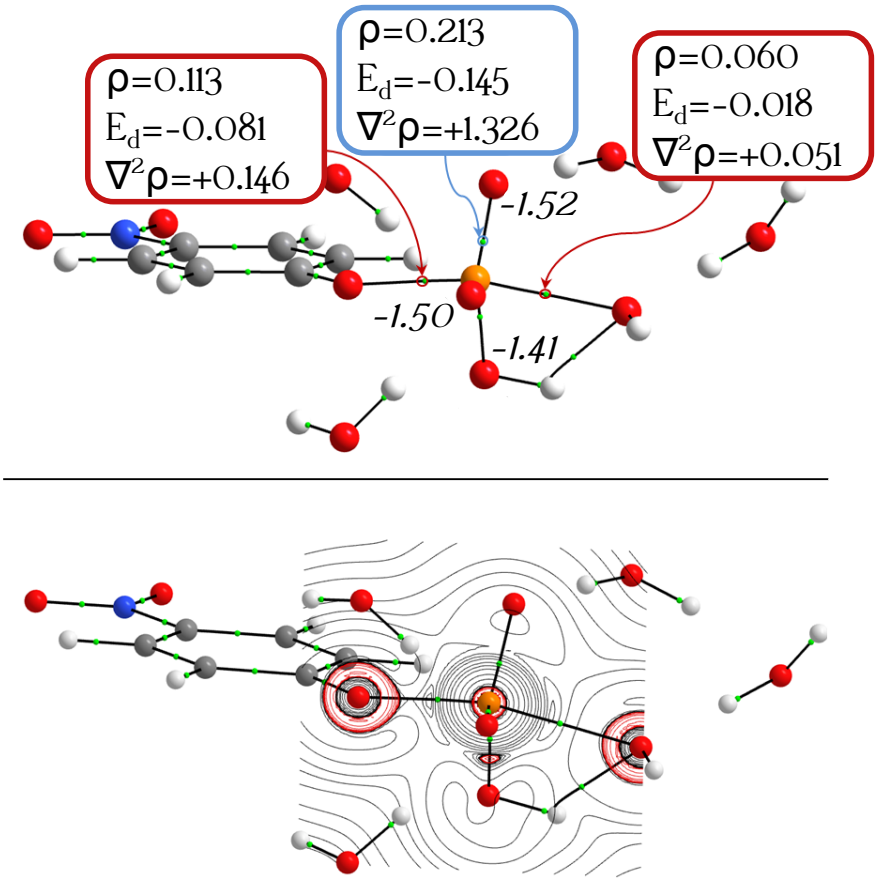

Figure 3.13: Bonding scheme, properties of BCPs involved in the transition state and integrated QTAIM charges for the O of phosphate group (top), and $\nabla^2\rho$ plot (bottom) for the non-catalysed reaction of the hydrolysis of NPP. Black lines represent charge depletion zones whilst red lines represent charge concentration zones.

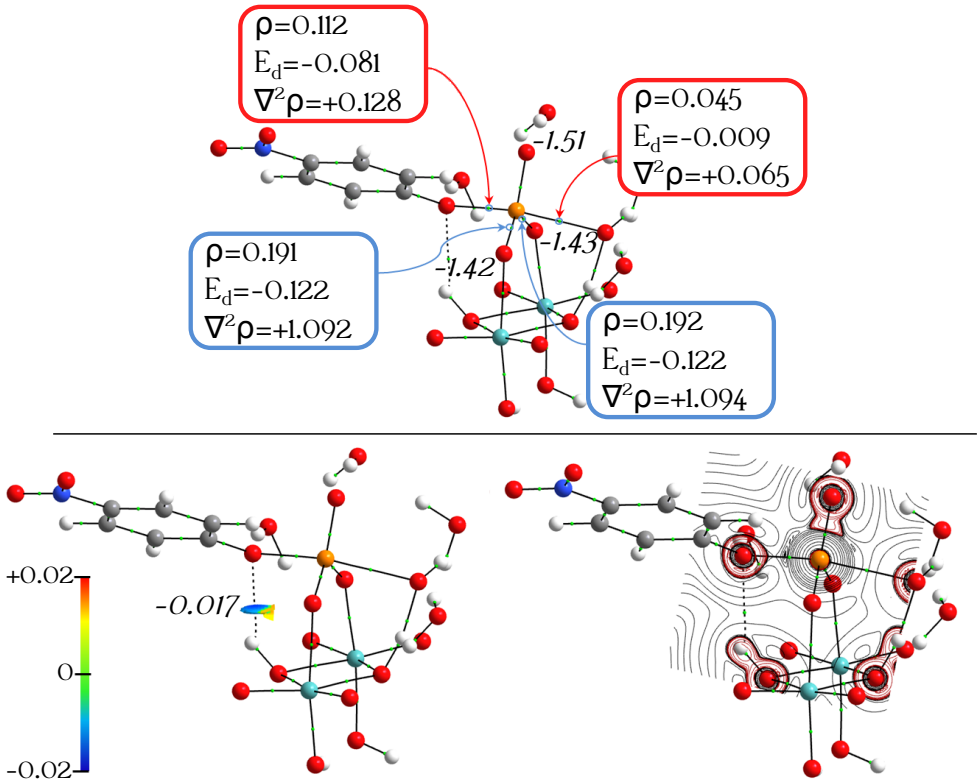

Figure 3.14: Bonding scheme, properties of BCPs involved in the TSDD1 transition state and integrated QTAIM charges for the O of phosphate group (top), $\nabla^2\rho_r$ contour map (bottom right), and NCI analysis (bottom left). Black lines represent charge depletion zones whilst red lines represent charge concentration zones

Furthermore, the electron energy density (E_d) provides information about the stability of the bond. More stabilised covalent interactions present negative values, whilst positive values or close to zero represents unstable or weak interactions. In this figure, the values for the integrated QTAIM charges for the O atoms of the phosphate group are also presented. At the same time, the contour map for the laplacian of the electron density $\nabla^2\rho_r$ is represented in the plane containing the atoms involved in the reaction coordinate.

Figure 3.14 presents the bonding scheme for the TSDD1 transition state structure for the hydrolysis in presence of dinuclear molybdate. It is observed that the electronic structure of the phosphate moiety has changed regarding the non-catalysed case in Figure 3.13. Firstly, the integrated charges of the O atoms are slightly lowered, particularly for the O atoms that are part of the molybdate structure, showing QTAIM charges of -1.42 and -1.43. Furthermore, the characteristics of the BCPs of the bonds between these O atoms and P (blue boxes) have also been modified, presenting lower values, namely, ρ_r=0.191 and 0.192 a.u. Regarding the breaking and emerging bonds, the BCPs present minor variations with a slight decrease of the electron denstity, ρ_r=0.112 and 0.045 a.u. These results suggest that the BCPs of the bonds involved in the reaction coordinate remain almost unchanged. Still, the electronic environment of the O atoms of the phosphate moiety has been quenched.

Furthermore, a weak interaction appears between the H atom connected to the bridge O atom of the molybdate structure with the O atom of the leaving group. Such weak interaction is represented in the corresponding NCI isosurface in Figure 3.14. This stabilising interaction, together with the reduction of the electron density in the phosphate moiety, contributes to the global stabilisation of the whole structure of the transition state. Figure 3.15 presents the same topological analysis for the transition state TSDD1$_{dis}$, leading to very similar results.

Next, we will explore the electron density analysis of the transition state with the protonated dinuclear species. Figure 3.16 plots the topological analysis for the TSDD1$_{prot}$ transition state. Notably, the values of ρ_r and E_d

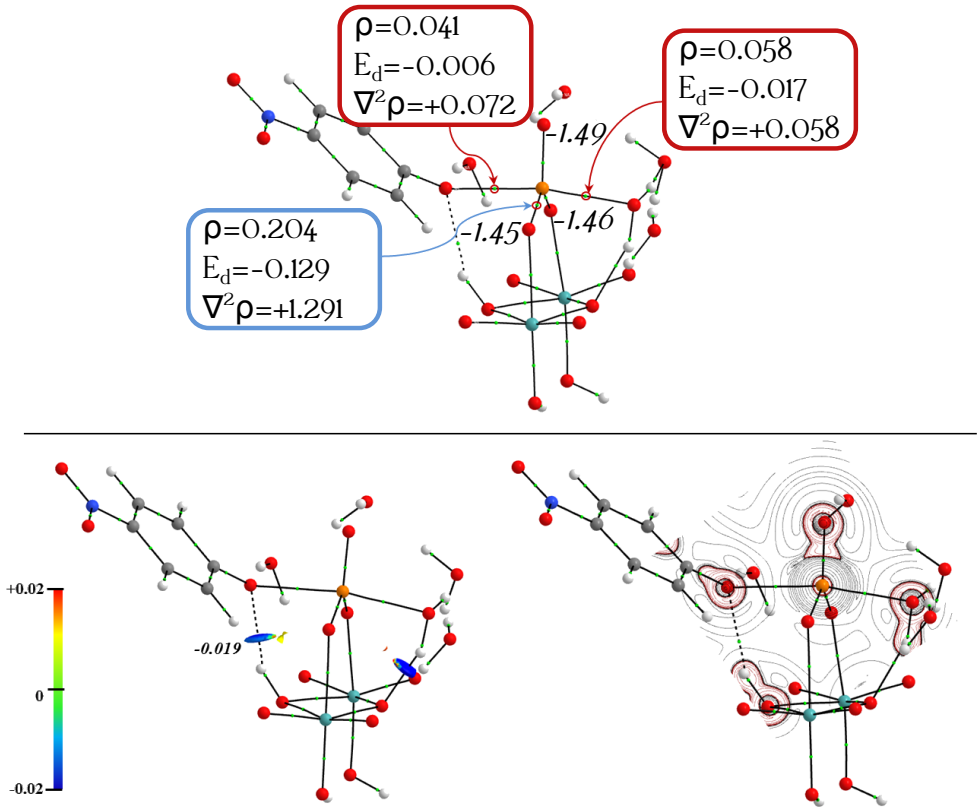

Figure 3.15: Bonding scheme, properties of BCPs involved in the TSDD1$_{dis}$ transition state and integrated QTAIM charges for the O of phosphate group (top), $\nabla^2\rho$ contour map (bottom right), and NCI analysis (bottom left). Black lines represent charge depletion zones whilst red lines represent charge concentration zones.

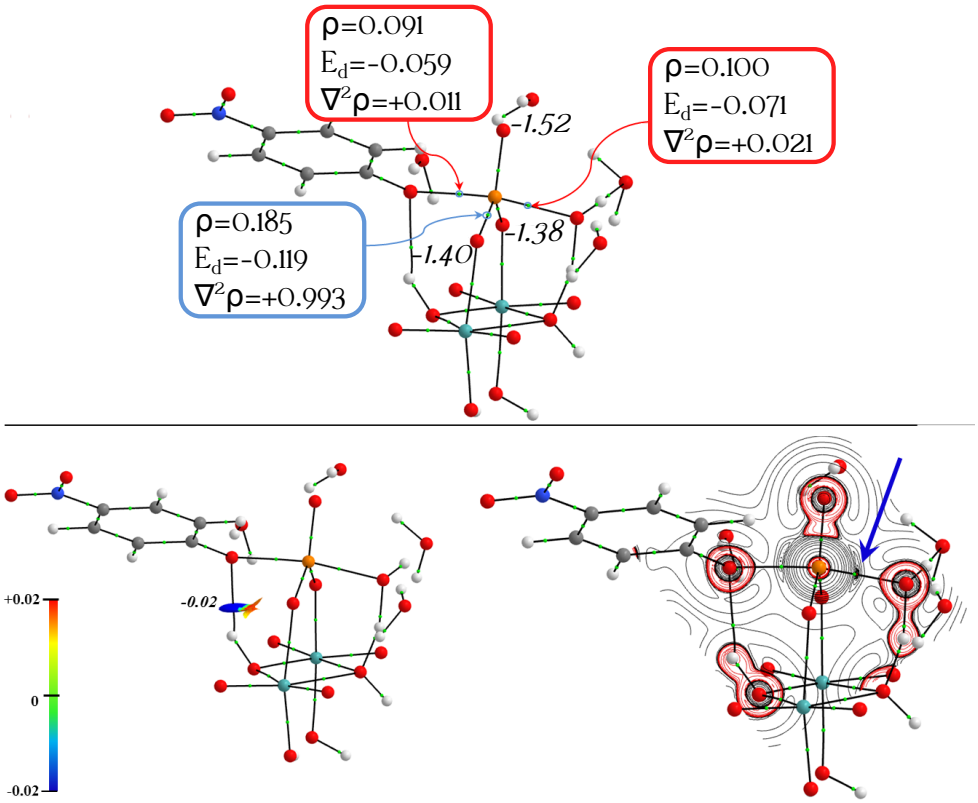

Figure 3.16: Bonding scheme, properties of BCPs involved in the TSDD1$_{prot}$ transition state and integrated QTAIM charges for the O of phosphate group (top), $\nabla^2\rho_r$ contour map (bottom right), and NCI analysis (bottom left). Black lines represent charge depletion zones whilst red lines represent charge concentration zones.

corresponding to the P−O emerging bond with the nucleophile have shifted to values that imply a stronger interaction, with a larger ρ_r of 0.100 a.u., and a more negative E_d, namely, −0.071 a.u. Besides, the QTAIM negative atomic charges of the oxygen atoms of the phosphate group connected to the molybdate structure have been reduced to values of −1.40 and −1.38. At the same time, the NCI analysis shows the same results, where an H atom of the molybdate structure interacts with the leaving oxygen with a weak stabilising

interaction. Additionally, another effect of the protonation of the molybdate environment is observed in the contour map of the Laplacian $\nabla^2\rho$. It is observed that close to the BCP between the P atom and the nucleophilic O atom, an emerging zone of negative $\nabla^2\rho$ appears (highlighted with a blue arrow) and the charge concentration zone surrounding the nucleophilic oxygen protrudes towards the BCP.

These results clearly show that the presence of the molybdate species with a protonated structure quenches the electronic environment of the phosphate, strengthening the P−O forming bond with the nucleophile and in agreement with the observed stabilising effect of the corresponding energy profiles.

Finally, the topological study has also been carried out for the reaction where a mononuclear complex is attached to the phosphate. Figure 3.17 shows the bonding scheme for the transition state TSM1. For this structure it is observed that the BCP properties of the emerging bond have similar values to the results obtained for TSSD1 (and TSSD1$_{dis}$).

In summary, these results suggest that the preferred geometrical arrangement of the transition state corresponds to to the TDD1$_{prot}$ structure. In this species, a weak interaction that stabilises the leaving group in conjunction with the quenching of the electronic environment of phosphate yields the most favoured bonding scheme between the P atom and the nucleophilic oxygen atom.

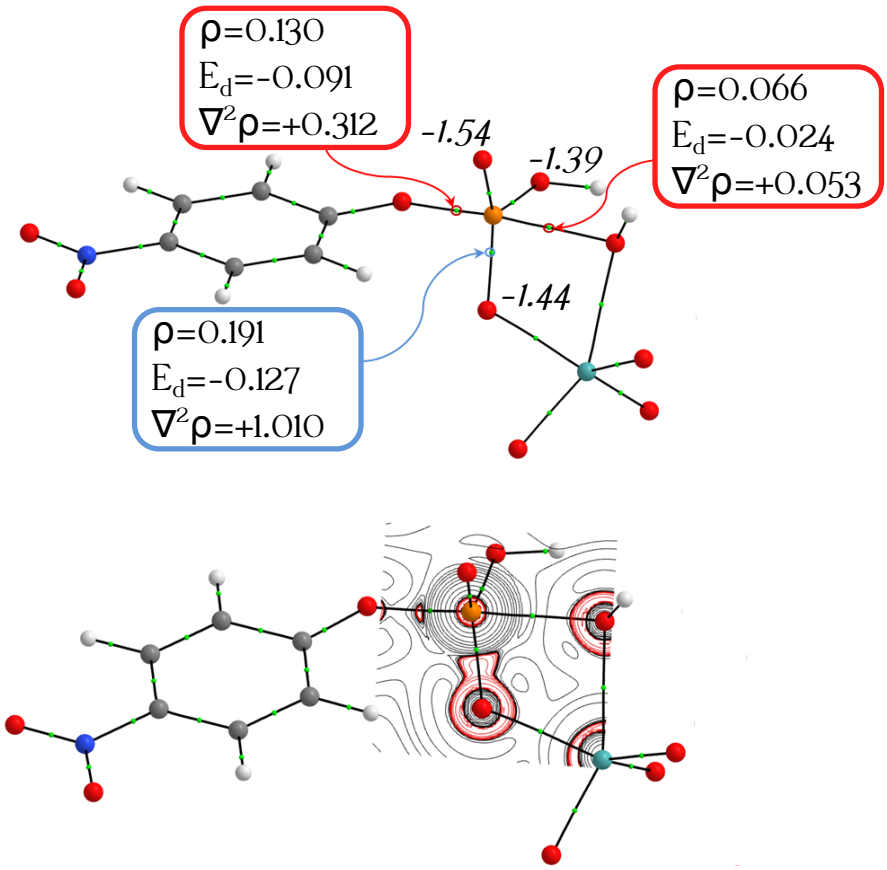

Figure 3.17: Bonding scheme, properties of BCPs involved in the TSM1 transition state and integrated QTAIM charges for the O atom of phosphate group (top), $\nabla^2\rho$ contour map (bottom). Black lines represent charge depletion zones whilst red lines represent charge concentration zones.

3.4 Conclusions

We have explained the relevant chemistry in solution once $MoO_2Cl_2(DMF)_2$ is dissolved: the release of DMF, the hydrolysis of the Mo−Cl bond and the mononuclear species that could be majoritarian at different pH before nucleation. Also, we have proposed the mechanism by which this complex promotes this reaction, suggesting different pathways depending on the possibilities of nucleation. In the experiments with a low quantity of initial complex, the pH lowered to only 6, and the concentration of molybdenum was not enough to form polynuclear species. In that conditions a slower catalysis was obtained, in agreement with the proposed mononuclear pathway. On the contrary, nucleation processes occur if the concentration is higher and a very acidic media is obtained, giving a transient isopolyoxometalate and a Keggin anion at the end. We explored other pathways using dinuclear species which could be formed if these conditions are favourable. After the very exergonic formation of these species, the surpass of the energy barriers of the dinuclear pathways would be straightforward, giving NPP hydrolysis. That would lead ultimately to the formation of the Keggin anion. QTAIM calculations showed a quenching of the electronic environment at the transition state structure, reinforcing the emerging bond. We highlight that the molybdenum species significantly reduce the energetic barrier of associative transition states, changing the overall preference of the phosphate hydrolysis to substrate-assisted mechanisms over solvent-assisted ones.

Chapter 4

PROBING THE CATALYTICALLY ACTIVE SPECIES IN POM-CATALYSED PHOSPHATE ESTER MODEL HYDROLYSIS

Abstract

Phosphoester hydrolysis is an important chemical step in DNA repair. One archetypal molecular model of phosphoesters is para-nitrophenylphosphate (NPP). It has been shown previously that the presence of molecular metal oxide $[Mo_7O_{24}]^{6-}$ may catalyse the hydrolysis of NPP through the partial decomposition of polyoxomolybdate framework resulting in a $[(PO_4)_2Mo_5O_{15}]^{6-}$ product. Real-time monitoring of the catalytic system using electrospray ionisation mass spectrometry (ESI-MS) provided a glance into the species present in the reaction mixture and identification of potential catalytic candidates. Following up on the obtained spectrometric data, Density Functional Theory (DFT) calculations were carried out to characterise the hypothetical intermediate $[Mo_5O_{15}(NPP)_2(H_2O)_6]^{6-}$ that would be required to form under the hypothesised transformation. Surprisingly, our results point to the dimeric

$[Mo_2O_8]^{4-}$ anion resulting from the decomposition of the $[Mo_7O_{24}]^{6-}$ as the active catalytic species involved in the hydrolysis of the NPP rather than the originally assumed $\{Mo_5O_{15}\}$ species. A similar study was carried out involving the same species but substituting Mo by W. The mechanism involving W species showed a higher barrier and less stable products in agreement with the non-catalytic effect found in experimental results.

4.1 Introduction

Polyoxometalates (POMs) are negatively charged metal oxide clusters known since 1826 (see Figure 4.1).[206] Classical POM archetypes are mainly formed from d^0 metal oxides made of V, Mo, or W, which can undergo condensation reactions at acidic pH with subsequent loss of H_2O.[207] Nevertheless, more recently, we can find examples of similar polyanionic nanostructures containing elements for the f,[208–211] and p groups.[212, 213]

During the last years, the applications of this family of compounds have been explored intensively and found their way in various fields such as the decontamination of water,[214] flash memory devices,[215] qubits,[216] water splitting,[217] as well as in biomedical research exploring their function as antiviral or antitumoural drugs.[218–220] However, biomedical studies were still scarce in the latter case in the 90s as discussed in the review of Rhule

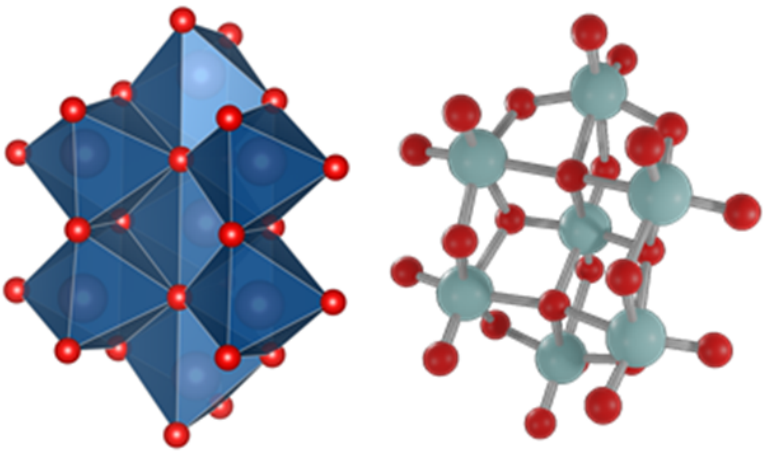

Figure 4.1: Polyhedral (left) and ball & stick (right) representations of the $[Mo_7O_{24}]^{6-}$ system studied in this work.

et al.[218] It was during the early-mid 2000s when systematic studies on the application of POMs to cancer treatment increased exponentially.[8, 219, 221–224] Additionally, recent advances in the use of POMs for medical applications, their antitumour activity[40] and their potential use to fight against bacterial antibiotic resistance[225, 226] have been reviewed by Bijelic *et al.*[40, 225] and Kortz *et al.*[226]

According to Bijelic *et al.*[40, 225] the proposed modes of antitumoural action of POMs involves a high number of biological targets: 1) Activation of cell death pathways, 2) Inhibition of angiogenesis, 3) Interaction with proteins or 4) DNA interaction among other mechanisms. On the other hand, the proposed mechanisms of action against bacteria involve: a) inhibition of both PBP2a and β-lactamases by POMs, b) POMs target P-type ATPases, c) impairment of the bacterial electron-transport chain (respiratory system) by POMs, d) POM-mediated increase of the reactive oxygen species level via oxidation, e) interaction of POMs with important membrane-anchored proteins and enzymes, f) the disruption of the bacterial cytoskeleton dynamics by POM-interactions with cytoskeletal elements, g) disruption of the bacterial cell wall leading to leakage of intracellular substances or h) interaction with cytoplasmic elements or proteins that are anion-sensitive like nucleic acid-binding proteins. As discussed earlier, one of the processes described in the reviews of Bijelic *et al.*[40, 225] is the interaction of POMs with DNA to promote its phosphoester hydrolysis as artificial phosphoesterases. The focus of this work is the investigation of the above catalysed hydrolysis step.

The phosphoester bond is produced when any hydroxy group of the phos-

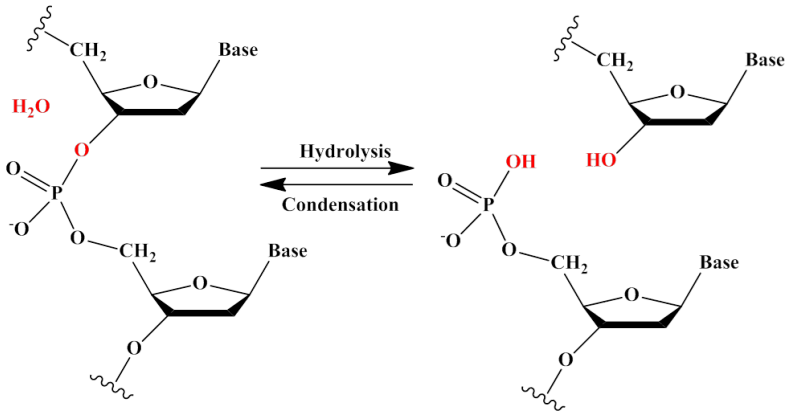

Figure 4.2: Phosphodiester hydrolysis in DNA.

phoric acid react with hydroxy groups of neighbouring molecules to form an ester bond. In the case of DNA, two bonds are formed from two hydroxy groups of the phosphoric acid with the deoxyribose sugars forming the DNA strand to form the phosphodiester bond (see Figure 4.2). These types of bonds are extremely stable and therefore play a very important role to maintain the integrity of the genetic code and the proper function of proteins. Consequently, nature has devised these links to maintain the connectivity of nucleosides in DNA, with remarkable kinetic stability: the half-life for hydrolysis of phosphoester bonds in DNA at neutral pH and 298 K is estimated to be 130 000 years.[227] This resistance to hydrolysis is mainly due to the repulsion between the negatively charged backbone and the potential nucleophiles which are also negatively charged. Consequently, an important Coulombic repulsion has to be overcome in order to produce the reaction, leading to high activation energy for the phosphoester hydrolysis.[15]

This stability of the phosphoester bond can be overcome through a family

of enzymes known as phosphoesterases. These catalysts play an essential role in repairing DNA sequences[228], increasing the phosphoester bond hydrolysis rate. Thus, the development of artificial catalysts promoting phosphoester bond hydrolysis in reasonable time scales is an important research topic that has been explored extensively during the last 15 years.[9–15, 229–249] These artificial catalysts include Cu(II),[250] Zn(II),[251] La(III),[252–254] Mo(V/VI) complexes[13–15] and/or POM clusters.[9–12, 229, 230, 235–237, 239, 241, 243]

Particularly surprising is the catalysis of the phosphoester bond by polyoxoanions since an also negatively charged phosphate group will need to coordinate with them to facilitate a nucleophilic attack by water. A deeper understanding and rationalisation of the catalytic mechanism involving POMs and chemical species with phosphoester bonds is inherently challenging. In previous studies, Luong *et al.*[237, 239] attempted to tap into the mechanistic action of $[Mo_7O_{24}]^{6-}$ ($\{Mo_7\}$) in phosphoester hydrolysis employing model substrates and using several experimental techniques.

Their work consisted of the hydrolysis of para-nitrophenylphosphate (NPP) in the presence of a $\{Mo_7\}$ solution.[9, 11, 12, 229] The NPP molecule is a typical model substrate of the phosphoester bond for biological phosphate esters. In their account, Cartuyvels *et al.*[11] clearly found that the hydrolysis was activated in the presence of $\{Mo_7\}$ and subsequently proposed a set of transformation steps based on their findings, notably ^{31}P and ^{1}H and DOSY NMR, UV-Vis and RAMAN spectroscopies. It was found that during the course of this reaction a side product $[Mo_5O_{15}(PO_4)_2]^{6-}$ ($\{Mo_5-PO_4\}$) anion was formed (see Figure 4.3) previously identified by Fischer and others.[255]

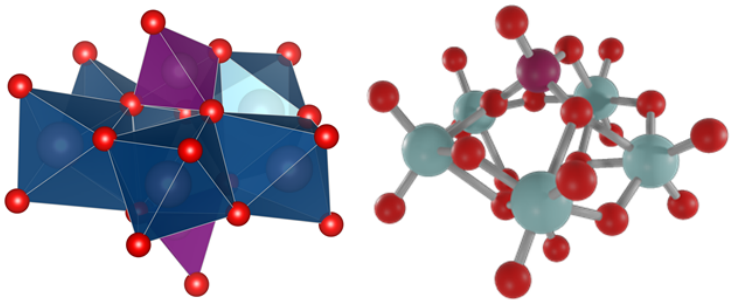

Figure 4.3: Polyhedral (left) and ball & stick (right) representations of the $[Mo_5O_{15}(PO_4)_2]^{6-}$ anion.

Based on this evidence the authors proposed two transformative steps (Figure 4.4) conducive to hypothetical intermediate species $[(NPP)_2Mo_5O_{21}]^{4-}$ ($\{Mo_5-NPP\}$) and $[(NPP)_2Mo_{12}O_{36}(H_2O)_6]^{4-}$ (Intermediates A and B in the original paper).

One aspect is particularly striking in the previously reported work: The disparity in geometries between the $\{Mo_5-PO_4\}$ product and the $\{Mo_7\}$ starting material. There is no simple obvious route from the latter to the former other than *i)* the complete disassembly and subsequent re-assembly into $\{Mo_5-PO_4\}$, or *ii)* a significant structural rearrangement within the $\{Mo_5\}$ framework. The primal goal in this work is to unveil some of these obscure aspects in this particular reaction step. As such, it was decided to revisit this work combining computational approaches (DFT) with experimental data from our colaborators (ESI-MS) to converge both approaches.

Herein we start out by analysing the information given by the ESI-MS experiments about the $\{Mo_7\}$ + NPP reaction mixture, which can provide us with other potential intermediate candidates that could be responsible of the observed catalysed hydrolysis. Then, we can use these species as a starting

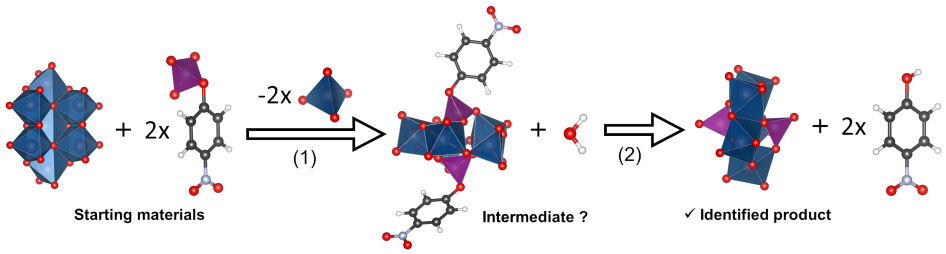

(1)+(2): $[Mo_7O_{24}]^{6-} + 2[NO_2PhOPO_3]^{2-} + H_2O \rightarrow [(PO_4)_2Mo_5O_{15}]^{6-} + 2(NO_2PhOH) + 2[MoO_4]^{2-}$

Figure 4.4: Proposed chemical reactions of the hydrolysis of NPP catalysed by heptamolybdate. Purple-hatched polyhedra represent the phosphate groups.[229]

point to carry out a reaction path analysis *in silico* of the hydrolysis process. Our new results highlight the fact that the Mo_5O_{15} ($\{Mo_5\}$, species which is the predecessor of the identified $\{Mo_5-PO_4\}$) is unlikely to be the catalytically active species. We propose an alternative sequence of transformations where the original $\{Mo_7\}$ reactant dissociates into two moieties: one dinuclear $[Mo_2O_8H_4]$ ($\{Mo_2\}$), and a pentanuclear $\{Mo_5\}$ species. The former species is the agent that catalyses the hydrolysis whereas the latter will capture the resulting phosphate. Additionally, the generation of the $Mo_2O_8H_4$ and Mo_5O_{15} species was corroborated by mass spectrometry experiments. Finally, the effect of solvent was considered not only with the dielectric continuum approach but also with a minimal number of explicit H_2O molecules which provide a more accurate portrayal of the energy barrier corresponding to the pentacoordinate transition state.

4.2 Computational Details

DFT calculations were performed using the Amsterdam Density Functional 2017.01 (ADF) program package.[187] Geometry optimisations, without symmetry constraints, were performed resorting to a combination of the gradient corrections of Becke 1988 exchange functional and Perdew 1986 correlation functional as well as the latest version of Grimme dispersion correction (BP86-D3).[85, 98, 189] Relativistic effects were treated with the Zero Order Regular Approximation (ZORA) Hamiltonian.[190, 191] The frozen core approximation was employed, thus, triple-ζ Slater-type orbitals (STO) were used to describe the valence shells of C and N (2s and 2p). One polarisation function was added to C, N, O, Mo and W (single-ζ, 3d, 4f). Triple-ζ STOs were used to describe the valence shells of H (1s) augmented with one polarisation function (single-ζ, 2s, 2p). Solvent effects were treated with the Conductor-like Screening Model (COSMO) of solvation (Water, $\epsilon = 78.39$).[125–127] Analytical frequencies were calculated to characterise the obtained stationary points and to calculate the free energies (standard state T = 298.15 K, P = 1 atm). Transition states were followed after a fractional displacement of the imaginary vibrational mode to both the reactants and products. The starting structures were modelled after the reported $[Mo_7O_{24}]^{6-}$ and $[Mo_5O_{15}(NPP)_2]^{4-}$ geometries. Molecular renderings were made with VESTA[256] and Chemcraft.[257].

4.3 Results and Discussion

To characterise further the clusters in solution and to identify unambiguously the structural integrity and composition of the species formed during the re-

action, our experimental collaborators employed high-resolution electrospray ionisation mass spectrometry (ESI-MS) and monitored in real time the reaction mixture.[258] We can extract valuable information from those experiments—thoroughly detailed and discussed in Appendix A.

The ESI-MS experiment with the reaction mixture (Figure 4.5) showed a decrease of the $\{Mo_7\}$ species until it can not be detected at 30 h. In this time, NPP values fluctuated due to adducts formation and decomposition. The molybdenum species formed by the $\{Mo_7\}$ decomposition had a nuclearity that ranged from 2 to 6. Interestingly, no NPP adduct was found with heptamolybdate or pentamolybdate species. On the contrary, two dimeric molybdenum species were found to form adducts with NPP. The $\{Mo_5-PO_4\}$ species was confirmed, but its formation was probably due to the free phosphate present in the medium. After 30 h, only dimeric and trimeric species were found, highlighting the decrease in nuclearity over time in presence of NPP. Quite the opposite occurs in an additional experiment without NPP (Figure 4.6, which showed little fragmentation—$\{Mo_7\}$ species having the main peak.

The ESI-MS studies provided the initial evidence of potential molecular candidates that were identified in the catalysed reaction mixture. Because a direct adduct of NPP with $[Mo_7O_{24}]^{6-}$ is unlikely to take place, we proceeded initially to quantify the non-catalysed hydrolysis step in a computational study and used it as a reference point for the catalytic steps.

Two types of mechanisms are traditionally proposed for the non-catalysed reaction. That is, *i)* the substrate-assisted mechanism in which the phosphate acts as a proton acceptor of an incoming water molecule, and *ii)* the solvent-

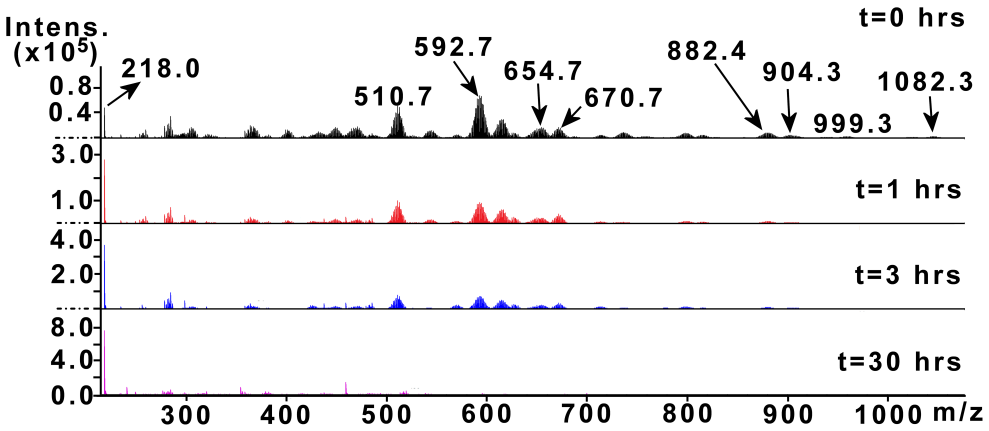

Figure 4.5: Negative mode electrospray ionisation mass spectrum (ESI-MS) of the catalytic reaction mixture in H2O/CH3OH (20:80).

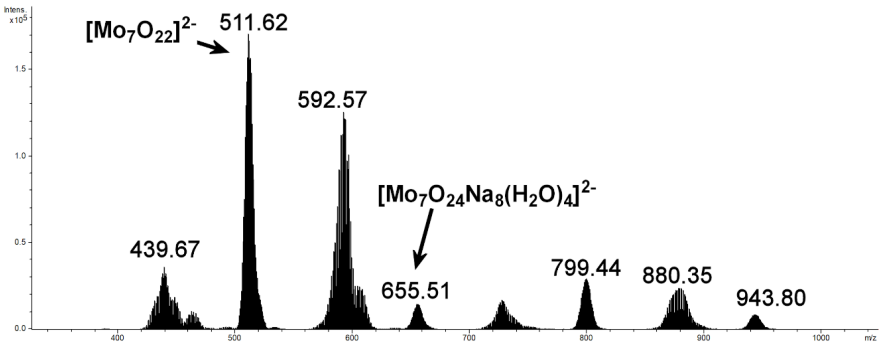

Figure 4.6: Negative ion mass spectrum in H_2O/MeOH (20:80) solution of $Na_6Mo_7O_{24}$.

assisted mechanism in which the nucleophilic substitution of nitro-phenolate proceed before the water molecule loses its proton.

In prior studies,[180] the most appropriate description of these two mechanisms implied the use of explicit water molecules. For this reason, it was decided to include four in all the models as the best compromise between expediency and accuracy. The energy profiles of these mechanisms with the inactivated NPP molecule are depicted in Figure 4.7. The values of $\Delta G^{\ddagger}$

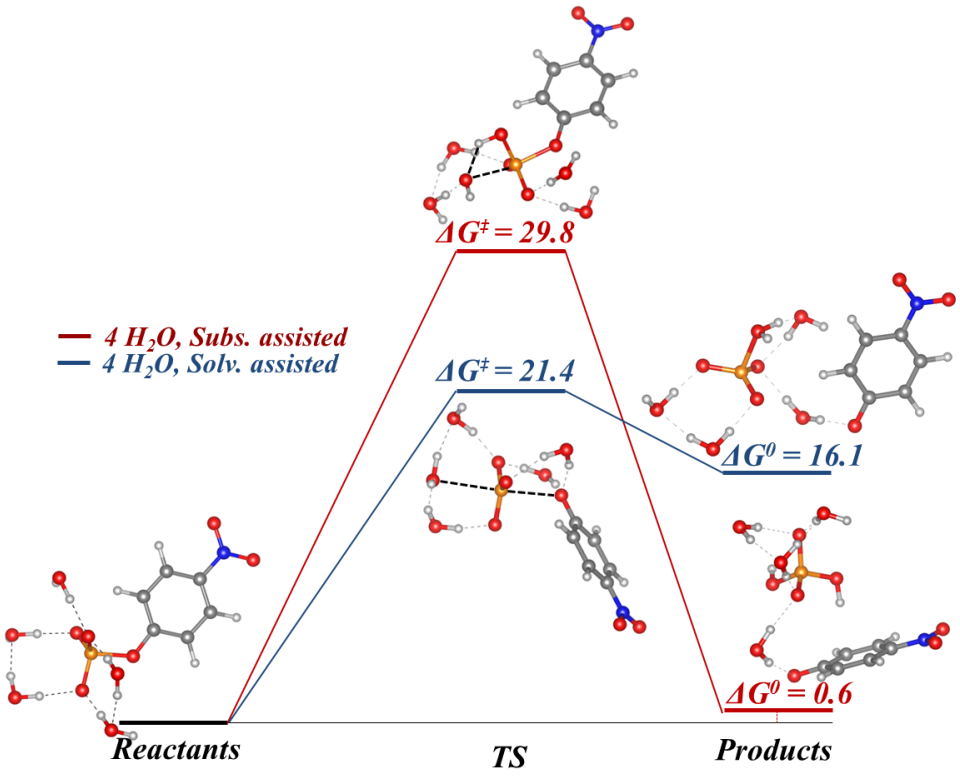

Figure 4.7: Reaction schemes for NPP hydrolysis with no catalyst. Gibbs free energies in kcal/mol.

= 29.8 kcal/mol for the substrate-assisted and $\Delta G^{\ddagger}$ = 21.4 kcal/mol for the solvent-assisted pathways are in line with previous computational studies.[180]

As the product detected in the Parac-Vogt studies[229] is $[Mo_5P_2O_{23}]^{6-}$ the natural step would be to reconstruct this reaction by hydrolysis of grafted NPP to reach this product. A reasonable starting species for this would be $[Mo_5O_{15}(NPP)_2]_4^-$. The production of the pentacoordinate phosphorus intermediate (see Figure 4.8) has an activation barrier that is 11 kcal/mol higher than the activation barrier of the uncatalysed substrate-assisted reaction and

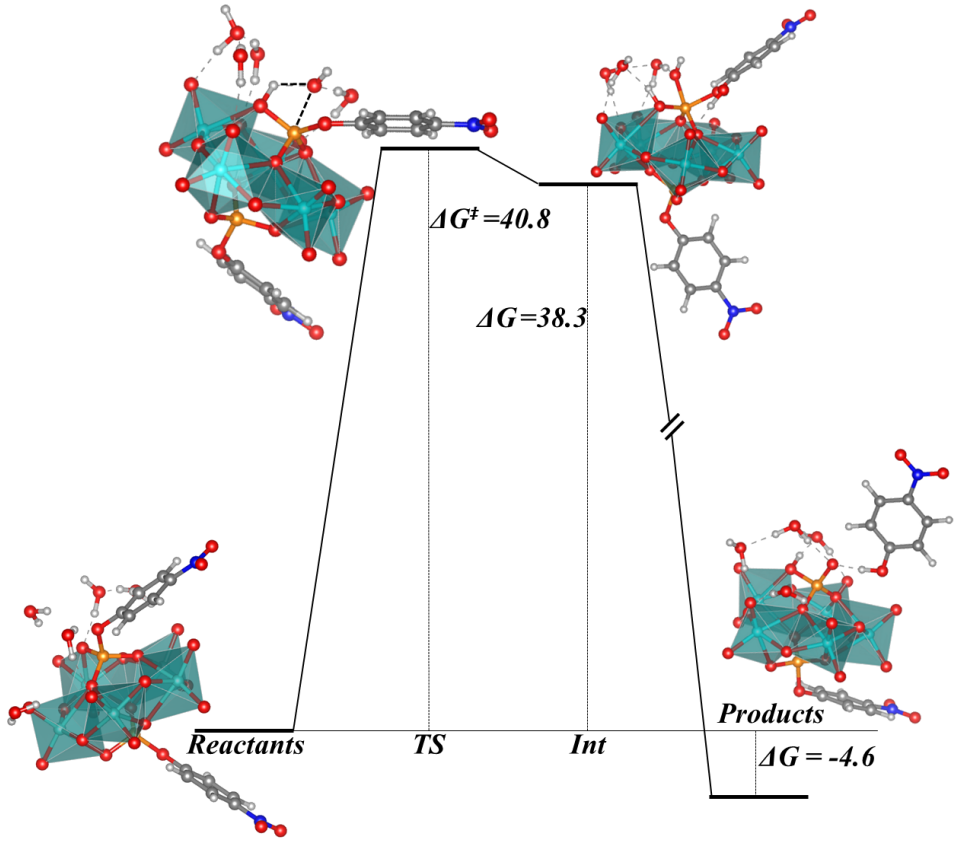

Figure 4.8: Reaction scheme for NPP hydrolysis with $[Mo_5O_{15}(NPP)_2(H_2O)_6]_6^-$. Gibbs free energies in kcal/mol.

19 kcal/mol higher than the barrier for the solvent-assisted pathway.

The POM-activated pathways involve an O−H bond cleavage from an incoming water molecule to one oxygen of the POM structure, resulting in a substrate-assisted type mechanism. For the $[Mo_5O_{15}(NPP)_2]_4^-$ the transition state leads to an intermediate λ^5-phosphate(V) containing structure that is a confirmed local minimum in energy.

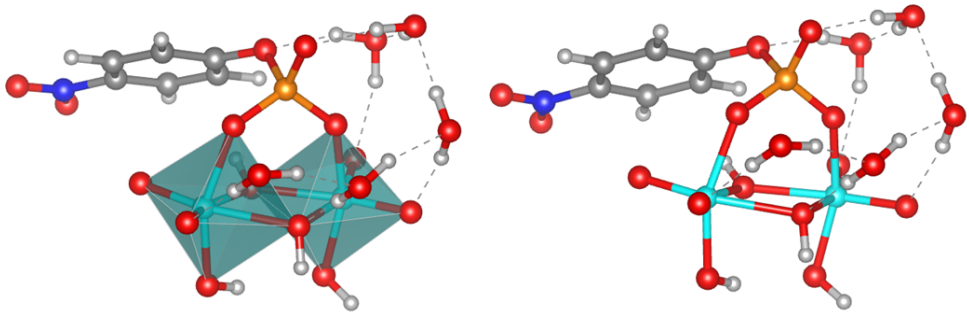

Figure 4.9: Optimised structure for the dimeric species observed through MS experiments along with some solvent molecules.

Subsequent searches for a solvent-assisted mechanism with this $\{Mo_5\}$ activator proved unsuccessful. This is probably due to the latent Brønsted acidity in polyoxoanions, making proton transfers ubiquitous. These results are inconsistent with the proposal set out in a previous work [229] (Figure 4.4), that is, that an $\{Mo_5\}$ species is directly responsible for the higher rate of hydrolysis. The only adduct with NPP that is observed in the ESI-MS study given above is with a dinuclear entity ($[Mo_2O_8(NO_2C_6H_4PO_4)Na_5(H_2O)H]^-$). In the light of this observation, it was decided to explore the catalytic ability of a dinuclear model with a reasonable formulation such as $[Mo_2O_4(OH)_4(NPP)]^{2-}$ ($\{Mo_2\}$), that is, two edge-sharing octahedra capped with hydroxy groups, herein represented in Figure 4.9. Four explicit water molecules were included in this model to make it comparable to the non-catalysed reaction (Figure 4.7). The effect of the surrounding water molecules is analysed in Figure 4.10.

A previous survey was carried out to find the most stable isomer with the formulation $[Mo_2O_4(OH)_4(NPP)]^{2-}$. The results concluded that the species bearing two protonated bridging O atoms and two axial O atoms is the most

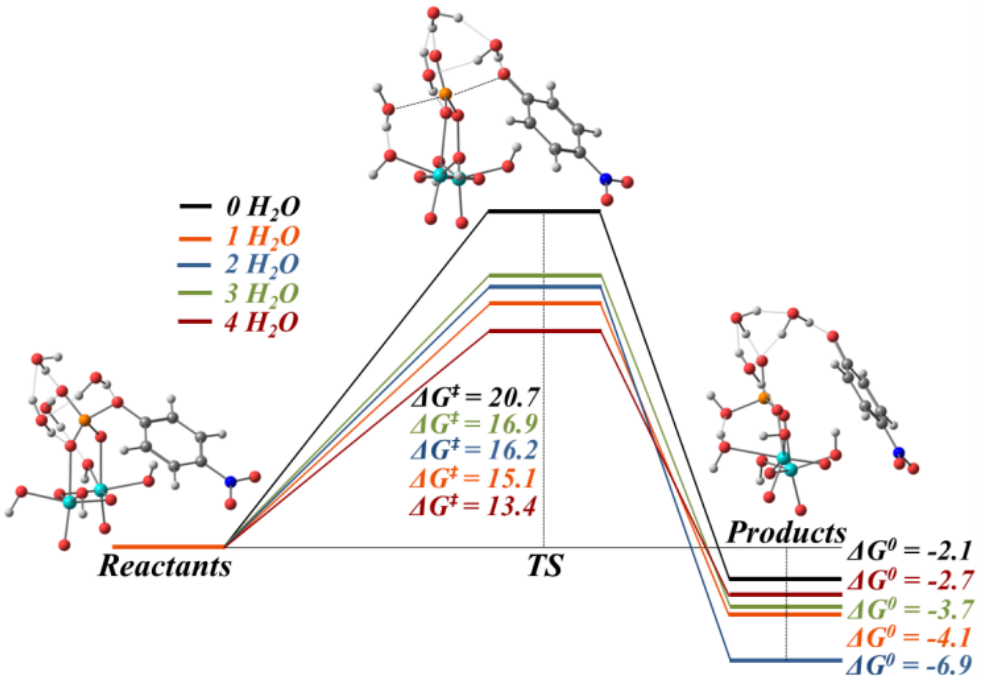

Figure 4.10: Reaction scheme for NPP hydrolysis with $[Mo_2O_8H_4]$ and increasing number of explicit water molecules. Gibbs energies in kcal/mol.

stable one. Such isomer is up to 10.6 kcal/mol more stable in energy than the $[Mo_2O_4(OH)_4(NPP)]^{2-}$ dimeric species capped with equatorial hydroxy groups as observed in Figure Figure 4.11.

The results of the hydrolysed activation with $\{Mo_2\}$ are presented in Figure 4.12 along with the activation barrier. When comparing these values to the non-catalysed pathways shown in Figure 4.7 a more favourable kinetics scenario is observed. The decrease in the barrier height is now down to 8.8 kcal/mol, 21 kcal/mol below the threshold of the substrate-assisted pathway and 13 kcal/mol below that of the solvent-assisted mechanism. This stabilisation of the transition state could be explained because of the stabilising

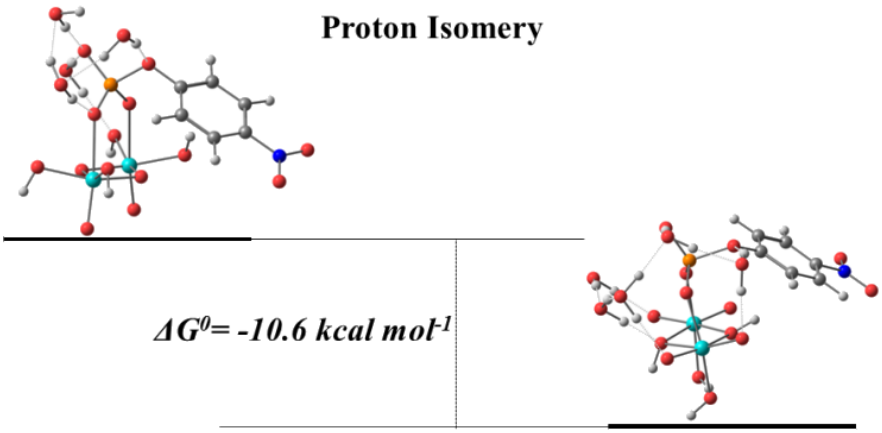

Figure 4.11: Energy difference between the $[Mo_2O_4(OH)_4(NPP)]^{2-}$ dimeric species capped with equatorial hydroxy groups and the most stable $[Mo_2O_4(OH)_4(NPP)]^{2-}$ isomer in which the O bridge atoms are protonated along with the axial O atoms.

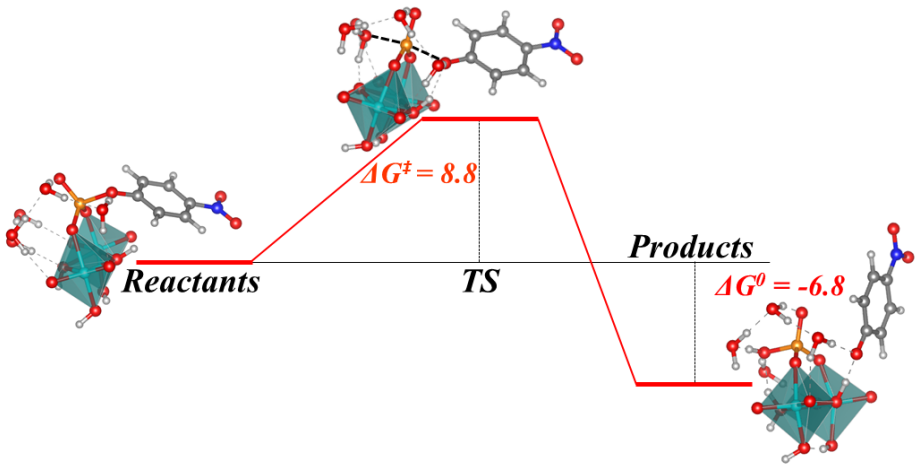

Figure 4.12: Reaction scheme for NPP hydrolysis activated by the $Mo_2O_8H_4$ species in which the O bridge atoms are protonated along with the axial O atoms. Four explicit water molecules are considered. Gibbs free energies are in kcal/mol.

hydrogen bond interactions between the H atoms of the O bridge and the O atom in para to the $-NO_2$ in the NPP species. Moreover, the product free energies are negative (exergonic), whereas those in Figure 4.7 are positive (endergonic, solvent-assisted mechanism) or thermoneutral (the substrate-assisted mechanism). Thus, we can affirm that the isomer of $\{Mo_2\}$ dimer in which the O atoms of the bridge are protonated along with the axial O atoms produces a real catalytic effect on the hydrolysis of the phosphoester bond.

The free energy changes of the overall transformations are summarised below:

- $8\,H_3O^+ + [Mo_7O_{24}]^{6-} \longrightarrow 2\,Mo_2O_8H_4 + [Mo_3O_8]^{2+} + 8\,H_2O$
  ΔG^o = -81.3 kcal/mol
- $2\,[Mo_2O_8H_4] + [Mo_3O_8]^{2+} + 8\,H_2O \longrightarrow Mo_2O_8H_4 + Mo_5O_{15} + 7\,H_2O + 2\,H_3O^+$
  ΔG^o = -79.3 kcal/mol
- $8\,H_3O^+ + [Mo_7O_{24}]^{6-} \longrightarrow Mo_2O_8H_4 + Mo_5O_{15} + 7\,H_2O + 2\,H_3O^+$
  ΔG^o = -160.6 kcal/mol

Probing for Activity in Analogous Wolfram Species

The same calculations were repeated for wolfram analogues. Likewise, the pentanuclear mechanism was also studied (Figure 4.13). The energetic results are compiled and compared to the Mo analogues in Table 4.1. The results showed in general higher activation barriers for the same reactions with wolfram analogues. The effect of the addition of explicit water molecules in the

Table 4.1: Activation and equilibrium free energies ($\Delta G^{\ddagger}$ and ΔG^{o}, in kcal/mol) of NPP hydrolysis.

	$\Delta G^{\ddagger}$	ΔG^{o}
No catalyst substrate-assisted	29.8	0.6
No catalyst solvent-assisted	21.4	16.1

Species	M = Mo	M = W	M = Mo	M = W
$\{M_5\}$	44.1	44.6	-3.6	-2.0
$\{M_2\}$*	8.8	14.6	-6.8	-1.1

* including 4 explicit H_2O molecules.

calculation was studied for the wolfram dimer as well. Comparative results can be found in Figure 4.14.

These results are in agreement with previous studies using Mo species in which the inclusion of explicit solvent molecules had a relevant effect in reaction barriers of phosphoester hydrolysis. We observe a general decrease in $\Delta G^{\ddagger}$ with the inclusion of additional explicit molecules for both metal dimers. The data are also in agreement with the observations by the Parac-Vogt group that found no catalytic activity for the wolfram analogue $[W_7O_{24}]_6^-$, as the activation barriers are higher for $\{W_2\}$ species than for Mo analogues and the general thermodynamic equilibrium is less favourable (Figure 4.15).

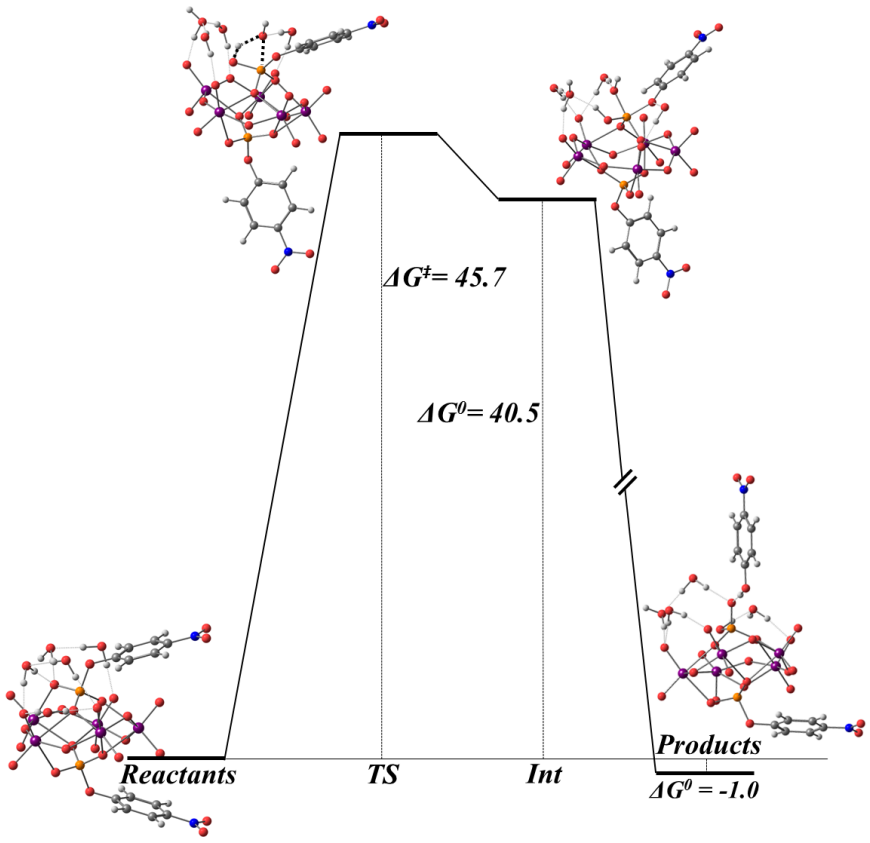

Figure 4.13: Reaction scheme for $[W_5O_{15}(NPP)_2(H_2O)_6]^{6-}$. Gibbs energies in kcal/mol.

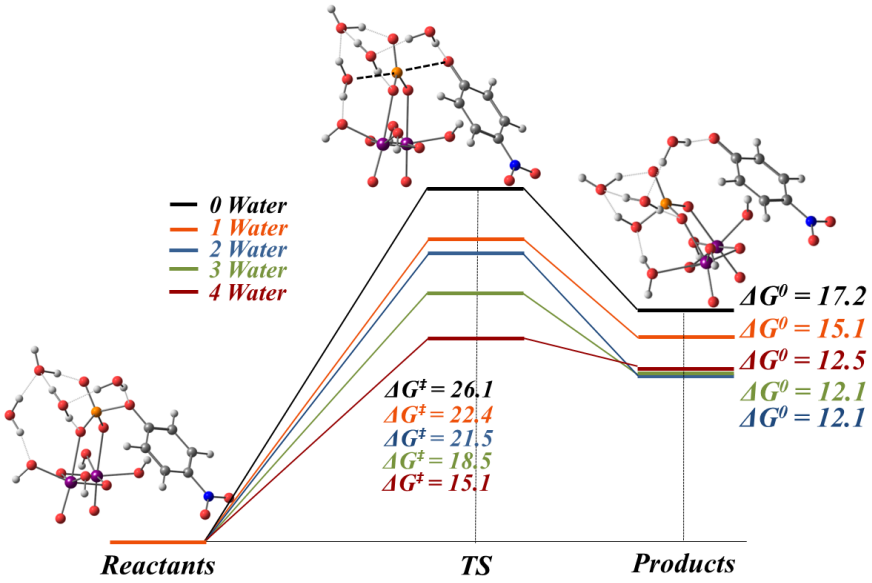

Figure 4.14: Reaction scheme for NPP hydrolysis with $[W_2O_8H_4]$ and increasing number of explicit water molecules. Hydrogen atoms are bonded to equatorial oxygen atoms of the polyoxowolframate. Gibbs energies in kcal/mol.

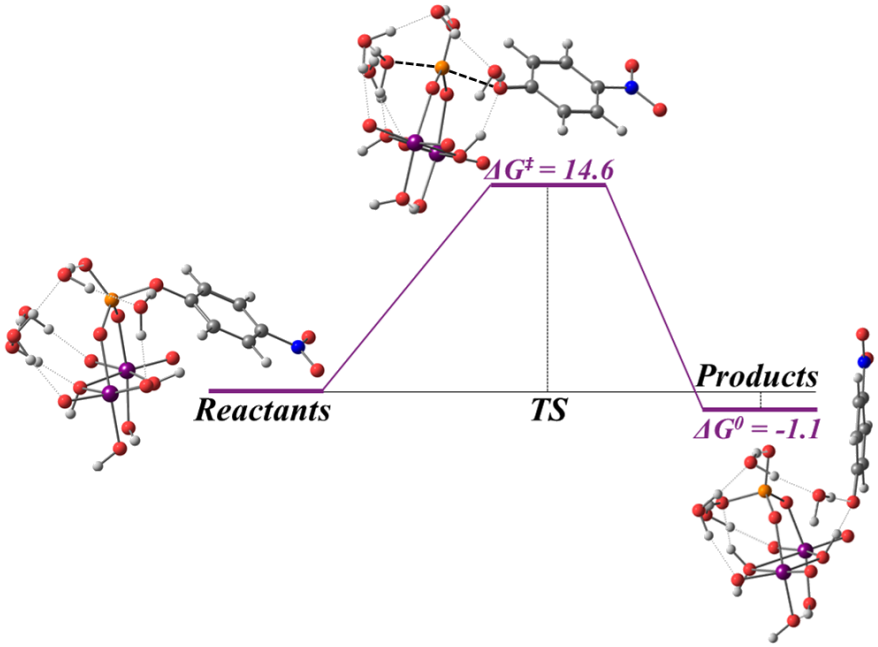

Figure 4.15: Reaction scheme for NPP hydrolysis with $[W_2O_8H_4]$ isomer with 4 explicit water molecules. Hydrogen atoms are bonded to axial and bridging atoms of the polyoxowolframete. Gibbs energies in kcal/mol.

4.4 Conclusions

A theory-experiment combined approach was employed in order to elucidate the underlying hydrolysis mechanism of POM-catalysed phosphate ester model NPP. The original work by Absilis *et al.*[10] proposed the activation of the phosphate group by a pentanuclear $\{Mo_5-NPP\}$ precursor. We have shown that this is inconsistent with the results reported in this work. The catalytically active species responsible for the hydrolytic process is most likely to be the dimeric unit $[Mo_2O_4(OH)_4(NPP)]^{2-}$, which exhibits a lower reaction barrier (8.8 kcal/mol) in a more exergonic reaction (-6.8 kcal/mol) than the uncatalysed one. This is in marked contrast to the $\{Mo_5\}$ alternative which was shown to have unfavourable free energies. Furthermore, no actual adducts between $\{Mo_5\}$ and NPP were detected in the ESI-MS spectra. In combination with the obtained computational data, it is likely that the formation equilibrium of $\{Mo_7\}$ with smaller fragments such as $\{Mo_3\}$ and $\{Mo_2\}$ and their subsequent reassembly is the source of the hydrolytic activation rather than a rearrangement of the Mo_5 framework. The identification of the actual catalytic species leads to a more efficient procedure. The lower mass of the catalytic species can be produced by cheaper starting materials than the originally proposed one which minimises the actual cost of the catalytic reaction and the amount of produced waste, rending it in a greener approach.

Finally, we also studied the analogous pathway for the $\{W_5\}$ and $\{W_2\}$ species and we found that the activation energies for the hydrolytic process are higher than the ones observed for the Mo relatives. The experiments described previously[11] also did not detect any catalytic activity in the presence of the

wolfram species.

Chapter 5

PHOSPHATE DIESTER HYDROLYSIS BY POLYOXOMETALATES

Abstract

Between the diverse applications of polyoxometalates, the anticancer activity of POMs stands out as it can be comparable to available drugs. The mechanism by which polyoxomolybdates inhibit tumour growth has been related to its interaction with key biological phosphate esters. Experimental studies showed that heptamolybdate catalysed the hydrolysis of phosphate diester models BNPP and HPNP through an unknown mechanism which kept the heptamolybdate structure through the reaction. In this computational work, we propose a consistent reaction mechanism that explains the phosphodiesterase behaviour of heptamolybdate compared to the non-catalysed reaction. In addition, a topological analysis of the most important structures shows that the phosphate increases its electrophilicity due to the interaction with the polyoxometalate structure. This mechanism is also coherent with the lack of activity of the more rigid wolfram analogue, also studied in this work.

5.1 Introduction

Polyoxometalates (POMs) are oxide clusters formed by early transition metals like V, Nb, Ta, Mo and W in their highest oxidation state. These species are assembled by condensation from oxometalate species in acidic solutions. They constitute an extensive and broad family with different chemical and physical properties derived from their different structures and compositions.[259] Due to their diversity, they have applications in many fields, such as catalysis, new materials, photochemistry, electrochemistry and medicine.[18–20, 150, 218, 260–263]

For instance, some POMs have been found to possess antiviral or antibacterial activities.[264, 265] POMs have been proven to be active against Gram-positive and Gram-negative bacteria, being more effective than common antibiotics. Their antibiotic effect can be rationalised by the inhibition of specific enzymes through specific interactions with the polyoxometalate species. Moreover, they also present great synergy with some of this conventional antibiotic agents, which is important in the treatment of highly resistant bacteria. Besides that, certain POMs also interact with some surface proteins located on viral envelopes, sabotaging their virus replication .[266]

Besides these antibiotic and antiviral activities of POMs, some POMs also have antitumoural activities.[40, 267] Some years ago, $[Mo_7O_{24}]^{6-}$ was proven to be effective against different cancer cells with an activity comparable with available drugs.[6, 39] The interaction of heptamolybdate with key phosphate ester biomolecules like DNA and RNA—usually through their phosphate moiety, as it is known—[268–270]has been pointed as a key factor of its antitu-

moural activity.[166]

The formation and cleavage of the phosphoester bond in biomolecular models is a hot research topic since this bond is used as a structural motif as well as for energetic storage in biological systems. The fundamental property of this bond for such essential tasks is the slow kinetics for its cleavage, as it guarantees excellent stability and allows great control using enzymes.[128–130]

During the last years, molybdenum species have been discovered to promote the hydrolysis of the phosphoester bond. Among these hydrolysis promoters, we can find a variety of structures: molybdocene derivatives,[14, 157–160] dioxomolybdates,[13, 15] molybdates[161–163] and polyoxometalates.[9–12, 164–166]

Absilis *et al.* showed an improved activity in the phosphoester cleavage of different models of ATP, DNA and RNA (NPP, BNPP, and HPNP, Figure 5.1) in solutions of molybdate at different pH.[9–11] The POM species identified as active in the hydrolysis of phosphodiester models was $[Mo_7O_{24}]^{6-}$. The heptamolybdate was an unexpected catalyst, being the first negative charged and coordinately saturated species to show activity towards phosphate ester hydrolysis. This species should overcome a significant barrier to approaching a negatively charged phosphate before hydrolysis occurs.

The characterisation of the intermediates and transition states in those reactions involving polyoxometalate structures is hard to accomplish through experimental work. Because of that, different techniques have been used to identify some intermediate species in their mechanisms as in the works of Absilis *et al.*[9–12], but still, there is a lack of understanding of the

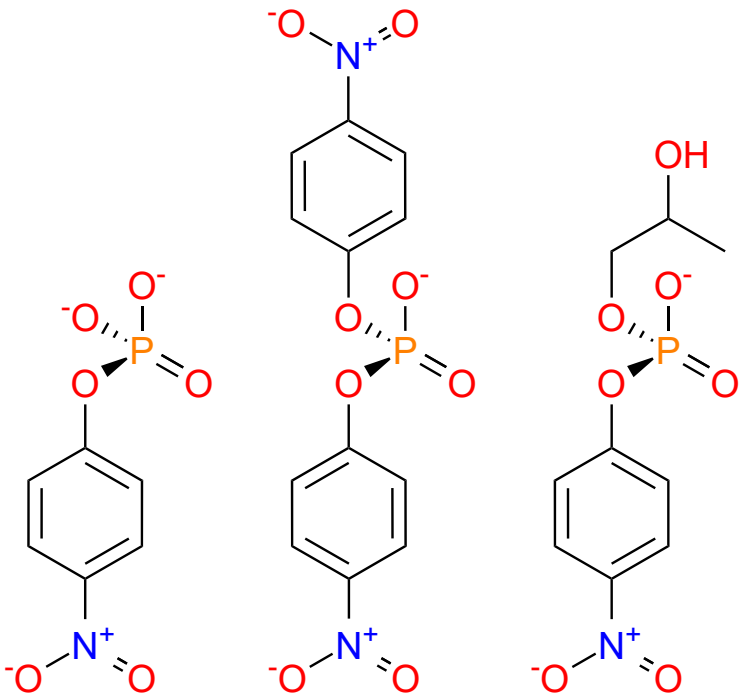

Figure 5.1: Model substrates. From left to right: 4–nitrophenylphosphate (NPP), bis(4–nitrophenyl)phophate (BNPP), and 2–hydroxypropyl–4–nitrophenylphosphate (HPNP).

catalytic mechanism. Using computational methods can help unveil the catalysis of these complex reactions..**[SalazarMarcano2023Feb]** Computational studies have been very useful in the study of the hydrolysis of different phosphate ester model substrates, like 4–nitrophenylphosphate (NPP), 2–hydroxypropyl–4–nitrophenylphosphate (HPNP), pyrophosphate (PP), and bis(4–nitrophenyl)phophate (BNPP).[167, 271–273]

The preferred reaction mechanism for phosphate ester hydrolysis can vary considerably depending on the substrate nature, the catalyst, and the medium (pH, solvent, etc.). Because of that, some aspects of this reaction remained

controversial and have been matter of discussion during the last years.[128, 167–171, 274, 275]

Recent studies of Duarte *et al.*[44, 180] showed a differential behaviour of the cleavage of phosphoester dianions as a function of good and bad leaving groups in basic media. Good leaving groups showed a preference for a pathway with a loose transition state. In contrast, bad leaving groups preferred a substrate-assisted pathway, in which a phosphorane formation was coupled with a proton transfer to the phosphate to increase its electrophilicity. In other works in a more acidic media, the monoanionic phosphates seem to activate the cleavage of the phosphoester bond by transferring its proton to the leaving group.[181–183] In the case of the phosphodiester molecules, the cleavage is more difficult, pointing to tighter transition states.[172–174, 177–179, 184]

With such a complicated picture, the specific pathway of a catalysed phosphate diester hydrolysis is very sensible to the ability of the catalyst to stabilise one transition state or the other. In this context, theoretical models are critical to elucidate the ongoing mechanism in every case.

In previous chapters we discussed various dinuclear molybdate species as promoters of the phosphoester bond hydrolysis .[276–279] These similar compounds could be obtained by *i)* nucleation processes of molybdenum(VI) complexes or *ii)* by breaking up processes of polyoxometalate structures. Although these dinuclear species are good candidates for phosphoesterase activity, experiments of Absilis *et al.* on phosphodiesters suggested that these substrates hydrolyse through different mechanisms than monoesters in presence of POMs, keeping the polyoxometalate structure intact during the course of the reac-

tion.[9, 11]

This work uses computational methods to elucidate key aspects of the mechanisms by which the $[Mo_7O_{24}]^{6-}$ heptamolybdate structure catalyses the hydrolysis of BNPP and HPNP, and to explain the different results obtained in the works of Absilis *et al.*[9, 11] We expect that this work will help to understand and rationalise how the negatively charged polyoxometalate structures can catalyse phosphodiester hydrolysis to optimise such catalysts for improved performance.

5.2 Computational Details

Calculations were carried with the Gaussian 16 Revision A.03 simulation software.[188] These calculations were made with the B3LYP DFT hybrid functional, that uses the Becke's three parameter exchange correlation that mixes Hartree-Fock exact exchange with Slater's and Becke's exchange functional;[84] whereas the local correlation functional corresponds to the non-local VWN functional with the Lee, Yang and Parr correlation functional.[87] The Los Alamos National Laboratory 2 effective core potential with double zeta (LANL2DZ) and f polarisation functions was used for the molybdenum atoms,[192–196] and the double-zeta split valence basis set including d and p polarisation functions and s and p diffuse functions for non-hydrogen atoms 6-31+G** was used for the rest of the atoms. Polarisable Continuum Model was used to take into account the implicit solvent.[123] Transition state geometries were optimised and characterised by frequency calculations. The intrinsic reaction coordinate was followed to obtain the reactants and products geome-

tries, followed by unconstrained optimisations.[197] Energies of mechanistically relevant results were refined using the 6-311++G($3df$,$2p$) basis set.[199] Dispersion effects were included using the third version of Grimme correction with the Becke-Johnson damping.[98]

The wavefunctions corresponding to the transition states have been analysed through the Quantum Theory of Atoms in Molecules (QTAIM) to explore the topology of the electron density.[112] This methodology allows us to exhibit the bonding scheme and the evolution of the electron density in the transition states to gain insight into the mechanistic process of the hydrolysis. Such analyses have been performed with the AIMAll software.[202]

5.3 Results and Discussion

As discussed previously, experimental results showed that the hydrolysis reactions of BNPP and HPNP were accelerated in presence of heptamolybdate.[9, 11] However, in contrast with the hydrolysis reaction of NPP—in which the heptamolybdate structure was not maintained—the $[Mo_7O_{24}]^{6-}$ structure is kept until the end of the hydrolysis of these phosphodiester substrates.

Both BNPP and HPNP are phosphodiester models, but HPNP has a mobile hydroxy group—like RNA—that can affect to its reactivity. We expect both hydrolysis mechanisms to diverge as the acting nucleophiles differ. With BNPP, an external water molecule acts as the nucleophile, whereas with HPNP, the substrate attacks the phosphorous atom intramolecularly. Details of both reaction mechanism are shown in separate sections.

Table 5.1: Relative energies (in kcal/mol), relevant distances (Å) and angles (degrees) for the species involved in the non-catalysed BNPP hydrolysis mechanism

Species	ΔE_{elec}	ΔG	P–O(LG)	P–O(Nu)	O(LG)–P–O(Nu)
Reac	0.0	0.0	1.666	3.754	110.3
TS1	35.8	36.6	1.688	2.284	168.5
Int	24.1	27.1	1.828	1.738	170.6
TS2	25.8	28.3	2.194	1.701	169.5
Prod	−9.9	−6.5	3.566	1.631	145.4

Of course, if we want to determine the catalytic ability of these mechanisms, we have to compare them with the non-catalysed mechanisms for the hydrolysis of both substrates.

Hydrolysis of BNPP

To prove any catalytic effect, we must first study the non-catalytic case. As shown in Table 5.1 and depicted in Figure 5.2, the first transition state resulting in a phosphorane formation is the rate-determining step with a high energetic barrier (ΔG=36.6 kcal/mol). On the contrary, the second transition state is only 1.2 kcal/mol over the phosphorane intermediate, located 27.1 kcal/mol over the reactant state.

Next, we analysed the catalytic mechanism for BNPP hydrolysis by heptamolybdate, which confirmed the tight associative mechanism. This mechanism is depicted in Figure 5.3, where we can appreciate that a transient phosphorane intermediate is reached, located only 22.1 kcal/mol over the reactants. The transition state for its formation is located very close in energy to the phosphorane itself, being only 0.4 kcal/mol higher in free energy. The transition state for the leaving group departure is the highest point in the mechanism,

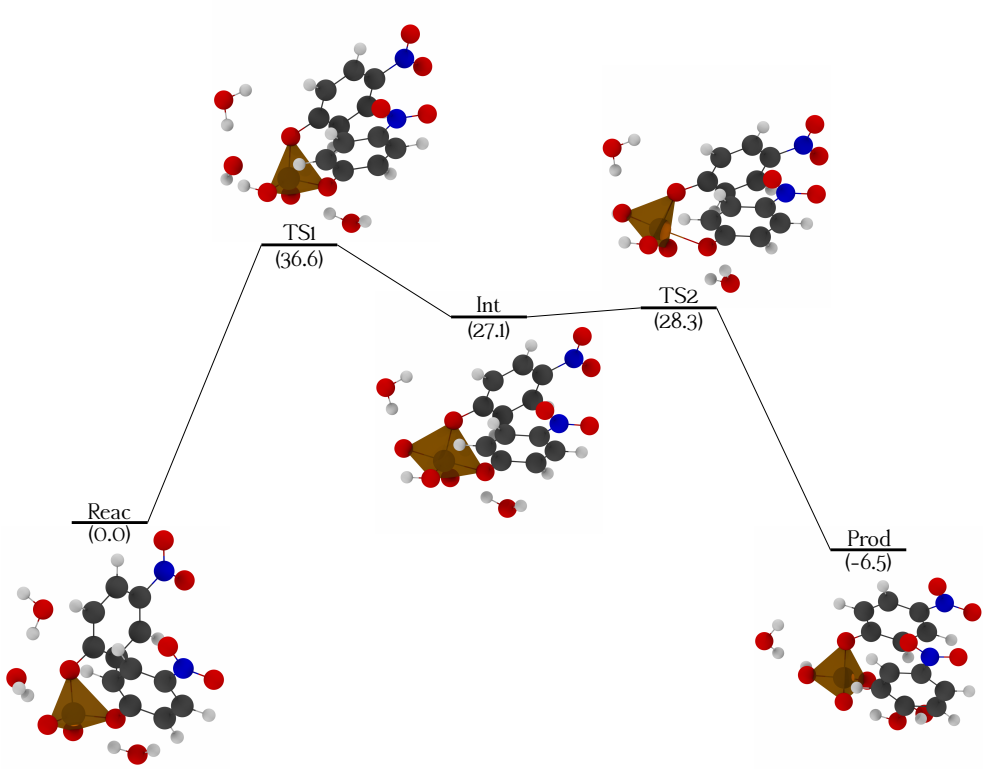

Figure 5.2: Calculated free energy profile for non-catalysed BNPP hydrolysis with two extra water molecules. Relative free energies are in kcal/mol.

25.0 kcal/mol over the reactant complex. The occurrence of the phosphorane and the short P−O distances to the nucleophile and leaving group at the transition state structures (see Figure 5.4 and Figure 5.5) confirm the associative character of the mechaninsm. After its departure, the negatively charged leaving group will ultimately be protonated through concatenated proton transfers involving the solvent and the previously protonated oxygen of the polyoxometalate structure. After this exergonic hydrolysis—$\Delta G = -10.3$ kcal/mol—a structure containing the NPP—a phosphate monoester—is obtained as a prod-

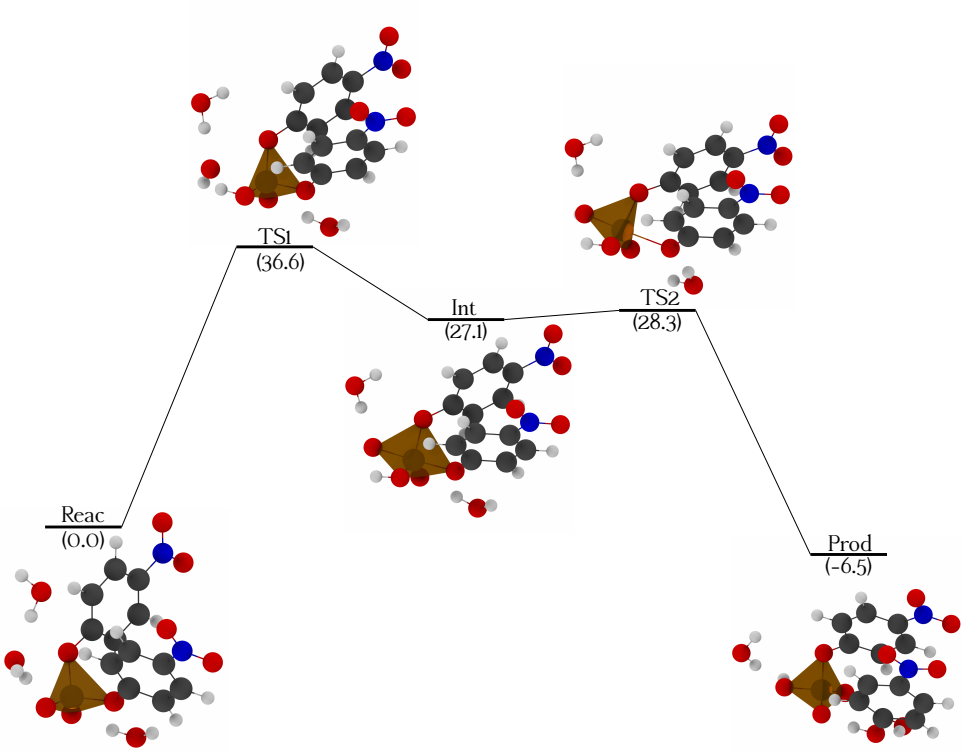

Figure 5.3: Calculated free energy profile for BNPP hydrolysis in presence of heptamolybdate. Relative free energies are in kcal/mol.

uct. This species is known to hydrolyse through a different—less associative—mechanism. A detailed description of the energetic and geometric data are shown in Table 5.2.

Now we can compare the energy values of this mechanism with the data for the non-catalysed hydrolysis, shown in Figure 5.2. By doing so, we can observe a catalytic effect, as the energetic barrier of this process is lowered by 11.6 kcal/mol. We can see a major stabilisation of both the phosphorane intermediate by 5.0 kcal/mol, and the transition state leading to its formation by 14.1 kcal/mol. By stabilising this transition state, the polyoxometalate

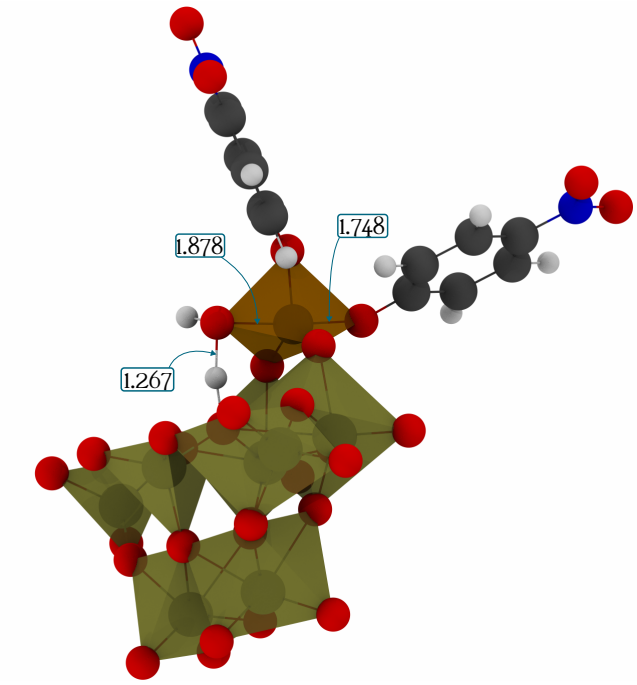

Figure 5.4: Transition state structure leading to the formation of the phosphorane in the BNPP hydrolysis mechanism in presence of $[Mo_7O_{24}]^{6-}$. Distances are in Å.

Table 5.2: Relative energies (in kcal/mol), relevant distances (Å) and angles (degrees) for the species involved in the catalysed BNPP hydrolysis mechanism.

Species	ΔE_{elec}	ΔG	P–O(LG)	P–O(Nu)	O(LG)–P–O(Nu)
Reac	0.0	0.0	1.633	3.434	162.1
TS1	22.8	22.5	1.748	1.878	174.7
Int	21.1	22.1	1.775	1.786	174.4
TS2	24.6	25.0	2.198	1.701	175.1
ProdH*	11.0	8.9	4.796	1.624	159.9
Prod	−8.2	−10.3	4.266	1.610	144.2

* Product before proton transfer to leaving group.

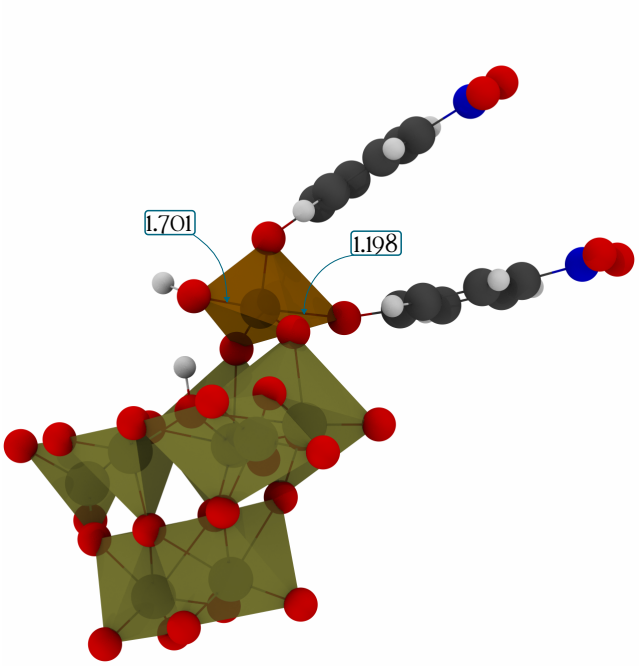

Figure 5.5: Transition state structure leading to the breaking of the phosphorane in the BNPP hydrolysis mechanism in presence of $[Mo_7O_{24}]^{6-}$. Distances are in Å.

structure changes the rate limiting step, with important consequences, as the nature of the leaving group could now significantly influence the overall kinetics of the reaction.

Hydrolysis of HPNP

As we stated previously, the mechanism by which HPNP is hydrolysed is qualitatively different as the nucleophile is part of the substrate. This intramolecular attack leads to an energetically lower pathway in which we obtain a stabilised ring structure that complicate any posterior hydrolysis.

Like before, we studied the non-activated mechanism before the catalysed

Table 5.3: Relative energies (in kcal/mol), relevant distances (Å) and angles (degrees) for the species involved in the non-catalysed HPNP hydrolysis mechanism

Species	ΔE_{elec}	ΔG	P−O(LG)	P−O(Nu)	O(LG)−P−O(Nu)
Reac	0.0	0.0	1.662	3.344	139.7
TS1	31.4	27.5	1.695	2.257	159.3
Int	20.8	21.4	1.830	1.744	166.3
TS2	20.5	21.3	2.283	1.668	166.6
Prod	−3.1	−3.4	3.810	1.647	129.2

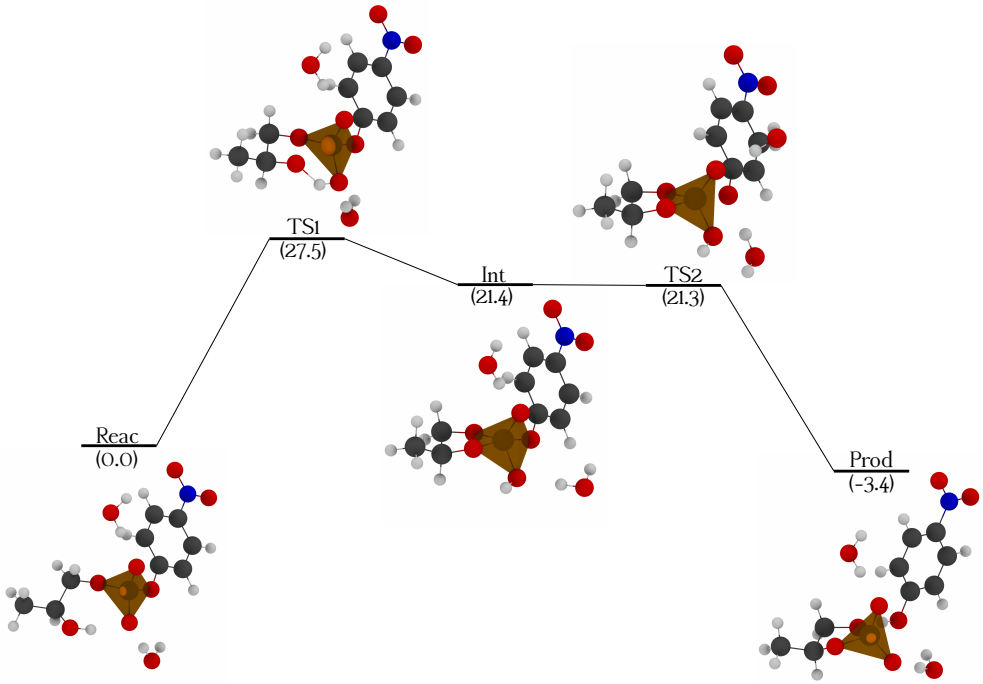

Figure 5.6: Calculated free energy profile for non-catalysed HPNP hydrolysis with two extra water molecules. Relative free energies are in kcal/mol.

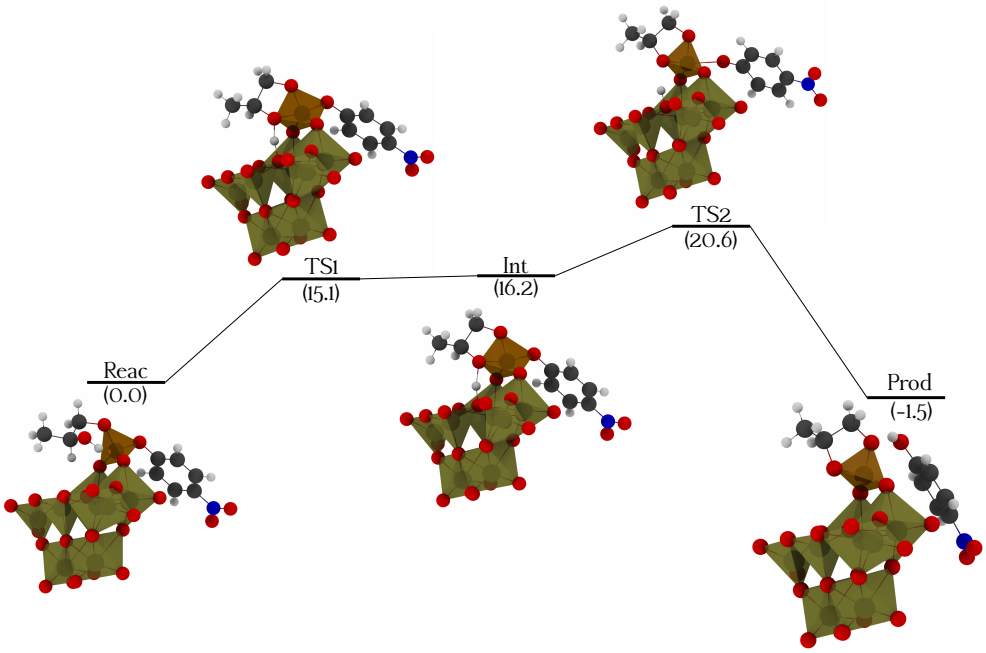

Figure 5.7: Calculated free energy profile for HPNP hydrolysis in presence of heptamolybdate. Relative free energies are in kcal/mol.

case. The energetic and geometric data for the non-catalysed hydrolysis of HPNP are listed in Table 5.3 and depicted in Figure 5.6. As expected, we observe an energetically lower path compared to the BNPP one, in which the first transition state (ΔG=27.5 kcal/mol) is still the rate determining step in absence of the polyoxometalate structure.

The POM-activated mechanism depicted in Figure 5.7 shows that reaching the phosphorane structure (ΔG=16.2 kcal/mol) require surpassing a transition state (Figure 5.8) located at only 15.1 kcal/mol over the reactant state. The rate-determining step is the leaving group departure, proceeding through a transition state at 20.6 kcal/mol over the reactant state.

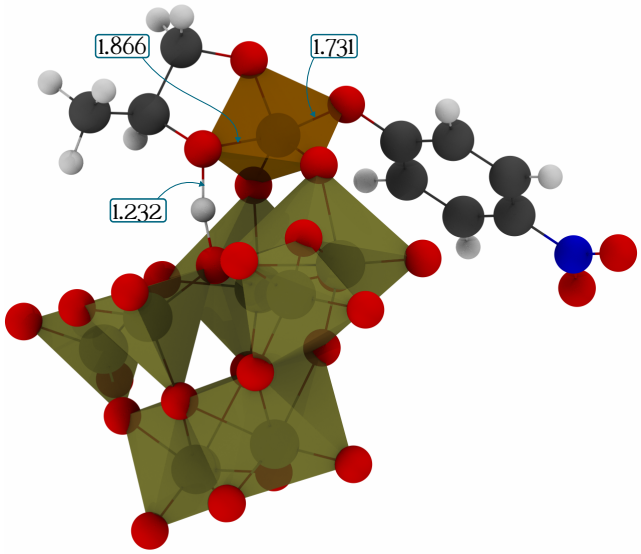

Figure 5.8: Transition state structure leading to the formation of the phosphorane in the HPNP hydrolysis mechanism in presence of $[Mo_7O_{24}]^{6-}$. Distances are in Å.

In comparison with the BNPP phosphorane, this associative intermediate is closer to the reactant state, with a shorter bond to the leaving group (1.745 Å compared to 1.775 Å) and a longer bond to the nucleophile (1.816 Å compared to 1.786 Å). On the contrary, the transition state for the phosphorane rupture is displaced to the products, with a P−O distance to the leaving group of 2.478 Å(see Figure 5.9). Again, the leaving group will accept a proton from the protonated polyoxometalate through proton transfers with the solvent. Energetic and geometric details are reported in Table 5.4.)

Once again, a catalytic effect is clear, as the energetic barrier of this process is lowered by 9.1 kcal/mol compared to the non-catalysed hydrolysis in

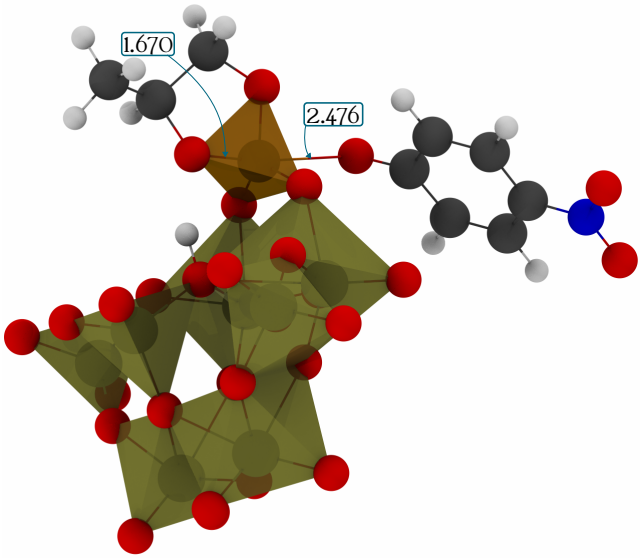

Figure 5.9: Transition state structure leading to the breaking of the phosphorane in the HPNP hydrolysis mechanism in presence of $[Mo_7O_{24}]^{6-}$. Distances are in Å.

Figure 5.6. We can see similar patterns to the BNPP case: a big stabilisation of the phosphorane formation—the first transition state is lowered by 12.4 kcal/mol and the intermediate by 5.2 kcal/mol—as well as an induced change in the rate determining step to the second transition state.

These results highlight the strong effect of the presence of $[Mo_7O_{24}]^{6-}$, which leads to the catalysis of the hydrolysis of phosphodiester substrates. The findings of our research are in agreement with the experimental results of Absilis *et al.*[9, 11] that suggested this catalytic activity. Moreover, it also agrees with our previous theoretical work, which highlighted a similar structure to promote the hydrolysis of phosphate monoester substrates. This din-

Table 5.4: Relative energies (in kcal/mol), relevant distances (Å) and angles (degrees) for the species involved in the catalysed HPNP hydrolysis mechanism

Species	ΔE_{elec}	ΔG	P–O(LG)	P–O(Nu)	O(LG)–P–O(Nu)
Reac	0.0	0.0	1.635	3.361	141.1
TS1	15.6	15.1	1.731	1.866	167.2
Int	15.6	16.2	1.745	1.816	166.9
TS2	21.8	20.6	2.478	1.670	172.3
ProdH*	17.9	11.1	4.543	1.629	151.4
Prod	0.6	−1.5	3.727	1.618	108.5

* Product before proton transfer to leaving group.

uclear dibridged molybdate motif—a little looser in the case of phosphate monoesters—could be important in the catalysis of phosphoester bonds by molybdenum species.

Mechanisms with Wolfram Species

Experiments with the same substrates (BNPP and HPNP) and an analogous $[W_7O_{24}]^{6-}$ cluster yielded no significant differences in cleavage rates to the experiments without promoter. The inactivity of polyoxowolframates towards phosphate ester catalysis was explained with its stiffness and inability to partial detach the WO_4 units through the W–O bonds, which will ultimately impede the formation of the initial heptawolframate structure including the phosphate moiety.

Nevertheless, we also wanted to compare their mechanisms once the substrate is incorporated into the polyoxometalate scaffold to see if a less favourable hydrolysis process can explain its lack of activity. In presence of this wolfram species ($[W_7O_{24}]^{6-}$), BNPP hydrolysis goes through an intermedi-

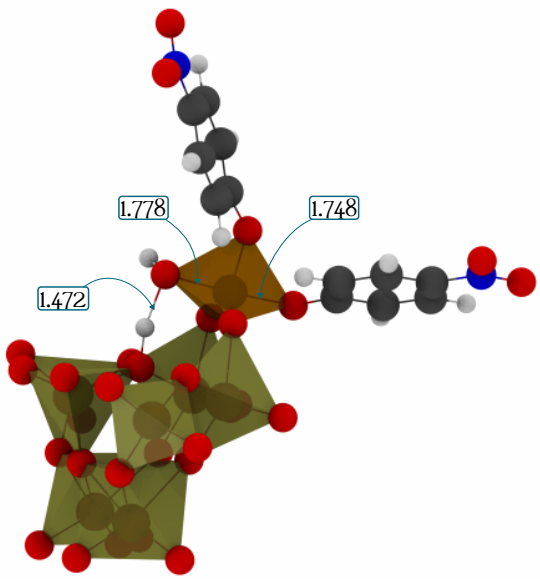

Figure 5.10: Phosphorane structure for the BNPP hydrolysis in presence of $[W_7O_{24}]^{6-}$. Distances are in Å.

ate which is located 25.8 kcal/mol over the reactant state. This phosphorane is almost 4 kcal/mol higher in energy than in the molybdenum case, which could result in higher transition states and a lesser catalytic activity than the molybdenum case.

Structural data also show that the intermediate is slightly more displaced to the reactant state. P – O distances to the leaving group and nucleophile are 1.748 Åand 1.778 Å, respectively, as seen in Figure 5.10. Those distances are also smaller than in the molybdenum case, showing a more associative character. The global reaction with wolfram species is also exergonic but less favourable than with the molybdenum analogue, releasing 8.4 kcal/mol of free energy.

To summarise, wolfram polyoxometalates are known to be less prone than molybdenum POMs to suffer intramolecular exchange, in contrast to polyoxomolybdates. Because of that, phosphate molecules are less likely to interact and be activated by these wolfram species. In addition to that, the energetics of the phosphorane intermediates also suggest that heptawolframate could have a lesser catalitic activity than its analagous heptamolybdate.

Topological Analysis

The catalytic process promoted by the molybdate structures has been studied with the QTAIM methodology. This procedure allows us to explore the electron density topology and it is extremely useful to describe chemical bonds. We can get important insights by using the Bond Critical Points (BCPs) of the breaking and emerging bonds in the transition states and comparing the situation between the catalysed and non-catalysed mechanisms.

In Figure 5.11, we can see a depiction of the bonding schemes and the corresponding properties of the bond critical points for the involved transition states of both non-catalysed and catalysed BNPP hydrolysis reaction. This figure also presents the integrated charges for the P atom and the surrounding O atoms. It is observed that the heptamolybdate slightly increases the charge on the P atom from 3.58 to 3.62 au (highlighted in orange). This change indicates that the heptamolybdate increases the electrophilicity of the P atom, making him more prone to a nucleophilic attack.

In addition, we can observe differences in the electron density on the BCPs between the catalysed and non-catalysed transition states for the nucleophilic

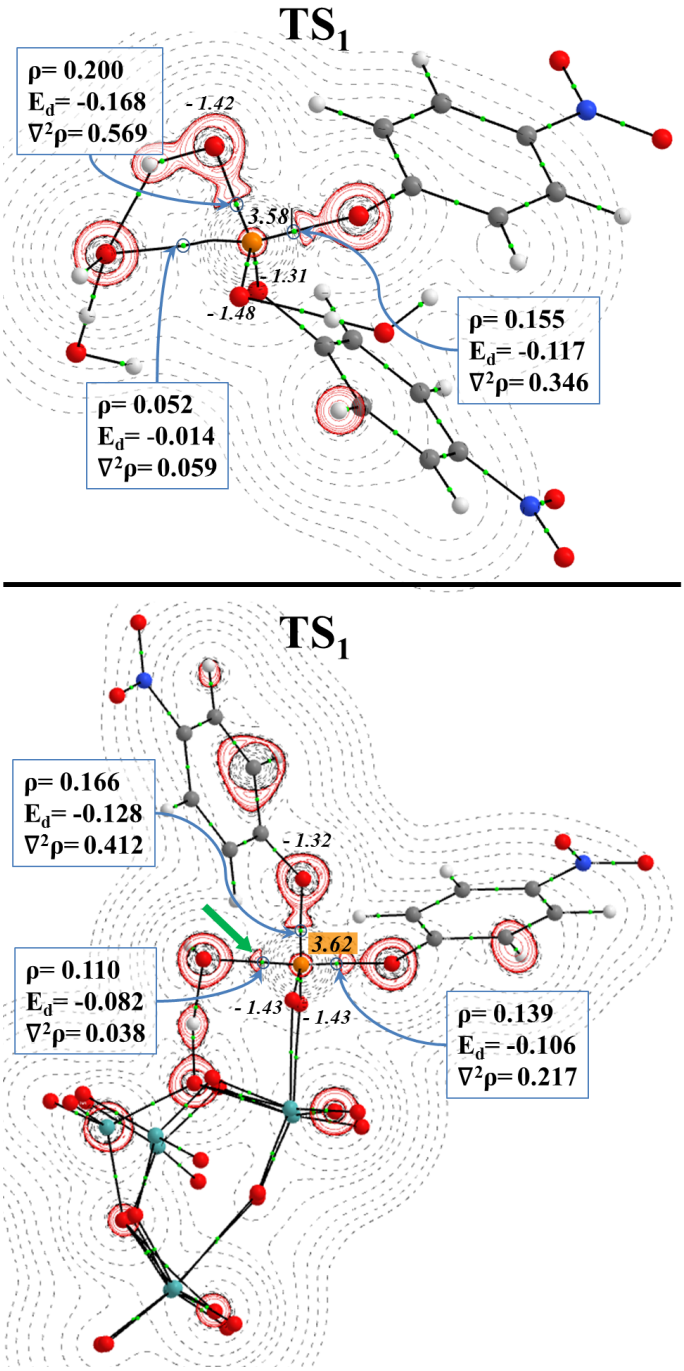

Figure 5.11: Bonding scheme properties for the BCPs involved in TS1 for the BNPP hydrolysis and the integrated charges for the P atoms and surrounding O atoms. The contour maps for the $\nabla^2\rho$ are plotted in the plane containing the BCPs involved in the reaction mechanism. Black dotted lines represent charge depletion zones, while red lines represent charge concentration zones. Up, non-catalytic process, down, catalytic process in presence of the heptamolybdate.

attack. In presence of heptamolybdate, the the electron density value (ρ) for the emerging bond grows from 0.052 to 0.110 au, indicating a stronger union. Moreover, the electron energy density (E_d) change (from -0.014 to -0.082 au) points to the stabilisation of this emerging bond due to the polyoxometalate presence. This result is corroborated by the contour map for the laplacian of the electron density $\nabla^2\rho$, plotted in the plane containing the nucleophylic O atom, the P atom and the O atoms of the leaving group. Also, we can observe—emphasised using a green arrow—a negative zone for $\nabla^2\rho$ between the nuchelophylic O and P atoms manifesting a charge concentration zone. Moreover, it is observed that one H atom of the nucleophile is forming a bond with the polyoxometalate structure, raising the nucleophilicity of the O atom.

Similar results have been obtained regarding the HPNP hydrolysis (Figure 5.12). The coordination of heptamolybdate to the phosphate group yields more positive integrated QTAIM charges for the P atom. For the non-catalysed process, we obtain a value of 3.56 au, while for the catalysed reaction, this value increases to 3.61 au. Regarding the values of the BCPs, a stabilisation of the forming bond between the nucleophile and the P atom is observed, with higher values for the ρ and E_d: 0.013 and -0.086 au, respectively. The charge concentration area in the $\nabla^2\rho$ contour map of the catalysed TS—again, accentuated with the green arrow—confirms this stabilisation due to the polyoxometalate presence. In addition, the H atom of the nucleophilic OH group is creating a bond with the polyoxometalate structure and increasing the nucleophilicity of the oxygen atom.

The study for the second transition state in both hydrolysis (BNPP and

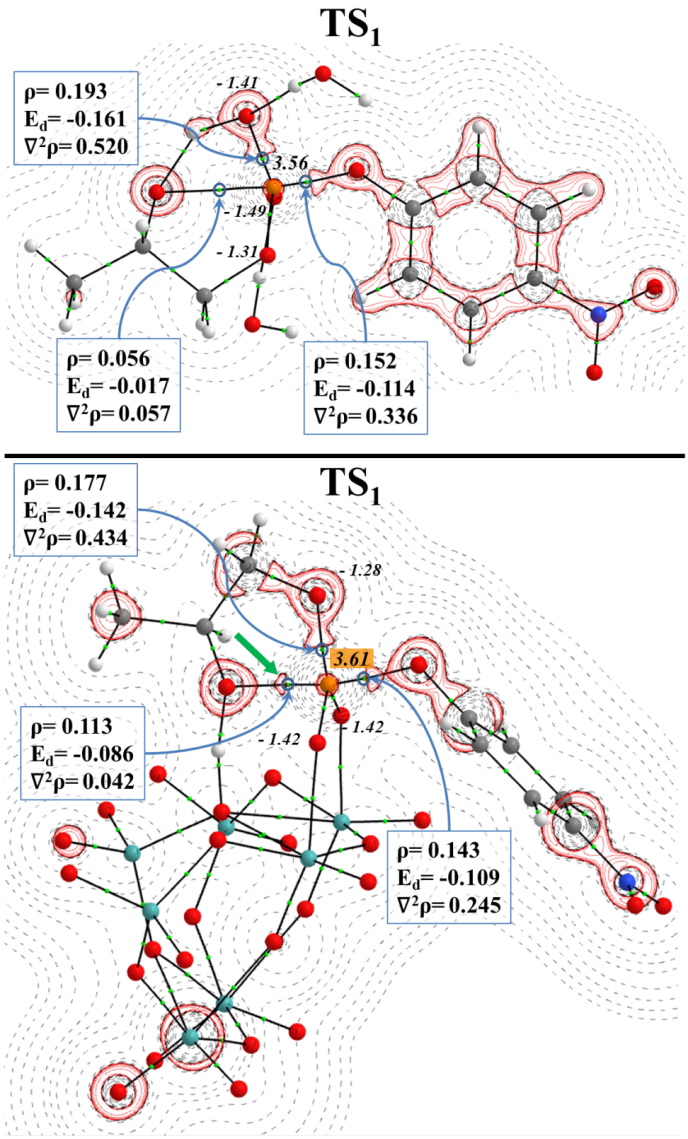

Figure 5.12: Bonding scheme properties for the BCPs involved in TS1 for the HPNP hydrolysis and the integrated charges for the P atoms and surrounding O atoms. The contour maps for the $\nabla^2\rho$ are plotted in the plane containing the BCPs involved in the reaction mechanism. Black dotted lines represent charge depletion zones, while red lines represent charge concentration zones. Up, non-catalytic process, down, catalytic process in presence of the heptamolybdate.

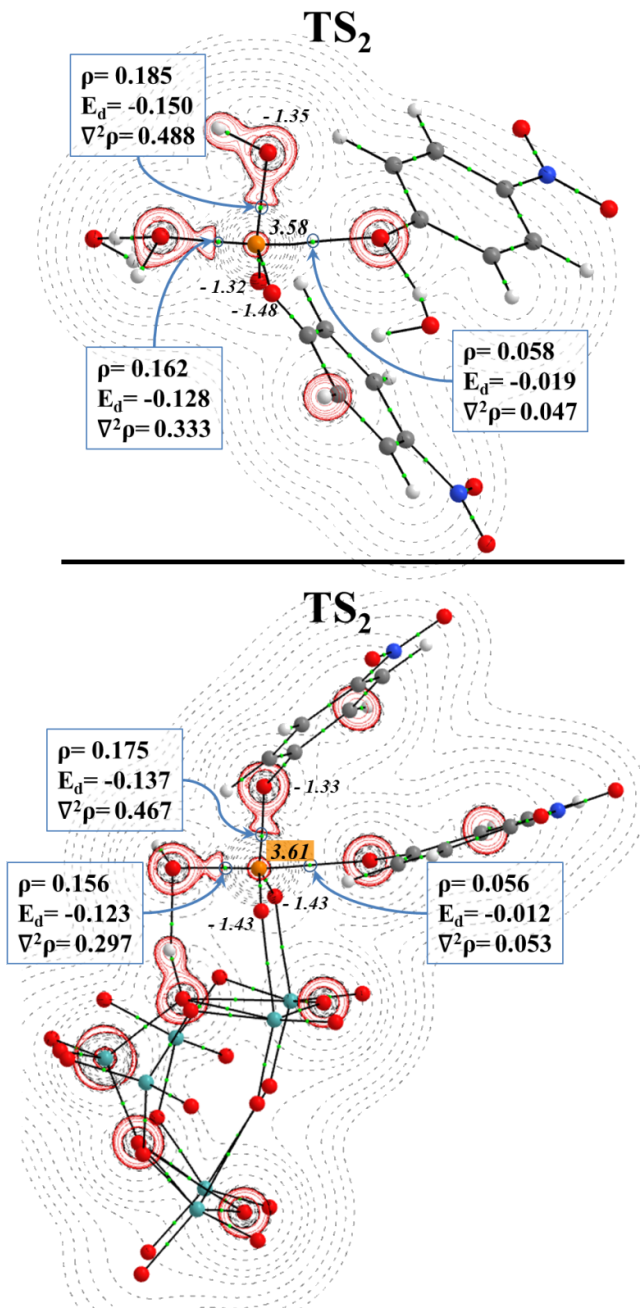

Figure 5.13: Bonding scheme properties for the BCPs involved in TS2 for the BNPP hydrolysis and the integrated charges for the P atoms and surrounding O atoms. The contour maps for the $\nabla^2\rho$ are plotted in the plane containing the BCPs involved in the reaction mechanism, black dotted lines represent charge depletion zone, while red lines represent charge concentration zone. Up, non-catalytic process, down, catalytic process in presence of heptamolybdate.

HPNP) have been also performed (see Figure 5.13 and Figure 5.14). If we compare both of them with their non-catalysed cases, we can observe higher integrated charges on the P atom, and the ρ and E_d values suggest a weaker bond to the leaving group.

These results indicate that the presence of the heptamolybdate attached to the phosphate groups results in a more positive P atom and an increase in the nucleophile strength due to the proton transfer to the polyoxometalate structure. This gives a more reactive O atom and a favoured phosphorane formation.

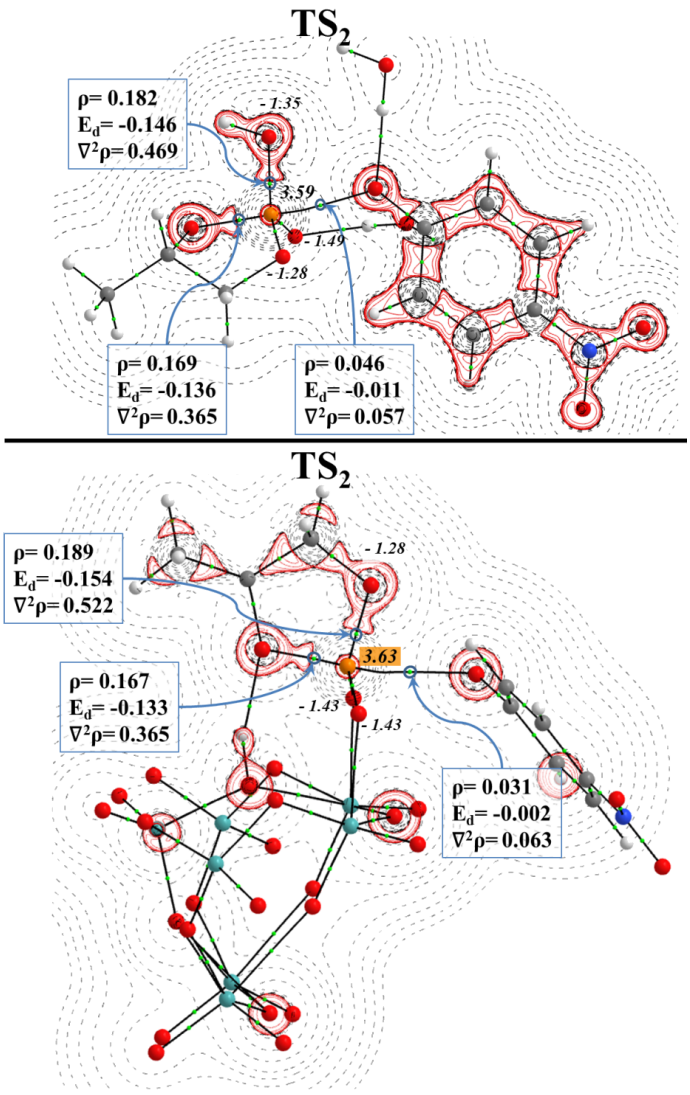

Figure 5.14: Bonding scheme properties for the BCPs involved in TS2 for the HPNP hydrolysis, and the integrated charges for the P atoms and surrounding O atoms. The contour maps for the $\nabla^2\rho$ are plotted in the plane containing the BCPs involved in the reaction mechanism, black dotted lines represent charge depletion zone, while red lines represent charge concentration zone. Up, non-catalytic process, down, catalytic process in presence of heptamolybdate.

5.4 Conclusions

Our results confirm that the valence-saturated and negatively charged heptamolybdate catalyses the hydrolysis reaction of the studied phosphate diester models: BNPP and HPNP. We have described in detail both catalysed mechanisms in this study, obtaining pathways with lower energetic barriers than the non-catalysed reactions by 11.6 and 9.1 kcal/mol for BNPP and HPNP hydrolysis, respectively. These results support the available experimental data and are coherent with some recent theoretical studies which point towards a structural motif involving dibridged molybdates with octahedral coordination to be key in the catalysis of these kind of phophoester hydrolysis reactions. An analogous mechanism with a more rigid wolfram species was also analysed and proved to proceed through less accessible intermediates. We also performed a topological analysis that confirms that the molybdate structure increases the electrophilicity of the phosphorous atom, lowering the energy needed for the rate-limiting step.

Chapter 6

FURTHER WORK: THIS IS NOT OVER

6.1 Overview

This thesis addresses relevant aspects that explain how molybdenum species can catalyse the hydrolysis of phosphoester bonds. Although this ability has been linked with antitumoural activity, applying this information to the medical world is far from simple and direct. Phosphoester models used in this work (NPP, BNPP, HPNP) are very different from the DNA, RNA, and ATP biomolecules, key targets in this approach. Their difference not only is explained by size—biomolecules are considerably larger—but also qualitatively, as the nature of the groups linked to the phosphorous atom can affect greatly to their reactivity. These differences could influence in the phosphoesterase activity of the polyoxometalate structures discussed previously in this thesis. To undertand the implications of our models in the biological world, we need to perform more realistic and costly simulations.

One step in that direction would be to use actual phosphoester biomolecules instead of smaller, more rigid and easier to hydrolyse models. By increasing the number of atoms and the degrees of freedom of the system the computational cost increases greatly. Nevertheless, we cannot simplify the methodology without sacrificing the accuracy needed to describe these mechanisms

Figure 6.1: Representation of the '5-AC-'3 dinucleotide.

correctly. With all this in mind, we continued our studies using an adenine cytosine dinucleotide (Figure 6.1) as a small fragment of the DNA chain.

Apart from modifying the substrate, we must consider other types of polyoxometalate structures. The kind of species studied in this thesis are known to be toxic in biological environments. Nevertheless, properties of the POMs can be modified by functionalising them with biological building blocks—as, for example, aminoacids—to tune their biological properties. This approach have been tried experimentally by testing the phophoesterase activity of a functionalised octamolybdate against ATP,[12] but no following attempts have been made on DNA-like substrates. These modifications could also affect the catalysis of the hydrolysis reaction, so further studies are needed to get a broader

view of the implications of the polyoxometalate functionalisation.

6.2 Partial Results

Using the ADF program package, we applied Density Functional Theory to perform geometry optimisations. Our methodology included the BP86 functional and a triple zeta slater-type basis set with two polarisation functions and the COSMO model to include solvent effects. Following these approaches, we scrutinised the potential energy surface to find key structures in the hydrolysis mechanism of the '5-AC-'3 dinucleotide attached to alanine- and glycylglycine-functionalised octamolybdate structures (Figure 6.2).

As we stated chapters before, phosphodiester molecules usually hydrolyse through compact pathways, specially when bad leaving groups are present. Furthermore, polyoxometalate structures are known to favour associative mechanisms, in which phosphorane intermediates are formed. So it is easy

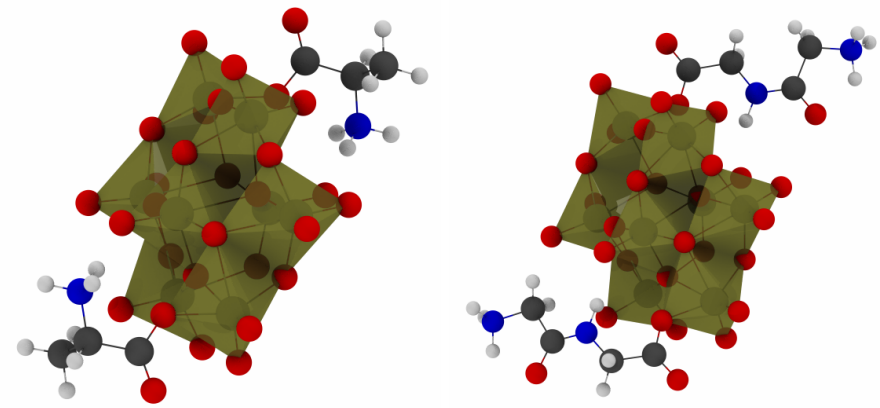

Figure 6.2: Representations of the octamolybdate structure functionalised with alanine (left) and glycylglycine (right).

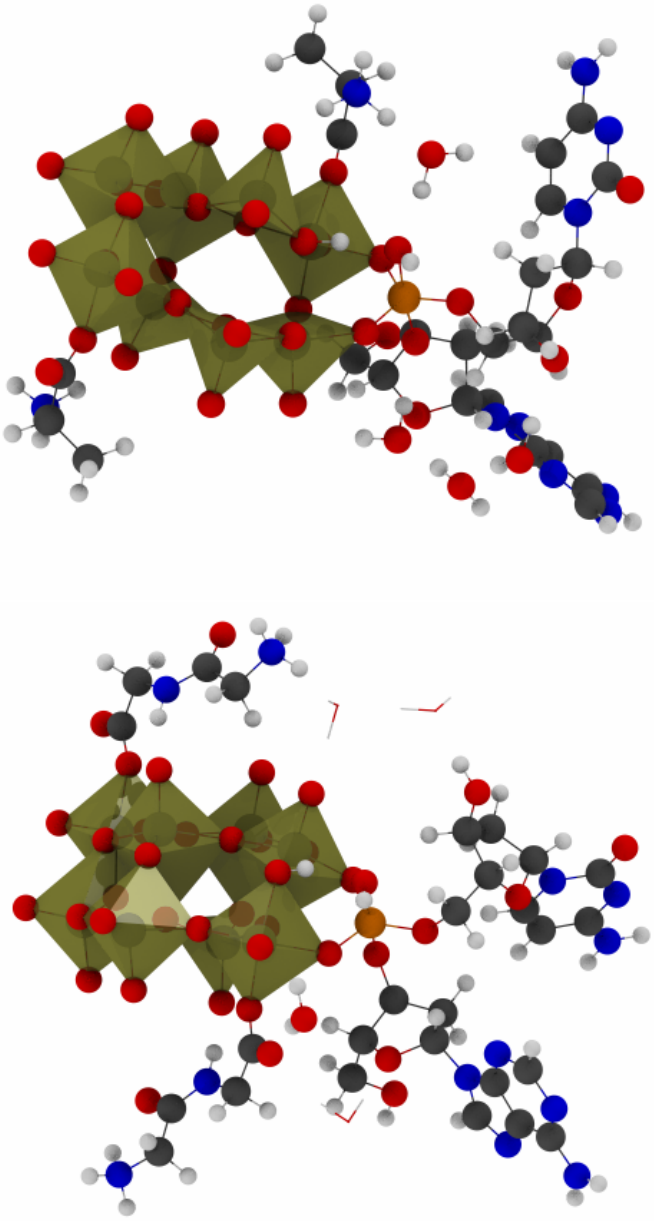

Figure 6.3: Partially optimised structures for the phosphorane intermediates with ala-octamolybdate (up) and glygly-octamolybdate (down).

to infer that this reaction will proceed through tight associative mechanisms involving phosphorane structures. In Figure 6.3 we can see an estimation of the structure of these intermediates. This structures were obtained using constrained optimisations keeping the P – O distances to the nucleophile fixed at 1.79 Å—value obtained after scanning this coordinate—,while relaxing the rest of the system. These phosphorane intermediates are around 30 kcal/mol over the reactant state, but they are in process to be refined with relaxed optimisations.

Transition state structures and the rest of the key stationary points will be obtained through further energy optimisations and connected trough intrinsic reaction coordinate calculations to obtain a complete and thorough description of the reaction mechanism.

6.3 Follow-up Studies

Apart from this ongoing theoretical work, which could illuminate the applicability of the functionalised polyoxometalates on biological phosphate ester targets, we could improve this approach by combining it with experimental studies. Another bioavailable dinucleotide, like nicotinamide adenine dinucleotide (NAD), could be tested as a phosphoesterase target by heptamolybdate. The combination of a experimental work and computational characterisation of the underlying mechanism would give very insightful information and a confirmation of the theoretical predictions.

It could be also riveting to deepen our knowledge by addressing the previous steps by which flexible polyoxometalates—like POMos—incorporate

phosphates in their structure, comparing it with the rigid polyoxometalate analogues—like POWs—which fail to have phosphoesterase activity. This approach could be tricky, since the detachment of molybdate units could lead to multiple mechanisms of heteropolyoxometalate formation. This topic is far from easy due to the multiple possible structures and configurations that can emerge, being the most stable ones also dependant on different conditions as pH or molybdate and phoshphate concentrations.

Chapter 7

CONCLUSIONS

This thesis aimed to use computational theoretical chemistry to explain how different molybdenum species have phosphoesterase activity. Of course, testing the catalytic activity of every imaginable molybdenum species with every molecule containing a phosphate ester bond was impossible. However, we have explained the potential catalytic activity of various molybdate structres—from small molibdenum complexes to polyoxometalate clusters—with different model substrates—phosphate monoesters in chapters 3 and 4 and phosphate diesters in chapter 5.

We started in chapter 3 with the $MoO_2Cl_2(DMF)_2$ complex. Since in the experimental works there was no clear catalyst candidate, we studied its speciation before trying to guess the active species that acts as the catalysis initiator. Our results supported the experimental findings reported in previous studies that pointed to DMF release and Mo−Cl bond breakage. After that we found a species that was ready to proceed through nucleation processes which—depending on the conditions—could end up giving polyoxometalete structures. We proposed two different pathways depending on the complex concentration. Experiments with lower concentrations of the initial complex, showed a slower catalysis. In those conditions, the formation of polynuclear species is disfavoured, and our proposed mechanism proceed through less favourable

mononuclear intermediates. With enough $MoO_2Cl_2(DMF)_2$ concentration, exergonic nucleation processes are favoured, giving polynuclear species. We choose dinuclear species from the wide range of polynuclear species that could catalyse the NPP hydrolysis since their interaction with phosphate molecules is more favourable than its succesive nucleation processes. After an exergonic inclusion of the phosphate to the molybdate structure, the nucleophilic attack and the consequent NPP hydrolysis showed lower energetic barriers than the uncatalysed reaction.

We found that, generally, the molybdate structure yielded a more electrophilic phosphorous and is able to activate the nucleophile by removing one of its protons. As a result, more compact associative mechanisms are favoured over dissociative ones. This behaviour is common to the different substrates and molybdate species treated in this thesis.

In Chapter 4 we considered the opposite approach to Chapter 3. Thus, whereas in Chapter 3 we started with a small complex that could nucleate to a polyoxometalate species, in Chapter 4 we depart from a polyoxometalate species ($[Mo_7O_{24}]^{6-}$) known to hydrolyse NPP while its nuclearity decreased. Experimental works proposed a pentanuclear intermediate as the possible active species in the hydrolytic process. Nevertheless, our studies suggested that the activation barrier for this pentamolybdate species is too high, and therefore, it can not be considered as a catalyst. Instead, we propose a dinuclear compound as the catalytic species, which decreased the energetic barrier and yielded an exergonic NPP hydrolysis with respect to the non-catalysed reaction.

In summary, the main conclusion of Chapters 3 and 4 is that dinuclear molybdate species are efficient catalysis for the hydrolysis of model phosphate monoesters. These dinuclear species can be formed through nucleation of molybdate species or through the fragmentation of polyoxometalate structures.

Next, in Chapter 5, we analysed the possibility that $[Mo_7O_{24}]^{6-}$ heptamolydbate could catalyse DNA and RNA models, represented by bis(4–nitrophenyl)phophate (BNPP) and 2–hydroxypropyl–4–nitrophenylphosphate (HPNP). Our calculations clearly showed associative mechanisms through phosphorane intermediates with lower energetic barriers than the non-catalysed analogues. Contrary to the phopshate monoester cases, the hydrolysis of phosphodiesters can be achieved without the fragmentation of the heptamolybdate sructure. This can be explained as the hydrolysis of phosphate diesters proceeds through more compact transition states that could fit within the heptamolybdate structure, whilst more reactive phosphate monoesters need less associative transition states.

Although the dinuclear species and the heptamolybdate species could appear to be very different at first glance, both structures provide with a structural motif that is properly designed to catalyse the hydrolysis of these phosphates. This could be useful in designing effective catalysts, which could also be tuned by functionalisation to lower their toxicity or improve its activity towards actual biological targets.

BIBLIOGRAPHY

(1) Ericsson, C. D.; Tannenbaum, C.; Charles, T. T. Antisecretory and Antiinflammatory Properties of Bismuth Subsalicylate. *Rev. Infect. Dis.* **1990**, *12*, S16–S20.

(2) Clark, P.; Tugwell, P.; Bennett, K. J.; Bombardier, C.; Shea, B.; Wells, G. A.; Suarez-Almazor, M. E. Injectable gold for rheumatoid arthritis. *Cochrane Database of Systematic Reviews* **1997**, DOI: 10.1002/14651858.CD000520.

(3) Mabeza, G. F.; Loyevsky, M.; Gordeuk, V. R.; Weiss, G. Iron Chelation Therapy for Malaria: A Review. *Pharmacol. Ther.* **1999**, *81*, 53–75.

(4) Sim, W.; Barnard, R. T.; Blaskovich, M. A. T.; Ziora, Z. M. Antimicrobial Silver in Medicinal and Consumer Applications: A Patent Review of the Past Decade (2007–2017). *Antibiotics* **2018**, *7*, 93.

(5) Köpf-Maier, P. Complexes of metals other than platinum as antitumour agents. *Eur. J. Clin. Pharmacol.* **1994**, *47*, 1–16.

(6) Fujita, H.; Fujita, T.; Sakurai, T.; Yamase, T.; Seto, Y. Antitumor Activity of New Antitumor Substance, Polyoxomolybdate, against Several Human Cancers in Athymic Nude Mice. *Tohoku J. Exp. Med.* **1992**, *168*, 421–426.

(7) Wang, X.-H.; Liu, J.-F.; Chen, Y.-G.; Liu, Q.; Liu, J.-T.; Pope, M. T. Synthesis, characterization and biological activity of organotitanium substituted heteropolytungstates. *J. Chem. Soc., Dalton Trans.* **2000**, 1139–1142.

(8) Wang, X.; Liu, J.; Li, J.; Yang, Y.; Liu, J.; Li, B.; Pope, M. T. Synthesis and antitumor activity of cyclopentadienyltitanium substituted polyoxotungstate [CoW11O39(CpTi)]7- (Cp=η5-C5H5). *J. Inorg. Biochem.* **2003**, *94*, 279–284.

(9) Absillis, G.; Cartuyvels, E.; Van Deun, R.; Parac-Vogt, T. N. Hydrolytic Cleavage of an RNA-Model Phosphodiester Catalyzed by a Highly Negatively Charged Polyoxomolybdate [Mo7O24]6- Cluster. *J. Am. Chem. Soc.* **2008**, *130*, 17400–17408.

(10) Absillis, G.; Van Deun, R.; Parac-Vogt, T. N. Polyoxomolybdate Promoted Hydrolysis of a DNA-Model Phosphoester Studied by NMR and EXAFS Spectroscopy. *Inorg. Chem.* **2011**, *50*, 11552–11560.

(11) Cartuyvels, E.; Absillis, G.; Parac-Vogt, T. N. Questioning the paradigm of metal complex promoted phosphodiester hydrolysis: [Mo7O24]6- polyoxometalate cluster as an unlikely catalyst for the hydrolysis of a DNA model substrate. *Chem. Commun.* **2007**, 85–87.

(12) Cartuyvels, E.; Van Hecke, K.; Van Meervelt, L.; Görller-Walrand, C.; Parac-Vogt, T. N. Structural characterization and reactivity of γ-octamolybdate functionalized by proline. *J. Inorg. Biochem.* **2008**, *102*, 1589–1598.

(13) Gomes, A. C.; Pillinger, M.; Nunes, P.; Gonçalves, I. S.; Abrantes, M. Promotion of phosphoester hydrolysis by MoO2Cl2L (L = bipyridine derivatives, H2O, no ligand), MoO2(CH3)2L (L = bipyridine derivatives) and related inorganic-organic hybrids in aqueous media. *J. Organomet. Chem.* **2014**, *760*, 42–47.

(14) Gomes, A. C.; Gamelas, C. A.; Fernandes, J. A.; Paz, F. A. A.; Nunes, P.; Pillinger, M.; Gonçalves, I. S.; Romão, C. C.; Abrantes, M. Use of Organomolybdenum Compounds for Promoted Hydrolysis of Phosphoester Bonds in Aqueous Media. *Eur. J. Inorg. Chem.* **2014**, *2014*, 3681–3689.

(15) Tomé, C. M.; Oliveira, M. C.; Pillinger, M.; Gonçalves, I. S.; Abrantes, M. Use of MoO2Cl2(DMF)2 as a precursor for molybdate promoted hydrolysis of phosphoester bonds. *Dalton Trans.* **2013**, *42*, 3901–3907.

(16) Green, M. L. H. In *Studies in Inorganic Chemistry*; Elsevier: Walthm, MA, USA, 1994; Vol. 19, pp 94–145.

(17) Lunk, H.-J.; Hartl, H. Discovery, properties and applications of molybdenum and its compounds. *ChemTexts* **2017**, *3*, 1–23.

(18) Gumerova, N. I.; Rompel, A. Interweaving Disciplines to Advance Chemistry: Applying Polyoxometalates in Biology. *Inorg. Chem.* **2021**, *60*, 6109–6114.

(19) Aureliano, M.; Mitchell, S. G.; Yin, P. Editorial: Emerging polyoxometalates with biological, biomedical, and health applications. *Front. Chem.* **2022**, *10*, DOI: 10.3389/fchem.2022.977317.

(20) Veríssimo, M. I. S.; Evtuguin, D. V.; Gomes, M. T. S. R. Polyoxometalate Functionalized Sensors: A Review. *Front. Chem.* **2022**, *10*, DOI: 10.3389/fchem.2022.840657.

(21) Garner, C. D. In *Studies in Inorganic Chemistry*; Elsevier: Walthm, MA, USA, 1994; Vol. 19, pp 403–418.

(22) Khurana, J. M.; Chauhan, S.; Agrawal, A. MOLYBDENUM IN ORGANIC SYNTHESIS. A REVIEW. *Org. Prep. Proced. Int.* **2004**, *36*, 201–276.

(23) Larson, M. L.; Moore, F. W. Coordination Chemistry of Molybdenum Oxochlorides. *Inorg. Chem.* **1966**, *5*, 801–805.

(24) Enemark, J. H.; Cooney, J. J. A.; Wang, J.-J.; Holm, R. H. Synthetic Analogues and Reaction Systems Relevant to the Molybdenum and Tungsten Oxotransferases. *Chem. Rev.* **2004**, *104*, 1175–1200.

(25) Wang, G.; Chen, G.; Luck, R. L.; Wang, Z.; Mu, Z.; Evans, D. G.; Duan, X. New molybdenum(VI) catalysts for the epoxidation of cyclohexene: synthesis, reactivity and crystal structures. *Inorg. Chim. Acta* **2004**, *357*, 3223–3229.

(26) Cai, S.-F.; Hu, F.-H. Solubilities of MoO2X2L2 (X = Cl, Br; L = OPPh3, OPMePh2) in Dichloromethane and H2O2 (30 % (By Weight)) + H2O Solution. *J. Chem. Eng. Data* **2009**, *54*, 2235–2238.

(27) Brito, J. A.; Royo, B.; Gómez, M. An overview of chiral molybdenum complexes applied in enantioselective catalysis. *Catal. Sci. Technol.* **2011**, *1*, 1109–1118.

(28) Szymańska, A.; Nitek, W.; Oszajca, M.; Łasocha, W.; Pamin, K.; Połtowicz, J. Molybdenum Complexes as Catalysts for the Oxidation of Cycloalkanes with Molecular Oxygen. *Catal. Lett.* **2016**, *146*, 998–1010.

(29) Pisk, J.; Prugovečki, B.; Matković-Čalogović, D.; Poli, R.; Agustin, D.; Vrdoljak, V. Charged dioxomolybdenum(VI) complexes with pyridoxal thiosemicarbazone ligands as molybdenum(V) precursors in oxygen atom transfer process and epoxidation (pre)catalysts. *Polyhedron* **2012**, *33*, 441–449.

(30) Thiel, W. R. Metal catalyzed oxidations. Part 5. Catalytic olefin epoxidation with seven-coordinate oxobisperoxo molybdenum complexes: a mechanistic study11For Part 4 of the series: see [1]. *J. Mol. Catal. A: Chem.* **1997**, *117*, 449–454.

(31) Jia, M.; Thiel, W. R. Oxodiperoxo molybdenum modified mesoporous MCM-41 materials for the catalytic epoxidation of cyclooctene. *Chem. Commun.* **2002**, 2392–2393.

(32) Djordjevic, C.; Puryear, B. C.; Vuletic, N.; Abelt, C. J.; Sheffield, S. J. Preparation, spectroscopic properties, and characterization of novel peroxo complexes of vanadium(V) and molybdenum(VI) with nicotinic acid and nicotinic acid N-oxide. *Inorg. Chem.* **1988**, *27*, 2926–2932.

(33) Brito, J. A.; Teruel, H.; Muller, G.; Massou, S.; Gómez, M. Molybdenum(VI)-catalysed olefin epoxidation: Structure and reactivity study. *Inorg. Chim. Acta* **2008**, *361*, 2740–2746.

(34) Yin, G. Active transition metal oxo and hydroxo moieties in nature's redox, enzymes and their synthetic models: Structure and reactivity relationships. *Coord. Chem. Rev.* **2010**, *254*, 1826–1842.

(35) Lyashenko, G.; Saischek, G.; Judmaier, M. E.; Volpe, M.; Baumgartner, J.; Belaj, F.; Jancik, V.; Herbst-Irmer, R.; Mösch-Zanetti, N. C. Oxo-molybdenum and oxo-tungsten complexes of Schiff bases relevant to molybdoenzymes. *Dalton Trans.* **2009**, 5655–5665.

(36) Abeysinghe, P. M.; Harding, M. M. Antitumour bis(cyclopentadienyl) metal complexes: titanocene and molybdocene dichloride and derivatives. *Dalton Trans.* **2007**, *0*, 3474–3482.

(37) Waern, J. B.; Harding, M. M. Coordination Chemistry of the Antitumor Metallocene Molybdocene Dichloride with Biological Ligands. *Inorg. Chem.* **2004**, *43*, 206–213.

(38) Hille, R.; Hall, J.; Basu, P. The Mononuclear Molybdenum Enzymes. *Chem. Rev.* **2014**, *114*, 3963–4038.

(39) Mitsui, S.; Ogata, A.; Yanagie, H.; Kasano, H.; Hisa, T.; Yamase, T.; Eriguchi, M. Antitumor activity of polyoxomolybdate, [NH3Pri]6[Mo7O24].3H2O, against, human gastric cancer model. *Biomed. Pharmacother.* **2006**, *60*, 353–358.

(40) Bijelic, A.; Aureliano, M.; Rompel, A. Polyoxometalates as Potential Next-Generation Metallodrugs in the Combat Against Cancer. *Angewandte Chemie (International Ed. in English)* **2019**, *58*, 2980.

(41) Li, G.; Ding, Y.; Wang, J.; Wang, X.; Suo, J. New progress of Keggin and Wells-Dawson type polyoxometalates catalyze acid and oxidative reactions. *J. Mol. Catal. A: Chem.* **2007**, *262*, 67–76.

(42) Qi, W.; Qin, Y.; Qi, Y.; Guo, L.; Li, J. In Vitro Antitumor Activity of a Keggin Vanadium-Substituted Polyoxomolybdate and its ctDNA Binding Properties. *J. Chem.* **2015**, *2015*, DOI: 10.1155/2015/753751.

(43) Wang, X.; Wei, S.; Zhao, C.; Li, X.; Jin, J.; Shi, X.; Su, Z.; Li, J.; Wang, J. Promising application of polyoxometalates in the treatment of cancer, infectious diseases and Alzheimer's disease. *JBIC, J. Biol. Inorg. Chem.* **2022**, *27*, 405–419.

(44) Duarte, F.; Barrozo, A.; Åqvist, J.; Williams, N. H.; Kamerlin, S. C. L. The Competing Mechanisms of Phosphate Monoester Dianion Hydrolysis. *J. Am. Chem. Soc.* **2016**, *138*, 10664–10673.

(45) Schrödinger, E. Quantisierung als Eigenwertproblem. *Ann. Phys.* **1926**, *385*, 437–490.

(46) Born, M.; Oppenheimer, R. Zur Quantentheorie der Molekeln. *Ann. Phys.* **1927**, *389*, 457–484.

(47) Hartree, D. R. The Wave Mechanics of an Atom with a Non-Coulomb Central Field. Part II. Some Results and Discussion. *Math. Proc. Cambridge Philos. Soc.* **1928**, *24*, 111–132.

(48) Slater, J. C. The Theory of Complex Spectra. *Phys. Rev.* **1929**, *34*, 1293–1322.

(49) Fock, V. Näherungsmethode zur Lösung des quantenmechanischen Mehrkörperproblems. *Z. Phys.* **1930**, *61*, 126–148.

(50) Rayner, H. D.; Hartree, W. Self-consistent field, with exchange, for beryllium. *Proc. R. Soc. London A - Math. Phys. Sci.* **1935**, *150*, 9–33.

(51) Slater, J. C. A Simplification of the Hartree-Fock Method. *Phys. Rev.* **1951**, *81*, 385–390.

(52) Heitler, W.; London, F. Wechselwirkung neutraler Atome und homöopolare Bindung nach der Quantenmechanik. *Z. Phys.* **1927**, *44*, 455–472.

(53) Pauling, L. The Application of the Quantum Mechanics to the Structure of the Hydrogen Molecule and Hydrogen Molecule-Ion and to Related Problems. *Chem. Rev.* **1928**, *5*, 173–213.

(54) Pauling, L. THE NATURE OF THE CHEMICAL BOND. APPLICATION OF RESULTS OBTAINED FROM THE QUANTUM MECHANICS AND FROM A THEORY OF PARAMAGNETIC SUSCEPTIBILITY TO THE STRUCTURE OF MOLECULES. *J. Am. Chem. Soc.* **1931**, *53*, 1367–1400.

(55) Lennard-Jones, J. E. The electronic structure of some diatomic molecules. *Trans. Faraday Soc.* **1929**, *25*, 668–686.

(56) Hückel, E. Theory of free radicals of organic chemistry. *Trans. Faraday Soc.* **1934**, *30*, 40–52.

(57) Coulson, C. A. Self-consistent field for molecular hydrogen. *Math. Proc. Cambridge Philos. Soc.* **1938**, *34*, 204–212.

(58) Hall G., G. The molecular orbital theory of chemical valency. VI. Properties of equivalent orbitals. *Proc. R. Soc. London A - Math. Phys. Sci.* **1950**, *202*, 336–344.

(59) Møller, C.; Plesset, M. S. Note on an Approximation Treatment for Many-Electron Systems. *Phys. Rev.* **1934**, *46*, 618–622.

(60) Pople, J. A.; Seeger, R.; Krishnan, R. Variational configuration interaction methods and comparison with perturbation theory. *Int. J. Quantum Chem.* **1977**, *12*, 149–163.

(61) Boys S., F. Electronic wave functions – I. A general method of calculation for the stationary states of any molecular system. *Proc. R. Soc. London A - Math. Phys. Sci.* **1950**, *200*, 542–554.

(62) Paldus, J. Group theoretical approach to the configuration interaction and perturbation theory calculations for atomic and molecular systems. *J. Chem. Phys.* **1974**, *61*, 5321–5330.

(63) Coester, F.; Kümmel, H. Short-range correlations in nuclear wave functions. *Nuclear Physics* **1960**, *17*, 477–485.

(64) Čížek, J. On the Correlation Problem in Atomic and Molecular Systems. Calculation of Wavefunction Components in Ursell-Type Expansion Using Quantum-Field Theoretical Methods. *J. Chem. Phys.* **1966**, *45*, 4256–4266.

(65) Thomas, L. H. The calculation of atomic fields. *Math. Proc. Cambridge Philos. Soc.* **1927**, *23*, 542–548.

(66) Fermi, E. Un Metodo Statistico per la Determinazione di Alcune Proprietà dell'Atomo. *Rendiconti Accademia Lincei* **1927**, *6*, 602–607.

(67) Hohenberg, P.; Kohn, W. Inhomogeneous Electron Gas. *Phys. Rev.* **1964**, *136*, B864–B871.

(68) Kohn, W.; Sham, L. J. Self-Consistent Equations Including Exchange and Correlation Effects. *Phys. Rev.* **1965**, *140*, A1133–A1138.

(69) Slater, J. C. Atomic Shielding Constants. *Phys. Rev.* **1930**, *36*, 57–64.

(70) Ditchfield, R.; Hehre, W. J.; Pople, J. A. Self-Consistent Molecular-Orbital Methods. IX. An Extended Gaussian-Type Basis for Molecular-Orbital Studies of Organic Molecules. *J. Chem. Phys.* **1971**, *54*, 724–728.

(71) Eyring, H.; Polanyi, M. On Simple Gas Reactions. *Z. Phys. Chem.* **1931**, *B*, 279–311.

(72) Sato, S. On a New Method of Drawing the Potential Energy Surface. *J. Chem. Phys.* **1955**, *23*, 592–593.

(73) Eyring, H. The Activated Complex in Chemical Reactions. *J. Chem. Phys.* **1935**, *3*, 107–115.

(74) Fukui, K. Formulation of the reaction coordinate. *J. Phys. Chem.* **1970**, *74*, 4161–4163.

(75) Ceperley, D. M.; Alder, B. J. Ground State of the Electron Gas by a Stochastic Method. *Phys. Rev. Lett.* **1980**, *45*, 566–569.

(76) Vosko, S. H.; Wilk, L.; Nusair, M. Accurate spin-dependent electron liquid correlation energies for local spin density calculations: a critical analysis. *Canadian Journal of Physics* **1980**, *58*, 1200–1211.

(77) Perdew, J. P.; Wang, Y. Accurate and simple analytic representation of the electron-gas correlation energy. *Phys. Rev. B* **1992**, *45*, 13244–13249.

(78) Langreth, D. C.; Perdew, J. P. Theory of nonuniform electronic systems. I. Analysis of the gradient approximation and a generalization that works. *Phys. Rev. B* **1980**, *21*, 5469–5493.

(79) Perdew, J. P.; Chevary, J. A.; Vosko, S. H.; Jackson, K. A.; Pederson, M. R.; Singh, D. J.; Fiolhais, C. Atoms, molecules, solids, and surfaces: Applications of the generalized gradient approximation for exchange and correlation. *Phys. Rev. B* **1992**, *46*, 6671–6687.

(80) Perdew, J. P.; Burke, K.; Ernzerhof, M. Generalized Gradient Approximation Made Simple. *Phys. Rev. Lett.* **1996**, *77*, 3865–3868.

(81) Becke, A. D. A new inhomogeneity parameter in density-functional theory. *J. Chem. Phys.* **1998**, *109*, 2092–2098.

(82) Tao, J.; Perdew, J. P.; Staroverov, V. N.; Scuseria, G. E. Climbing the Density Functional Ladder: Nonempirical Meta-Generalized Gradient Approximation Designed for Molecules and Solids. *Phys. Rev. Lett.* **2003**, *91*, 146401.

(83) Becke, A. D. A new mixing of Hartree–Fock and local density-functional theories. *J. Chem. Phys.* **1993**, *98*, 1372–1377.

(84) Becke, A. D. Density-functional thermochemistry. III. The role of exact exchange. *J. Chem. Phys.* **1993**, *98*, 5648–5652.

(85) Becke, A. D. Density-functional exchange-energy approximation with correct asymptotic behavior. *Phys. Rev. A* **1988**, *38*, 3098–3100.

(86) Wang, Y.; Perdew, J. P. Correlation hole of the spin-polarized electron gas, with exact small-wave-vector and high-density scaling. *Phys. Rev. B* **1991**, *44*, 13298–13307.

(87) Lee, C.; Yang, W.; Parr, R. G. Development of the Colle-Salvetti correlation-energy formula into a functional of the electron density. *Phys. Rev. B* **1988**, *37*, 785–789.

(88) Adamo, C.; Barone, V. Toward reliable density functional methods without adjustable parameters: The PBE0 model. *J. Chem. Phys.* **1999**, *110*, 6158–6170.

(89) Zhao, Y.; Schultz, N. E.; Truhlar, D. G. Exchange-correlation functional with broad accuracy for metallic and nonmetallic compounds, kinetics, and noncovalent interactions. *J. Chem. Phys.* **2005**, *123*, 161103.

(90) Zhao, Y.; Schultz, N. E.; Truhlar, D. G. Design of Density Functionals by Combining the Method of Constraint Satisfaction with Parametrization for Thermochemistry, Thermochemical Kinetics, and Noncovalent Interactions. *J. Chem. Theory Comput.* **2006**, *2*, 364–382.

(91) Zhao, Y.; Truhlar, D. G. The M06 suite of density functionals for main group thermochemistry, thermochemical kinetics, noncovalent interac-

tions, excited states, and transition elements: two new functionals and systematic testing of four M06-class functionals and 12 other functionals. *Theor. Chem. Acc.* **2008**, *120*, 215–241.

(92) Zhao, Y.; Truhlar, D. G. Exploring the Limit of Accuracy of the Global Hybrid Meta Density Functional for Main-Group Thermochemistry, Kinetics, and Noncovalent Interactions. *J. Chem. Theory Comput.* **2008**, *4*, 1849–1868.

(93) Peverati, R.; Truhlar, D. G. Improving the Accuracy of Hybrid Meta-GGA Density Functionals by Range Separation. *J. Phys. Chem. Lett.* **2011**, *2*, 2810–2817.

(94) Peverati, R.; Truhlar, D. G. Screened-exchange density functionals with broad accuracy for chemistry and solid-state physics. *Phys. Chem. Chem. Phys.* **2012**, *14*, 16187–16191.

(95) Yu, H. S.; He, X.; Li, S. L.; Truhlar, D. G. MN15: A Kohn–Sham global-hybrid exchange–correlation density functional with broad accuracy for multi-reference and single-reference systems and noncovalent interactions. *Chem. Sci.* **2016**, *7*, 5032–5051.

(96) Grimme, S. Semiempirical GGA-type density functional constructed with a long-range dispersion correction. *J. Comput. Chem.* **2006**, *27*, 1787–1799.

(97) Grimme, S.; Antony, J.; Ehrlich, S.; Krieg, H. A consistent and accurate ab initio parametrization of density functional dispersion correction (DFT-D) for the 94 elements H-Pu. *J. Chem. Phys.* **2010**, *132*, 154104.

(98) Grimme, S.; Ehrlich, S.; Goerigk, L. Effect of the damping function in dispersion corrected density functional theory. *J. Comput. Chem.* **2011**, *32*, 1456–1465.

(99) Grimme, S. Semiempirical hybrid density functional with perturbative second-order correlation. *J. Chem. Phys.* **2006**, *124*, 034108.

(100) Schwabe, T.; Grimme, S. Towards chemical accuracy for the thermodynamics of large molecules: new hybrid density functionals including non-local correlation effects. *Phys. Chem. Chem. Phys.* **2006**, *8*, 4398–4401.

(101) Schwabe, T.; Grimme, S. Double-hybrid density functionals with long-range dispersion corrections: higher accuracy and extended applicability. *Phys. Chem. Chem. Phys.* **2007**, *9*, 3397–3406.

(102) Grimme, S.; Neese, F. Double-hybrid density functional theory for excited electronic states of molecules. *J. Chem. Phys.* **2007**, *127*, 154116.

(103) Tarnopolsky, A.; Karton, A.; Sertchook, R.; Vuzman, D.; Martin, J. M. L. Double-Hybrid Functionals for Thermochemical Kinetics. *J. Phys. Chem. A* **2008**, *112*, 3–8.

(104) Bohm, D.; Pines, D. A Collective Description of Electron Interactions: III. Coulomb Interactions in a Degenerate Electron Gas. *Phys. Rev.* **1953**, *92*, 609–625.

(105) Langreth, D. C.; Perdew, J. P. The exchange-correlation energy of a metallic surface. *Solid State Commun.* **1975**, *17*, 1425–1429.

(106) Furche, F. Molecular tests of the random phase approximation to the exchange-correlation energy functional. *Phys. Rev. B* **2001**, *64*, 195120.

(107) Harl, J.; Kresse, G. Accurate Bulk Properties from Approximate Many-Body Techniques. *Phys. Rev. Lett.* **2009**, *103*, 056401.

(108) Paier, J.; Ren, X.; Rinke, P.; Scuseria, G. E.; Grüneis, A.; Kresse, G.; Scheffler, M. Assessment of correlation energies based on the random-phase approximation. *New J. Phys.* **2012**, *14*, 043002.

(109) Zhang, I. Y.; Xu, X. On the top rung of Jacob's ladder of density functional theory: Toward resolving the dilemma of SIE and NCE. *WIREs Comput. Mol. Sci.* **2021**, *11*, e1490.

(110) Mulliken, R. S. Electronic Population Analysis on LCAO–MO Molecular Wave Functions. I. *J. Chem. Phys.* **1955**, *23*, 1833–1840.

(111) Löwdin, P.-O. On the Non-Orthogonality Problem Connected with the Use of Atomic Wave Functions in the Theory of Molecules and Crystals. *J. Chem. Phys.* **1950**, *18*, 365–375.

(112) Bader, R.; Bader, R., *Atoms in Molecules: A Quantum Theory*; International series of monographs on chemistry; Clarendon Press: 1990.

(113) Bader, R. F. W. A quantum theory of molecular structure and its applications. *Chem. Rev.* **1991**, *91*, 893–928.

(114) Stalke, D. Meaningful Structural Descriptors from Charge Density. *Chem. Eur. J.* **2011**, *17*, 9264–9278.

(115) Hirshfeld, F. L. Bonded-atom fragments for describing molecular charge densities. *Theor. Chim. Acta* **1977**, *44*, 129–138.

(116) Bultinck, P.; Van Alsenoy, C.; Ayers, P. W.; Carbó-Dorca, R. Critical analysis and extension of the Hirshfeld atoms in molecules. *J. Chem. Phys.* **2007**, *126*, 144111.

(117) Becke, A. D. A multicenter numerical integration scheme for polyatomic molecules. *J. Chem. Phys.* **1988**, *88*, 2547–2553.

(118) Mayer, I.; Salvador, P. Overlap populations, bond orders and valences for 'fuzzy' atoms. *Chem. Phys. Lett.* **2004**, *383*, 368–375.

(119) Matito, E.; Solà, M.; Salvador, P.; Duran, M. Electron sharing indexes at the correlated level. Application to aromaticity calculations. *Faraday Discuss.* **2006**, *135*, 325–345.

(120) Salvador, P.; Ramos-Cordoba, E. Communication: An approximation to Bader's topological atom. *J. Chem. Phys.* **2013**, *139*, 071103.

(121) Miertuš, S.; Scrocco, E.; Tomasi, J. Electrostatic interaction of a solute with a continuum. A direct utilizaion of AB initio molecular potentials for the prevision of solvent effects. *Chem. Phys.* **1981**, *55*, 117–129.

(122) Miertuš, S.; Tomasi, J. Approximate evaluations of the electrostatic free energy and internal energy changes in solution processes. *Chem. Phys.* **1982**, *65*, 239–245.

(123) Cancès, E.; Mennucci, B.; Tomasi, J. A new integral equation formalism for the polarizable continuum model: Theoretical background and applications to isotropic and anisotropic dielectrics. *J. Chem. Phys.* **1997**, *107*, 3032–3041.

(124) Cancès, E.; Mennucci, B. New applications of integral equations methods for solvation continuum models: ionic solutions and liquid crystals. *J. Math. Chem.* **1998**, *23*, 309–326.

(125) Klamt, A. Conductor-like Screening Model for Real Solvents: A New Approach to the Quantitative Calculation of Solvation Phenomena. *J. Phys. Chem.* **1995**, *99*, 2224–2235.

(126) Klamt, A.; Schüürmann, G. COSMO: a new approach to dielectric screening in solvents with explicit expressions for the screening energy and its gradient. *J. Chem. Soc., Perkin Trans. 2* **1993**, 799–805.

(127) Klamt, A.; Jonas, V. Treatment of the outlying charge in continuum solvation models. *J. Chem. Phys.* **1996**, *105*, 9972–9981.

(128) Kamerlin, S. C. L.; Sharma, P. K.; Prasad, R. B.; Warshel, A. Why nature really chose phosphate. *Q. Rev. Biophys.* **2013**, *46*, 1–132.

(129) Cleland, W. W.; Hengge, A. C. Enzymatic Mechanisms of Phosphate and Sulfate Transfer. *Chem. Rev.* **2006**, *106*, 3252–3278.

(130) Silverman, S. K. Pursuing DNA Catalysts for Protein Modification. *Acc. Chem. Res.* **2015**, *48*, 1369–1379.

(131) Gomez, S.; Marchena, C. L.; Renzini, M. S.; Pizzio, L.; Pierella, L. In situ generated TiO2 over zeolitic supports as reusable photocatalysts for the degradation of dichlorvos. *Appl. Catal. B* **2015**, *162*, 167–173.

(132) Sirotkina, M.; Lyagin, I.; Efremenko, E. Hydrolysis of organophosphorus pesticides in soil: New opportunities with ecocompatible immobilized His6-OPH. *Int. Biodeterior. Biodegrad.* **2012**, *68*, 18–23.

(133) Kumar, S. V.; Fareedullah, M.; Sudhakar, Y.; Venkateswarlu, B. S.; Kumar, E. A. Current review on organophosphorus poisoning. *Archives of Applied Science Research* **2010**, *2*, 199–215.

(134) Eddleston, M.; Buckley, N. A.; Eyer, P.; Dawson, A. H. Management of acute organophosphorus pesticide poisoning. *Lancet* **2008**, *371*, 597–607.

(135) Morales-Rojas, H.; Moss, R. A. Phosphorolytic Reactivity of o-Iodosylcarboxylates and Related Nucleophiles. *Chem. Rev.* **2002**, *102*, 2497–2522.

(136) García-Martínez, J.; Serrano-Torregrosa, E., *The Chemical Element: Chemistry's Contribution to Our Global Future*; Wiley: Weinheim, Germany, 2011.

(137) Herbst, A.; Janiak, C. MOF catalysts in biomass upgrading towards value-added fine chemicals. *CrystEngComm* **2017**, *19*, 4092–4117.

(138) Moon, S.-Y.; Liu, Y.; Hupp, J. T.; Farha, O. K. Instantaneous Hydrolysis of Nerve-Agent Simulants with a Six-Connected Zirconium-Based Metal-Organic Framework. *Angew. Chem. Int. Ed.* **2015**, *54*, 6795–6799.

(139) Kim, K.; Tsay, O. G.; Atwood, D. A.; Churchill, D. G. Destruction and Detection of Chemical Warfare Agents. *Chem. Rev.* **2011**, *111*, 5345–5403.

(140) Erxleben, A.; Claffey, J.; Tacke, M. Binding and hydrolysis studies of antitumoural titanocene dichloride and Titanocene Y with phosphate diesters. *J. Inorg. Biochem.* **2010**, *104*, 390–396.

(141) Steens, N.; Ramadan, A. M.; Absillis, G.; Parac-Vogt, T. N. Hydrolytic cleavage of DNA-model substrates promoted by polyoxovanadates. *Dalton Trans.* **2009**, *39*, 585–592.

(142) Steens, N.; Ramadan, A. M.; Parac-Vogt, T. N. When structural and electronic analogy leads to reactivity: the unprecedented phosphodiesterase activity of vanadates. *Chem. Commun.* **2009**, 965–967.

(143) Aguilar-Pérez, F.; Gómez-Tagle, P.; Collado-Fregoso, E.; Yatsimirsky, A. K. Phosphate Ester Hydrolysis by Hydroxo Complexes of Trivalent Lanthanides Stabilized by 4-Imidazolecarboxylate. *Inorg. Chem.* **2006**, *45*, 9502–9517.

(144) Baldwin, D. S.; Beattie, J. K.; Coleman, L. M.; Jones, D. R. Hydrolysis of an Organophosphate Ester by Manganese Dioxide. *Environ. Sci. Technol.* **2001**, *35*, 713–716.

(145) Jia-qing, X.; Yong, C.; Ci, L.; Jiu-jin, Z.; Wei, H.; Xian-cheng, Z. Hydrolysis of Bis(4-Nitrophenyl) Phosphate Catalyzed by Metallomicelle Made Up of the Crowned Schiff Base Complex as Synthetic Hydrolase. *J. Dispersion Sci. Technol.* **2005**, *26*, 693–699.

(146) Jiang, W.; Xu, B.; Lin, Q.; Li, J.; Liu, F.; Zeng, X.; Chen, H. Metal-promoted hydrolysis of bis(p-nitrophenyl)phosphate by trivalent manganese complexes with Schiff base ligands in Gemini micellar solution. *Colloids Surf., A* **2008**, *315*, 103–109.

(147) Jiang, W.-d.; Xu, B.; Li, J.-z.; Xie, J.-q.; Fu, H.-y.; Chen, H.; Zeng, X.-c. Studies on BNPP Cleavage by Schiff Base Complexes Containing Benzoaza-15-Crown-5 in DHAB Micellar Solution. *J. Dispersion Sci. Technol.* **2006**, *27*, 869–877.

(148) Katz, M. J.; Mondloch, J. E.; Totten, R. K.; Park, J. K.; Nguyen, S. T.; Farha, O. K.; Hupp, J. T. Simple and Compelling Biomimetic Metal-Organic Framework Catalyst for the Degradation of Nerve Agent Simulants. *Angew. Chem. Int. Ed.* **2014**, *53*, 497–501.

(149) Ma, Y.-Y.; Wu, C.-X.; Feng, X.-J.; Tan, H.-Q.; Yan, L.-K.; Liu, Y.; Kang, Z.-H.; Wang, E.-B.; Li, Y.-G. Highly efficient hydrogen evolution from seawater by a low-cost and stable CoMoP@C electrocatalyst superior to Pt/C. *Energy Environ. Sci.* **2017**, *10*, 788–798.

(150) Wang, S.-S.; Yang, G.-Y. Recent Advances in Polyoxometalate-Catalyzed Reactions. *Chem. Rev.* **2015**, *115*, 4893–4962.

(151) Calderazzo, F. et al., *Metal-catalysis in Industrial Organic Processes*; The Royal Society of Chemistry: 2006.

(152) Brown, K. A.; Harris, D. F.; Wilker, M. B.; Rasmussen, A.; Khadka, N.; Hamby, H.; Keable, S.; Dukovic, G.; Peters, J. W.; Seefeldt, L. C.; King, P. W. Light-driven dinitrogen reduction catalyzed by a CdS:nitrogenase MoFe protein biohybrid. *Science* **2016**, *352*, 448–450.

(153) Mendel, R. R.; Hänsch, R. Molybdoenzymes and molybdenum cofactor in plants. *Journal of Experimental Botany* **2002**, *53*, 1689–1698.

(154) Hille, R. The Mononuclear Molybdenum Enzymes. *Chem. Rev.* **1996**, *96*, 2757–2816.

(155) Ma, J.; Bei, Q.; Wang, X.; Lan, P.; Liu, G.; Lin, X.; Liu, Q.; Lin, Z.; Liu, B.; Zhang, Y.; Jin, H.; Hu, T.; Zhu, J.; Xie, Z. Impacts of Mo application on biological nitrogen fixation and diazotrophic communities in a flooded rice-soil system. *Sci. Total Environ.* **2019**, *649*, 686–694.

(156) Gupta, U. C., *Molybdenum in Agriculture*, [Online; accessed 11. Apr. 2022]; Cambridge University Press: 1997.

(157) Ahmed, T. J.; Zakharov, L. N.; Tyler, D. R. Organometallic Catalysis in Aqueous Solution. The Hydrolytic Activity of a Water-Soluble ansa-Molybdocene Catalyst. *Organometallics* **2007**, *26*, 5179–5187.

(158) Kuo, L. Y.; Perera, N. M. Paraoxon and Parathion Hydrolysis by Aqueous Molybdenocene Dichloride (Cp2MoCl2): First Reported Pesticide Hydrolysis by an Organometallic Complex. *Inorg. Chem.* **2000**, *39*, 2103–2106.

(159) Kuo, L. Y.; Barnes, L. A. Aqueous Phosphoester Bond Cleavage of Dimethyl Phosphate by Cp2MoCl2: First Reported Case of Hydrolytic Cleavage on an Unactivated Phosphate Diester by an Organometallic Complex. *Inorg. Chem.* **1999**, *38*, 814–817.

(160) Kuo, L. Y.; Kuhn, S.; Ly, D. First Reported Aqueous Phosphoester Bond Cleavage Promoted by an Organometallic Complex. *Inorg. Chem.* **1995**, *34*, 5341–5345.

(161) Weil-Malherbe, H.; Green, R. H. The catalytic effect of molybdate on the hydrolysis of organic phosphate bonds. *Biochem. J.* **1951**, *49*, 286–292.

(162) Lutwak, L.; Sacks, J. THE CATALYTIC EFFECT OF MOLYBDATE ON THE HYDROLYSIS OF ORGANIC PHOSPHATES. *J. Biol. Chem.* **1953**, *200*, 565–569.

(163) Weil-Malherbe, H. The catalytic effect of molybdate on the hydrolysis of organic phosphates. *Biochem. J.* **1953**, *55*, 741–745.

(164) Poppe, J.; Brünle, S.; Hail, R.; Wiesemann, K.; Schneider, K.; Ermler, U. The Molybdenum Storage Protein: A soluble ATP hydrolysis-dependent molybdate pump. *FEBS J.* **2018**, *285*, 4602–4616.

(165) Ishikawa, E.; Yamase, T. Catalytic Hydrolysis of Adenosine Triphosphate (ATP) by Antitumoral xn–kza-Keggin Core Compound, [H2MoV12O28(OH)12(MoVIO3)4]6-, at pH 5 and 7.5. *Eur. J. Inorg. Chem.* **2013**, *2013*, 1917–1925.

(166) Ishikawa, E.; Yamase, T. 31P NMR and isothermal titration calorimetry studies on polyoxomolybdates-catalyzed hydrolysis of ATP. *J. Inorg. Biochem.* **2006**, *100*, 344–350.

(167) Petrović, D.; Szeler, K.; Kamerlin, S. C. L. Challenges and advances in the computational modeling of biological phosphate hydrolysis. *Chem. Commun.* **2018**, *54*, 3077–3089.

(168) Lassila, J. K.; Zalatan, J. G.; Herschlag, D. Biological Phosphoryl-Transfer Reactions: Understanding Mechanism and Catalysis. *Annu. Rev. Biochem.* **2011**, *80*, 669–702.

(169) Gregersen, B. A.; Lopez, X.; York, D. M. Hybrid QM/MM Study of Thio Effects in Transphosphorylation Reactions: The Role of Solvation. *J. Am. Chem. Soc.* **2004**, *126*, 7504–7513.

(170) Gregersen, B. A.; Lopez, X.; York, D. M. Hybrid QM/MM Study of Thio Effects in Transphosphorylation Reactions. *J. Am. Chem. Soc.* **2003**, *125*, 7178–7179.

(171) Lopez, X.; Dejaegere, A.; Karplus, M. Solvent Effects on the Reaction Coordinate of the Hydrolysis of Phosphates and Sulfates: Application of Hammond and Anti-Hammond Postulates to Understand Hydrolysis in Solution. *J. Am. Chem. Soc.* **2001**, *123*, 11755–11763.

(172) Formoso, E.; Matxain, J. M.; Lopez, X.; York, D. M. Molecular Dynamics Simulation of Bovine Pancreatic Ribonuclease A-CpA and Transition State-like Complexes. *J. Phys. Chem. B* **2010**, *114*, 7371–7382.

(173) Lopez, X.; Dejaegere, A.; Leclerc, F.; York, D. M.; Karplus, M. Nucleophilic Attack on Phosphate Diesters: A Density Functional Study of In-Line Reactivity in Dianionic, Monoanionic, and Neutral Systems. *J. Phys. Chem. B* **2006**, *110*, 11525–11539.

(174) Liu, Y.; Gregersen, B. A.; Lopez, X.; York, D. M. Density Functional Study of the In-Line Mechanism of Methanolysis of Cyclic Phosphate and Thiophosphate Esters in Solution: Insight into Thio Effects in RNA Transesterification. *J. Phys. Chem. B* **2005**, *109*, 19987–20003.

(175) Liu, Y.; Lopez, X.; York, D. M. Kinetic isotope effects on thio-substituted biological phosphoryl transfer reactions from density-functional theory. *Chem. Commun.* **2005**, 3909–3911.

(176) Range, K.; McGrath, M. J.; Lopez, X.; York, D. M. The Structure and Stability of Biological Metaphosphate, Phosphate, and Phosphorane Compounds in the Gas Phase and in Solution. *J. Am. Chem. Soc.* **2004**, *126*, 1654–1665.

(177) López, C. S.; Faza, O. N.; Gregersen, B. A.; Lopez, X.; de Lera, A. R.; York, D. M. Pseudorotation of Natural and Chemically Modified Biological Phosphoranes: Implications for RNA Catalysis. *ChemPhysChem* **2004**, *5*, 1045–1049.

(178) Lopez, X.; Schaefer, M.; Dejaegere, A.; Karplus, M. Theoretical Evaluation of pKa in Phosphoranes: Implications for Phosphate Ester Hydrolysis. *J. Am. Chem. Soc.* **2002**, *124*, 5010–5018.

(179) Lopez, X.; York, D. M.; Dejaegere, A.; Karplus, M. Theoretical studies on the hydrolysis of phosphate diesters in the gas phase, solution, and RNase A. *Int. J. Quantum Chem.* **2002**, *86*, 10–26.

(180) Duarte, F.; Åqvist, J.; Williams, N. H.; Kamerlin, S. C. L. Resolving Apparent Conflicts between Theoretical and Experimental Models of Phosphate Monoester Hydrolysis. *J. Am. Chem. Soc.* **2015**, *137*, 1081–1093.

(181) Bianciotto, M.; Barthelat, J.-C.; Vigroux, A. Reactivity of Phosphate Monoester Monoanions in Aqueous Solution. 1. Quantum Mechanical Calculations Support the Existence of "Anionic Zwitterion"

MeO+(H)PO32- as a Key Intermediate in the Dissociative Hydrolysis of the Methyl Phosphate Anion1. *J. Am. Chem. Soc.* **2002**, *124*, 7573–7587.

(182) Bianciotto, M.; Barthelat, J.-C.; Vigroux, A. Reactivity of Phosphate Monoester Monoanions in Aqueous Solution. 2. A Theoretical Study of the Elusive Zwitterion Intermediates RO+(H)PO32-. *J. Phys. Chem. A* **2002**, *106*, 6521–6526.

(183) Grzyska, P. K.; Czyryca, P. G.; Purcell, J.; Hengge, A. C. Transition State Differences in Hydrolysis Reactions of Alkyl versus Aryl Phosphate Monoester Monoanions. *J. Am. Chem. Soc.* **2003**, *125*, 13106–13111.

(184) Zalatan, J. G.; Herschlag, D. Alkaline Phosphatase Mono- and Diesterase Reactions: Comparative Transition State Analysis. *J. Am. Chem. Soc.* **2006**, *128*, 1293–1303.

(185) Te Velde, G.; Bickelhaupt, F. M.; Baerends, E. J.; Guerra, C. F.; van Gisbergen, S. J. A.; Snijders, J. G.; Ziegler, T. Chemistry with ADF. *J. Comput. Chem.* **2001**, *22*, 931–967.

(186) Fonseca Guerra, C.; Snijders, J. G.; Te Velde, G.; Baerends, E. J. Towards an order-N DFT method. *Theor. Chem. Acc.* **1998**, *99*, 391–403.

(187) Amsterdam Density Functional (ADF): DFT for molecules, Vrije Universiteit, Amsterdam, the Netherlands, 2010.

(188) Frisch, M. J. et al. Gaussian˜16 Revision C.01, Gaussian Inc. Wallingford CT, 2016.

(189) Perdew, J. P. Density-functional approximation for the correlation energy of the inhomogeneous electron gas. *Phys. Rev. B* **1986**, *33*, 8822–8824(R).

(190) Van Lenthe, E. v.; Baerends, E. J.; Snijders, J. G. Relativistic regular two-component Hamiltonians. *J. Chem. Phys.* **1993**, *99*, 4597–4610.

(191) Van Lenthe, E.; Baerends, E. J.; Snijders, J. G. Relativistic total energy using regular approximations. *J. Chem. Phys.* **1994**, *101*, 9783–9792.

(192) Hay, P. J.; Wadt, W. R. Ab initio effective core potentials for molecular calculations. Potentials for the transition metal atoms Sc to Hg. *J. Chem. Phys.* **1985**, *82*, 270–283.

(193) Wadt, W. R.; Hay, P. J. Ab initio effective core potentials for molecular calculations. Potentials for main group elements Na to Bi. *J. Chem. Phys.* **1985**, *82*, 284–298.

(194) Hay, P. J.; Wadt, W. R. Ab initio effective core potentials for molecular calculations. Potentials for K to Au including the outermost core orbitals. *J. Chem. Phys.* **1985**, *82*, 299–310.

(195) Check, C. E.; Faust, T. O.; Bailey, J. M.; Wright, B. J.; Gilbert, T. M.; Sunderlin, L. S. Addition of Polarization and Diffuse Functions to the LANL2DZ Basis Set for P-Block Elements. *J. Phys. Chem. A* **2001**, *105*, 8111–8116.

(196) Ehlers, A. W.; Böhme, M.; Dapprich, S.; Gobbi, A.; Höllwarth, A.; Jonas, V.; Köhler, K. F.; Stegmann, R.; Veldkamp, A.; Frenking, G. A set of f-polarization functions for pseudo-potential basis sets of the transition metals xn–ScCu-c13v, xn–YAg-w25q and xn–LaAu-c13v. *Chem. Phys. Lett.* **1993**, *208*, 111–114.

(197) Hratchian, H. P.; Schlegel, H. B. Accurate reaction paths using a Hessian based predictor-corrector integrator. *J. Chem. Phys.* **2004**, *120*, 9918–9924.

(198) Hratchian, H. P.; Schlegel, H. B. Using Hessian Updating To Increase the Efficiency of a Hessian Based Predictor-Corrector Reaction Path Following Method. *J. Chem. Theory Comput.* **2005**, *1*, 61–69.

(199) Hehre, W. J.; Ditchfield, R.; Pople, J. A. Self-Consistent Molecular Orbital Methods. XII. Further Extensions of Gaussian-Type Basis Sets for Use in Molecular Orbital Studies of Organic Molecules. *J. Chem. Phys.* **1972**, *56*, 2257–2261.

(200) Besora, Maria and Vidossich, Pietro and Lledós, Agustí and Ujaque, Gregori and Maseras, Feliu Calculation of Reaction Free Energies in Solution: A Comparison of Current Approaches. *The Journal of Physical Chemistry A* **2018**, *122*, 1392–1399.

(201) Johnson, E. R.; Keinan, S.; Mori-Sánchez, P.; Contreras-García, J.; Cohen, A. J.; Yang, W. Revealing Noncovalent Interactions. *Journal of the American Chemical Society* **2010**, *132*, 6498–6506.

(202) Teith, T. A. AIMAll, version 15.09.27, Gristmill TK Software, Overland Park, KS, 2015.

(203) McCleverty, J. A. In *Encyclopedia of Inorganic and Bioinorganic Chemistry*; John Wiley & Sons, Ltd: Chichester, England, UK, 2011.

(204) Vilà-Nadal, L.; Wilson, E. F.; Miras, H. N.; Rodríguez-Fortea, A.; Cronin, L.; Poblet, J. M. Combined Theoretical and Mass Spectrometry Study of the Formation-Fragmentation of Small Polyoxomolybdates. *Inorg. Chem.* **2011**, *50*, 7811–7819.

(205) Vilà-Nadal, L.; Mitchell, S. G.; Rodríguez-Fortea, A.; Miras, H. N.; Cronin, L.; Poblet, J. M. Connecting theory with experiment to understand the initial nucleation steps of heteropolyoxometalate clusters. *Phys. Chem. Chem. Phys.* **2011**, *13*, 20136–20145.

(206) Gouzerh, P.; Che, M. From Scheele and Berzelius to Müller: Polyoxometalates (POMs) revisited and the "missing link" between the bottom up and top down approaches. *Actualite Chimique* **2006**, 9–22.

(207) Greenwood, N. N.; Earnshaw, A., *Chemistry of the Elements*; Butterworth-Heinemann: Oxford, England, UK, 1997.

(208) Mir'o, P.; Pierrefixe, S.; Gicquel, M.; Gil, A.; Bo, C. On the Origin of the Cation Templated Self-Assembly of Uranyl-Peroxide Nanoclusters. *J. Am. Chem. Soc.* **2010**, *132*, 17787–17794.

(209) Gil, A.; Karhánek, D.; Miró, P.; Antonio, M. R.; Nyman, M.; Bo, C. A Journey inside the U28 Nanocapsule. *Chem. Eur. J.* **2012**, *18*, 8340–8346.

(210) Tiferet, E.; Gil, A.; Bo, C.; Shvareva, T. Y.; Nyman, M.; Navrotsky, A. The Energy Landscape of Uranyl-Peroxide Species. *Chem. Eur. J.* **2014**, *20*, 3646–3651.

(211) Miró, P.; Vlaisavljevich, B.; Gil, A.; Burns, P. C.; Nyman, M.; Bo, C. Self-Assembly of Uranyl-Peroxide Nanocapsules in Basic Peroxidic Environments. *Chem. Eur. J.* **2016**, *22*, 8571–8578.

(212) Yang, P.; Ma, T.; Lang, Z.; Misirlic-Dencic, S.; Isakovic, A. M.; Bényei, A.; Čolović, M. B.; Markovic, I.; Krstić, D. Z.; Poblet, J. M.; Lin, Z.; Kortz, U. Tetravalent Metal Ion Guests in Polyoxopalladate Chemistry: Synthesis and Anticancer Activity of [MO8Pd12(PO4)8]12- (M = SnIV, PbIV). *Inorg. Chem.* **2019**, *58*, 11294–11299.

(213) Ayass, W. W. et al. Synthesis, Structure, and Antibacterial Activity of a Thallium(III)-Containing Polyoxometalate, [Tl2{B-β-SiW8O30(OH)}2]12-. *Inorg. Chem.* **2016**, *55*, 10118–10121.

(214) Hiskia, A.; Troupis, A.; Antonaraki, S.; Gkika, E.; Papaconstantinou, P. K. Polyoxometallate photocatalysis for decontaminating the aquatic environment from organic and inorganic pollutants. *Int. J. Environ. Anal. Chem.* **2006**, *86*, 233–242.

(215) Busche, C.; Vilà-Nadal, L.; Yan, J.; Miras, H. N.; Long, D.-L.; Georgiev, V. P.; Asenov, A.; Pedersen, R. H.; Gadegaard, N.; Mirza, M. M.; Paul, D. J.; Poblet, J. M.; Cronin, L. Design and fabrication of memory devices based on nanoscale polyoxometalate clusters. *Nature* **2014**, *515*, 545–549.

(216) Lehmann, J.; Gaita-Arinō, A.; Coronado, E.; Loss, D. Spin qubits with electrically gated polyoxometalate molecules. *Nat. Nanotechnol.* **2007**, *2*, 312–317.

(217) Buvailo, H. I.; Makhankova, V. G.; Kokozay, V. N.; Omelchenko, I. V.; Shishkina, S. V.; Jezierska, J.; Pavliuk, M. V.; Shylin, S. I. Copper-containing hybrid compounds based on extremely rare [V2Mo6O26]6- POM as water oxidation catalysts. *Inorg. Chem. Front.* **2019**, *6*, 1813–1823.

(218) Rhule, J. T.; Hill, C. L.; Judd, D. A.; Schinazi, R. F. Polyoxometalates in Medicine. *Chem. Rev.* **1998**, *98*, 327–358.

(219) Hasenknopf, B. Polyoxometalates: introduction to a class of inorganic compounds and their biomedical applications. *Frontiers in Bioscience-Landmark* **2005**, *10*, 275–287.

(220) Yamase, T. Polyoxometalates for molecular devices: Antitumor activity and luminescence. *Mol. Eng.* **1993**, *3*, 241–262.

(221) Li, J.; Qi, Y.; Li, J.; Wang, H.; Wu, X.; Duan, L.; Wang, E. Heteropolymolybdate-amino acid complexes: synthesis, characterization and biological activity. *J. Coord. Chem.* **2004**, *57*, 1309–1319.

(222) Gerth, H. U. V.; Rompel, A.; Krebs, B.; Boos, J.; Lanvers-Kaminsky, C. Cytotoxic effects of novel polyoxotungstates and a platinum compound on human cancer cell lines. *Anti-Cancer Drugs* **2005**, *16*, 101–106.

(223) Wang, X.; Li, F.; Liu, S.; Pope, M. T. New liposome-encapsulated-polyoxometalates: synthesis and antitumoral activity. *J. Inorg. Biochem.* **2005**, *99*, 452–457.

(224) Ogata, A.; Mitsui, S.; Yanagie, H.; Kasano, H.; Hisa, T.; Yamase, T.; Eriguchi, M. A novel anti-tumor agent, polyoxomolybdate induces apoptotic cell death in AsPC-1 human pancreatic cancer cells. *Biomed. Pharmacother.* **2005**, *59*, 240–244.

(225) Bijelic, A.; Aureliano, M.; Rompel, A. The antibacterial activity of polyoxometalates: structures, antibiotic effects and future perspectives. *Chem. Commun.* **2018**, *54*, 1153–1169.

(226) Ma, T. et al. Tetra-(p-tolyl)antimony(III)-Containing Heteropolytungstates, [{(p-tolyl)SbIII}4(A-α-XW9O34)2]n- (X = P, As, or Ge): Synthesis, Structure, and Study of Antibacterial and Antitumor Activity. *Inorg. Chem.* **2020**, *59*, 2978–2987.

(227) Radzicka, A.; Wolfenden, R. A Proficient Enzyme. *Science* **1995**, *267*, 90–93.

(228) Alberts, B., *Molecular Biology of the Cell*; Garland Science: Abingdon, England, UK, 2017.

(229) Lokeren, L. V.; Cartuyvels, E.; Absillis, G.; Willem, R.; Parac-Vogt, T. N. Phosphoesterase activity of polyoxomolybdates: diffusion ordered NMR spectroscopy as a tool for obtaining insights into the reactivity of polyoxometalate clusters. *Chem. Commun.* **2008**, 2774–2776.

(230) Vanhaecht, S.; Absillis, G.; Parac-Vogt, T. N. Hydrolysis of DNA model substrates catalyzed by metal-substituted Wells-Dawson polyoxometalates. *Dalton Trans.* **2012**, *41*, 10028–10034.

(231) Li, W.; Rudack, T.; Gerwert, K.; Gräter, F.; Schlitter, J. Exploring the Multidimensional Free Energy Surface of Phosphoester Hydrolysis with Constrained QM/MM Dynamics. *J. Chem. Theory Comput.* **2012**, *8*, 3596–3604.

(232) Nunes, P.; Gomes, A. C.; Pillinger, M.; Gonçalves, I. S.; Abrantes, M. Promotion of phosphoester hydrolysis by the ZrIV-based metal-organic framework UiO-67. *Microporous Mesoporous Mater.* **2015**, *208*, 21–29.

(233) Lain, L.; Lönnberg, H.; Lönnberg, T. Intramolecular Participation of Amino Groups in the Cleavage and Isomerization of Ribonucleoside 3′-Phosphodiesters: The Role in Stabilization of the Phosphorane Intermediate. *Chem. Eur. J.* **2013**, *19*, 12424–12434.

(234) Das, P.; Chandar, N. B.; Chourey, S.; Agarwalla, H.; Ganguly, B.; Das, A. Role of Metal Ion in Specific Recognition of Pyrophosphate Ion under Physiological Conditions and Hydrolysis of the Phosphoester Linkage by Alkaline Phosphatase. *Inorg. Chem.* **2013**, *52*, 11034–11041.

(235) Luong, T. K. N.; Absillis, G.; Shestakova, P.; Parac-Vogt, T. N. Solution Speciation of the Dinuclear ZrIV-Substituted Keggin Polyoxometalate [{α-PW11O39Zr(μ-OH)(H2O)}2]8- and Its Reactivity towards DNA-Model Phosphodiester Hydrolysis. *Eur. J. Inorg. Chem.* **2014**, *2014*, 5276–5284.

(236) Luong, T. K. N.; Absillis, G.; Shestakova, P.; Parac-Vogt, T. N. Hydrolysis of the RNA model substrate catalyzed by a binuclear ZrIV-substituted Keggin polyoxometalate. *Dalton Trans.* **2015**, *44*, 15690–15696.

(237) Luong, T. K. N.; Shestakova, P.; Mihaylov, T. T.; Absillis, G.; Pierloot, K.; Parac-Vogt, T. N. Multinuclear Diffusion NMR Spectroscopy and DFT Modeling: A Powerful Combination for Unraveling the Mechanism of Phosphoester Bond Hydrolysis Catalyzed by Metal-Substituted Polyoxometalates. *Chem. Eur. J.* **2015**, *21*, 4428–4439.

(238) Gouré, E.; Carboni, M.; Troussier, A.; Lebrun, C.; Pécaut, J.; Jacquot, J.-F.; Dubourdeaux, P.; Clémancey, M.; Blondin, G.; Latour, J.-M. Phosphoester Hydrolysis: The Incoming Substrate Turns the Bridging Hydroxido Nucleophile into a Terminal One. *Chem. Eur. J.* **2015**, *21*, 8064–8068.

(239) Luong, T. K. N.; Shestakova, P.; Parac-Vogt, T. N. Kinetic studies of phosphoester hydrolysis promoted by a dimeric tetrazirconium(iv) Wells-Dawson polyoxometalate. *Dalton Trans.* **2016**, *45*, 12174–12180.

(240) Bosch, S.; Comba, P.; Gahan, L. R.; Schenk, G. Asymmetric mono- and dinuclear GaIII and ZnII complexes as models for purple acid phosphatases. *J. Inorg. Biochem.* **2016**, *162*, 343–355.

(241) Kandasamy, B.; Vanhaecht, S.; Nkala, F. M.; Beelen, T.; Bassil, B. S.; Parac-Vogt, T. N.; Kortz, U. Gallium(III)-Containing, Sandwich-Type Heteropolytungstates: Synthesis, Solution Characterization, and Hy-

drolytic Studies toward Phosphoester and Phosphoanhydride Bond Cleavage. *Inorg. Chem.* **2016**, *55*, 9204–9211.

(242) Luong, T. K. N.; Mihaylov, T. T.; Absillis, G.; Shestakova, P.; Pierloot, K.; Parac-Vogt, T. N. Phosphate Ester Bond Hydrolysis Promoted by Lanthanide-Substituted Keggin-type Polyoxometalates Studied by a Combined Experimental and Density Functional Theory Approach. *Inorg. Chem.* **2016**, *55*, 9898–9911.

(243) Luong, T. K. N.; Govaerts, I.; Robben, J.; Shestakova, P.; Parac-Vogt, T. N. Polyoxometalates as artificial nucleases: hydrolytic cleavage of DNA promoted by a highly negatively charged ZrIV-substituted Keggin polyanion. *Chem. Commun.* **2017**, *53*, 617–620.

(244) De, A.; Pradhan, S. S.; Biswas, B. Coordinated aqua molecules mediated phosphoester cleavage activity of a dimeric gadolinium(III)-acetate. *J. Indian Chem. Soc.* **2017**, *94*, 1063–1071.

(245) Huang, X.-L. Hydrolysis of Phosphate Esters Catalyzed by Inorganic Iron Oxide Nanoparticles Acting as Biocatalysts. *Astrobiology* **2018**, *18*, 294–310.

(246) Hu, Q.; Jayasinghe-Arachchige, V. M.; Zuchniarz, J.; Prabhakar, R. Effects of the Metal Ion on the Mechanism of Phosphodiester Hydrolysis Catalyzed by Metal-Cyclen Complexes. *Front. Chem.* **2019**, *7*, DOI: 10.3389/fchem.2019.00195.

(247) Kou, H.; Wang, Y.; Ding, P.; Li, J.; Shi, B. A new macrocyclic heterobinuclear Cu(II)-Zn(II) complex: synthesis, crystal structure, phos-

phate hydrolysis, and DNA binding studies. *J. Coord. Chem.* **2019**, *72*, 1683–1696.

(248) Pereira, C.; Farias, G.; Maranha, F. G.; Castilho, N.; Schenk, G.; de Souza, B.; Terenzi, H.; Neves, A.; Peralta, R. A. Guanidine- and purine-functionalized ligands of FeIIIZnII complexes: effects on the hydrolysis of DNA. *JBIC, J. Biol. Inorg. Chem.* **2019**, *24*, 675–691.

(249) Hu, Q.; Jayasinghe-Arachchige, V. M.; Sharma, G.; Serafim, L. F.; Paul, T. J.; Prabhakar, R. Mechanisms of peptide and phosphoester hydrolysis catalyzed by two promiscuous metalloenzymes (insulin degrading enzyme and glycerophosphodiesterase) and their synthetic analogues. *WIREs Comput. Mol. Sci.* **2020**, *10*, e1466.

(250) Morrow, J. R.; Trogler, W. C. Hydrolysis of phosphate diesters with copper(II) catalysts. *Inorg. Chem.* **1988**, *27*, 3387–3394.

(251) Koike, T.; Kimura, E. Roles of zinc(II) ion in phosphatases. A model study with zinc(II)-macrocyclic polyamine complexes. *J. Am. Chem. Soc.* **1991**, *113*, 8935–8941.

(252) Amin, S.; Voss, D. A.; Horrocks, W. D.; Morrow, J. R. Restoration of Catalytic Activity by Replacement of a Coordinated Amide Group: Synthesis and Laser-Induced Luminescence Studies of the Phosphate Diester Transesterification Catalyst [Eu(NBAC)]3+. *Inorg. Chem.* **1996**, *35*, 7466–7467.

(253) Amin, S.; Voss, D. A.; Horrocks, W. D.; Lake, C. H.; Churchill, M. R.; Morrow, J. R. Laser-Induced Luminescence Studies and Crystal Structure of the Europium(III) Complex of 1,4,7,10-

Tetrakis(carbamoylmethyl)-1,4,7,10-tetraazacyclododecane. The Link between Phosphate Diester Binding and Catalysis by Lanthanide(III) Macrocyclic Complexes. *Inorg. Chem.* **1995**, *34*, 3294–3300.

(254) Chin, K. O. A.; Morrow, J. R. RNA Cleavage and Phosphate Diester Transesterification by Encapsulated Lanthanide Ions: Traversing the Lanthanide Series with Lanthanum(III), Europium(III), and Lutetium(III) Complexes of1,4,7,10-Tetrakis(2-hydroxyalkyl)-1,4,7,10-tetraazacyclododecane. *Inorg. Chem.* **1994**, *33*, 5036–5041.

(255) Fischer, J.; Ricard, L.; Toledano, P. A novel phosphomolybdate structure: crystal structure of [NH4]5[(MoO3)5(PO4)(HPO4)],3H2O. *J. Chem. Soc., Dalton Trans.* **1974**, 941–946.

(256) Momma, K.; Izumi, F. VESTA 3 for three-dimensional visualization of crystal, volumetric and morphology data. *J. Appl. Crystallogr.* **2011**, *44*, 1272–1276.

(257) Zhurko, G. A.; A., Z. D. ChemCraft, Tool for Treatment of the Chemical Data. http://www.chemcraftprog.com.

(258) Miras, H. N.; Stone, D.; Long, D.-L.; McInnes, E. J. L.; Kögerler, P.; Cronin, L. Exploring the Structure and Properties of Transition Metal Templated {VM17(VO4)2} Dawson-Like Capsules. *Inorg. Chem.* **2011**, *50*, 8384–8391.

(259) Mattes, R. Heteropoly and Isopoly Oxometalates. Von M. T. Pope. Springer-Verlag, Berlin 1983. XIII, 180 S., geb. DM 124.00. *Angew. Chem.* **1984**, *96*, 730.

(260) Lv, H.; Geletii, Y. V.; Zhao, C.; Vickers, J. W.; Zhu, G.; Luo, Z.; Song, J.; Lian, T.; Musaev, D. G.; Hill, C. L. Polyoxometalate water oxidation catalysts and the production of green fuel. *Chem. Soc. Rev.* **2012**, *41*, 7572–7589.

(261) Yamase, T.; Pope, M. T., *Polyoxometalate Chemistry for Nano-Composite Design*; Springer, Boston, MA: Boston, MA, USA, 2002.

(262) Bijelic, A.; Rompel, A. The use of polyoxometalates in protein crystallography – An attempt to widen a well-known bottleneck. *Coord. Chem. Rev.* **2015**, *299*, 22–38.

(263) Sadakane, M.; Steckhan, E. Electrochemical Properties of Polyoxometalates as Electrocatalysts. *Chem. Rev.* **1998**, *98*, 219–238.

(264) Wang, J.; Liu, Y.; Xu, K.; Qi, Y.; Zhong, J.; Zhang, K.; Li, J.; Wang, E.; Wu, Z.; Kang, Z. Broad-Spectrum Antiviral Property of Polyoxometalate Localized on a Cell Surface. *ACS Appl. Mater. Interfaces* **2014**, *6*, 9785–9789.

(265) Bijelic, A.; Aureliano, M.; Rompel, A. The antibacterial activity of polyoxometalates: structures, antibiotic effects and future perspectives. *Chemical Communications (Cambridge, England)* **2018**, *54*, 1153.

(266) Chen, K.; Yu, Q.; Liu, Y.; Yin, P. Bacterial hyperpolarization modulated by polyoxometalates for solutions of antibiotic resistance. *J. Inorg. Biochem.* **2021**, *220*, 111463.

(267) Yamase, T. Anti-tumor, -viral, and -bacterial activities of polyoxometalates for realizing an inorganic drug. *J. Mater. Chem.* **2005**, *15*, 4773–4782.

(268) Katsoulis, D. E.; Lambrianidou, A. N.; Pope, M. T. Heteropoly molybdate complexes of flavin mononucleotide and some other phosphate esters. *Inorg. Chim. Acta* **1980**, *46*, L55–L57.

(269) Geraldes, C. F. G. C.; Castro, M. M. C. A. 1H and 31P NMR study of the interaction of molybdate with the nucleotides adenosine 5'-diphosphate and adenosine 5'-triphosphate. *J. Inorg. Biochem.* **1986**, *28*, 319–327.

(270) Piperaki, P.; Katsaros, N.; Katakis, D. The interaction of oxomolybdenum(VI) with nucleic acid bases and nucleosides. *Inorg. Chim. Acta* **1982**, *67*, 37–44.

(271) Chang, C. A.; Wu, T.-T.; Lee, H.-Y. Hydrolysis and DFT structural studies of dinuclear Zn(II) and Cu(II) macrocyclic complexes of m-12N3O-dimer and the effect of pH on their promoted HPNP hydrolysis rates. *J. Coord. Chem.* **2016**, *69*, 1388–1405.

(272) Daver, H.; Das, B.; Nordlander, E.; Himo, F. Theoretical Study of Phosphodiester Hydrolysis and Transesterification Catalyzed by an Unsymmetric Biomimetic Dizinc Complex. *Inorg. Chem.* **2016**, *55*, 1872–1882.

(273) Colvin, M. E.; Evleth, E.; Akacem, Y. Quantum chemical studies of pyrophosphate hydrolysis. *J. Am. Chem. Soc.* **1995**, *117*, 4357–4362.

(274) Lopez, X.; York, D. M. Parameterization of semiempirical methods to treat nucleophilic attacks to biological phosphates: AM1/d parameters for phosphorus. *Theor. Chem. Acc.* **2003**, *109*, 149–159.

(275) Giese, T. J.; Gregersen, B. A.; Liu, Y.; Nam, K.; Mayaan, E.; Moser, A.; Range, K.; Faza, O. N.; Lopez, C. S.; Lera, A. R. d.; Schaftenaar, G.; Lopez, X.; Lee, T.-S.; Karypis, G.; York, D. M. QCRNA 1.0: A database of quantum calculations for RNA catalysis. *J. Mol. Graphics Model.* **2006**, *25*, 423–433.

(276) Martins, F. F.; Sánchez-González, Á.; Lanuza, J.; Miras, H. N.; Lopez, X.; Bandeira, N. A.; Gil, A. Probing the Catalytically Active Species in POM-Catalysed DNA-Model Hydrolysis. *Chem. Eur. J.* **2021**, *27*, 8977–8984.

(277) Lanuza, J.; Sánchez-González, Á.; Bandeira, N. A. G.; Lopez, X.; Gil, A. Mechanistic Insights into Promoted Hydrolysis of Phosphoester Bonds by MoO2Cl2(DMF)2. *Inorg. Chem.* **2021**, *60*, 11177–11191.

(278) Sánchez-González, Á.; Bandeira, N. A. G.; Ortiz de Luzuriaga, I.; Martins, F. F.; Elleuchi, S.; Jarraya, K.; Lanuza, J.; Lopez, X.; Calhorda, M. J.; Gil, A. New Insights on the Interaction of Phenanthroline Based Ligands and Metal Complexes and Polyoxometalates with Duplex DNA and G-Quadruplexes. *Molecules* **2021**, *26*, 4737.

(279) Gil, A.; Carbó, J. J. Computational Modelling of the Interactions Between Polyoxometalates and Biological Systems. *Front. Chem.* **2022**, *10*, 1–7.

(280) Wilson, E. F.; Miras, H. N.; Rosnes, M. H.; Cronin, L. Real-Time Observation of the Self-Assembly of Hybrid Polyoxometalates Using Mass Spectrometry. *Angew. Chem. Int. Ed.* **2011**, *50*, 3720–3724.

(281) Zang, H.; Surman, A.; Long, D.; Cronin, L.; Miras, H. N. Exploiting the equilibrium dynamics in the self-assembly of inorganic macrocycles based upon polyoxothiometalate building blocks. *Chem. Commun.* **2016**, *52*, 9109–9112.

(282) Zang, H.-Y.; Chen, J.-J.; Long, D.-L.; Cronin, L.; Miras, H. N. Assembly of Thiometalate-Based {Mo16} and {Mo36} Composite Clusters Combining [Mo2O2S2]2+ Cations and Selenite Anions. *Adv. Mater.* **2013**, *25*, 6245–6249.

(283) Pettersson, L.; Andersson, I.; Oehman, L. O. Multicomponent polyanions. 39. Speciation in the aqueous hydrogen ion-molybdate(MoO42-)-hydrogenphosphate(HPO42-) system as deduced from a combined Emf-phosphorus-31 NMR study. *Inorg. Chem.* **1986**, *25*, 4726–4733.

Appendix A

ESI-MS OF THE HEPTAMOLYBDATE AND NITROPHENYL PHOSPHATE REACTION MIXTURE

A.1 Experimental Details

All MS data were collected by our colleagues using a Q-trap, time-of-flight MS (Maxis Impact MS) instrument supplied by Bruker Daltonics Ltd. The detector was a time-of-flight, micro-channel plate detector and all data was processed using the Bruker Daltonics Data Analysis 4.1 software, whilst simulated isotope patterns were investigated using Bruker Isotope Pattern software and Molecular Weight Calculator 6.45. The calibration solution used was Agilent ES tuning mix solution, Recorder No. G2421 A, enabling calibration between approximately 100 m/z and 3000 m/z. This solution was diluted 60:1 with MeCN. Samples were dissolved in H_2O/MeOH (20:80) and introduced into the MS via direct injection at 180 μL/h. The ion polarity for all MS scans recorded was negative, at 180 °C, with the voltage of the capillary tip set at 4000 V, end plate offset at 500 V, funnel 1 RF at 300 Vpp and funnel 2 RF at 400 Vpp.

A.2 ESI-MS Results

The ESI-MS studies were performed in water/methanol (20:80). The speciation and fragment rearrangements were investigated as follows:

Equimolar amounts of sodium heptamolybdate, $Na_6[Mo_7O_{24}]$ and NPP (100 mM, pH = 5.4) were dissolved in aqueous solution and stirred at 50 °C for approximately 30 h. Aliquots were removed at noted time intervals throughout the reaction, diluted with methanol, and analysed using ESI-MS (the parameters for which were consistent throughout all runs). It is important to note at this point that no precipitation has been observed during the course of the catalytic reaction. The first spectrum was recorded upon mixing the starting materials (t = 0) and after the reaction mixture had been stirred at 50 °C for 1, 3 and 30 h, respectively. In all cases, the observation of distribution envelopes of higher m/z values are due to the existence of the heptanuclear moiety, resulting from the combination of protons, counterions and solvent molecules. Additionally, transition metal clusters are generally susceptible to redox processes. The observed change of the oxidation state of the metal centres is due to the ionisation and consecutive ion-transfer process of the charged species and have been observed previously on numerous occasions.[280–282]

In this case, the region of higher m/z values is populated by a series of distribution envelopes assigned to 1 charged species and can be assigned to the $\{Mo_7\}$ intact cluster (Figure 4.5, Table A.1) with the corresponding distribution envelopes centred at ca. 1103.27, 1225.25 and 1249.24 m/z. The intensity of the envelopes corresponding to the intact Mo7 cluster can be detected clearly the first 3 h of the reaction while their relevant intensity gradually decreases to

Table A.1: Representation of the experimentally identified and simulated m/z values of distribution envelopes corresponding to the species in the reaction mixture.

Exp.	Theor.	Charge	Chemical formula
218.00	217.98	−1	$[NO_2C_6H_4PO_4H]^-$
304.77	304.77	−1	$[Mo_2O_7H]^-$
448.66	448.70	−1	$[Mo_3O_{10}H]^-$
470.64	470.65	−1	$[Mo_3O_{10}Na]^-$
510.72	510.70	−1	$[Mo^{IV}Mo^{V}{}_2O_9Na(H_2O)_3H_2]^-$
592.65	592.75	−1	$[Mo_3O_{15}(H_2O)_3H_{11}]^-$
614.54	614.56	−1	$[Mo_4O_{13}Na]^-$
654.73	654.64	−1	$[Mo_2O_7(NO_2C_6H_4PO_4)Na_5(H_2O)H]^-$
671.64	671.71	−1	$[Mo_2O_7(NO_2C_6H_4PO_4)Na_5(H_2O)H_2]^-$
882.40	882.31	−1	$[Mo_5P_2O_{21}H_5]^-$
904.29	904.39	−1	$[Mo_5P_2O_{21}NaH_4]^-$
999.35	999.36	−1	$[Mo_5P_2O_{23}Na_3(H_2O)H_3]^-$
1017.47	1017.37	−1	$[Mo_5P_2O_{23}Na_3(H_2O)_2H_3]^-$
1046.22	1046.35	−1	$[Mo_5P_2O_{21}Na_5(H_2O)_3]^-$
1082.30	1082.37	−1	$[Mo_5P_2O_{21}Na_5(H_2O)_5]^-$
1103.27	1103.34	−1	$[Mo_7O_{24}Na(H_2O)H_7]^-$
1225.25	1225.20	−1	$[Mo_7O_{24}Na_5(H_2O)_3H]^-$
1249.24	1249.20	−1	$[Mo_7O_{24}Na_6(H_2O)_3H_2]^-$

the point where cannot be detected any more (t = 30 h). As expected, the peak centred at 217.90 m/z can be assigned to the singly charged organic molecule of $[NO_2C_6H_4PO_4H]^-$. The relevant intensity of the free organic ligand fluctuates during the course of the study due to the formation of intermediate catalytic organic-inorganic adducts followed by their subsequent decomposition after 30 h.

Interestingly, the lower region of m/z values (ca. 300−1100) revealed additional information regarding the building block units that can be generated *insitu* during the course of the catalytic reaction. The distribution envelopes centred at 304.77, 448.66, 470.64 and 510.72 m/z values have been identified as

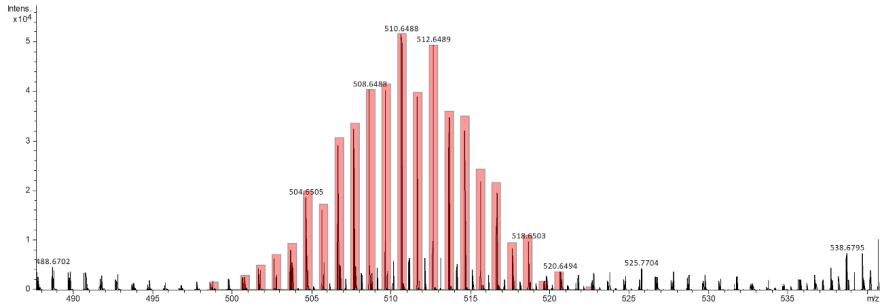

Figure A.1: Expanded isotopic distribution envelope of the main singly charged moiety observed in the catalysed reaction centred at m/z ca. 510.72, associated to the $[Mo^{IV}Mo^{V}{}_2O_9Na(H_2O)_3H_2]^-$ species. Black line: experimental data, Red bars: simulation of isotope pattern.

dimeric $\{Mo_2\}$ and trimeric $\{Mo_3\}$ (Figure A.1) units associated with different number of counterions and solvent molecules while the envelope at 614.54 m/z (Figure A.2) could be assigned to the tetrameric molybdenum moiety, $[Mo_4O_{13}Na]^-$. Interestingly, two envelopes centred at 654.73 and 671.64 m/z values (Figure A.3) have been identified as the Mo2 dimeric NPP adducts revealing the ability to the lower nuclearity species to form hybrid complexes with the organic moiety.

The higher m/z region (800–1000 m/z) revealed the formation of pentamolybdodiphosphate-based, $[Mo_5O_{15}(PO_4)_2]^{6-}$, derivatives which typically form in mildly acidic solutions containing molybdate and phosphate ions.[283] However, it has been reported that the $[Mo_5O_{15}(PO_4)_2]^{6-}$ anion does not induce the cleavage of the phosphoester bond in NPP, even after prolonged reaction times[229] which is an indication that the species forms *in situ* due to the presence of free ${PO_4}^{3-}$ anions originating from the cleavage of phosphate groups.

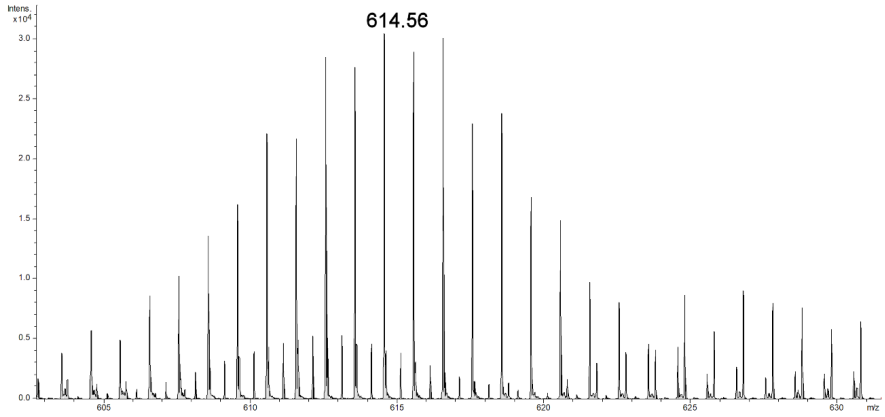

Figure A.2: Expanded isotopic distribution envelope of the singly charged moiety observed in the catalysed reaction centred at m/z ca. 614.54, associated to the $[Mo_4O_{13}Na]^-$ species.

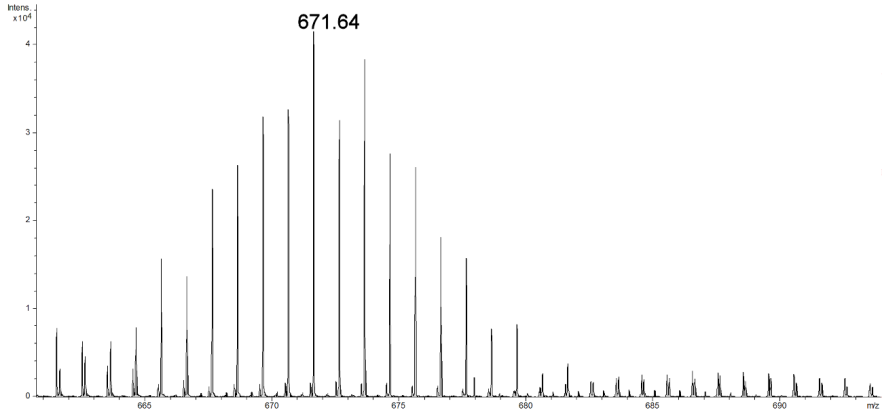

Figure A.3: Expanded isotopic distribution envelope of the singly charged moiety observed in the catalysed reaction centred at m/z ca. 671.64, associated to the $[Mo_2{}^{V}O_7(NO_2C_6H_4PO_4)Na_5(H_2O)H_2]^-$ species.

Table A.2: Representation of the experimentally identified and simulated m/z values of distribution envelopes corresponding to the species of the uncatalysed reaction mixture.

Exp.	Theor.	Charge	Chemical formula
439.67	439.66	−2	$[Mo_6O_{19}H]^{2-}$
511.61	511.62	−2	$[Mo_7O_{22}]^{2-}$
592.57	592.56	−1	$[Mo_3O_{15}(H_2O)_3H_{11}]^{-}$
655.58	654.51	−2	$[Mo_7O_{24}Na_8(H_2O)_4]^{2-}$
799.94	799.93	−2	$[(Mo_5O_{16})_2Na_4(H_2O)_2]^{2-}$
880.34	880.35	−1	$[Mo_6O_{19}H]_2^{-}$
943.87	943.80	−2	$[(Mo_6O_{19})_2Na_3(H_2O)_3H_5]^{2-}$

Overall, the higher nuclearity species identified during the first hours of the reaction (t = 0−3), degrade over time, including the $\{Mo_7\}$, $\{Mo_5\}$ and $\{Mo_4\}$ observed during the first hours, and only dimeric and trimeric species can be identified after 30 h. In an effort to investigate the fragmentation processes that might take place during the course of the ESI-MS studies, we have recorded the ESI-MS of the $\{Mo_7\}$ starting material under the same conditions but in the absence of NPP moiety. In the case of the uncatalysed system the main peak can be assigned as the intact $\{Mo_7\}$ species along with a $\{Mo_6\}$ species due to limited fragmentation (Figure 4.6, Figure A.4, Figure A.5, Figure A.6 and Table A.2). This is in marked contrast to the extended speciation observed in the case of the catalysed reaction where we were able to observe a variety of species ranging from $\{Mo_2\}$ all the way up to $\{Mo_7\}$ upon addition of the NPP moiety (Table A.1). These observations collectively increase our understanding of the rearrangement processes taking place in the reaction solution.

In summary, several peaks were observed for $\{Mo_5\}$ related species (m/z = 882.40 to 999.35) that incorporate either one or two phosphate groups. These

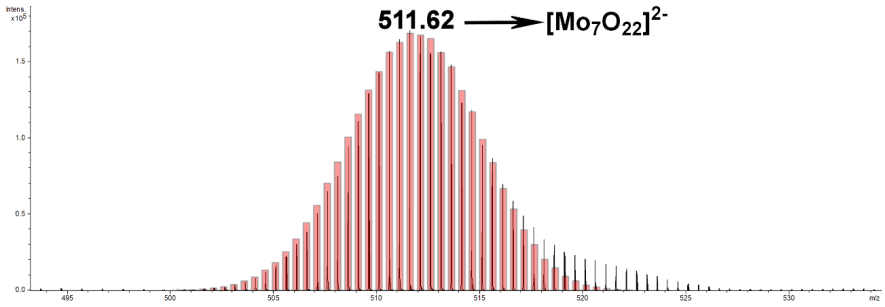

Figure A.4: Expanded isotopic distribution envelope of the main doubly charged species centred at m/z ca. 511.62, associated with the Mo_7 cluster. The observed species originates form the starting material $[Mo_7O_{24}]^{6-}$ after the loss of two oxygen atoms occurred during the ionisation process. Black line: experimental data, Red bars: simulation of isotope pattern.

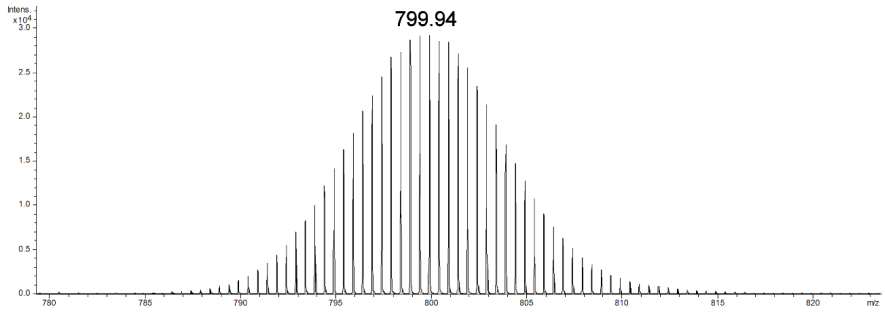

Figure A.5: Expanded isotopic distribution envelope of the singly charged species centred at m/z ca. 799.94, associated to the $[(Mo^{V}Mo_4{}^{VI}O_{16})_2Na_4(H_2O)_2]^{2-}$ fragment.

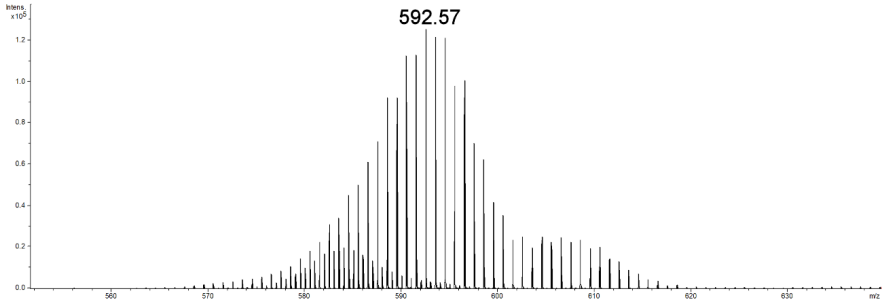

Figure A.6: Expanded isotopic distribution envelope of the singly charged species centred at m/z ca. 592.57, associated to the $[Mo_3O_{15}(H_2O)_3H_{11}]^{-}$ fragment.

species have been identified and reported previously in the literature.[255] Interestingly, none of the identified species corresponds to an adduct of $\{Mo_7\}$ ($1103.27 < m/z < 1249.24$) or $\{Mo_5\}$ type fragment associated with the NPP anion.[229]